

---


Electronic Theses and Dissertations, 2004-2019

---

2008

## Digital Signal Processing Techniques For Coherent Optical Communication

Gilad Goldfarb  
*University of Central Florida*

 Part of the [Electromagnetics and Photonics Commons](#), and the [Optics Commons](#)  
Find similar works at: <https://stars.library.ucf.edu/etd>  
University of Central Florida Libraries <http://library.ucf.edu>

This Doctoral Dissertation (Open Access) is brought to you for free and open access by STARS. It has been accepted for inclusion in Electronic Theses and Dissertations, 2004-2019 by an authorized administrator of STARS. For more information, please contact [STARS@ucf.edu](mailto:STARS@ucf.edu).

---

### STARS Citation

Goldfarb, Gilad, "Digital Signal Processing Techniques For Coherent Optical Communication" (2008).  
*Electronic Theses and Dissertations, 2004-2019*. 3730.  
<https://stars.library.ucf.edu/etd/3730>

# DIGITAL SIGNAL PROCESSING TECHNIQUES FOR COHERENT OPTICAL COMMUNICATION

by  
GILAD GOLDFARB

B.S. Ben-Gurion University, Israel, 2002  
M.S. University of Central Florida, 2005

A dissertation submitted in partial fulfillment of the requirements  
for the degree of Doctor of Philosophy in Optics  
in the Department of Optics  
in the College of Optics and Photonics  
at the University of Central Florida  
Orlando, Florida

Fall Term  
2008  
Major Professor: Guifang Li

© 2008 GILAD GOLDFARB

*To my uncle, David.*

## ABSTRACT

Coherent detection with subsequent digital signal processing (DSP) is developed, analyzed theoretically and numerically and experimentally demonstrated in various fiber-optic transmission scenarios. The use of DSP in conjunction with coherent detection unleashes the benefits of coherent detection which rely on the preservation of full information of the incoming field. These benefits include high receiver sensitivity, the ability to achieve high spectral-efficiency and the use of advanced modulation formats.

With the immense advancements in DSP speeds, many of the problems hindering the use of coherent detection in optical transmission systems have been eliminated. Most notably, DSP alleviates the need for hardware phase-locking and polarization tracking, which can now be achieved in the digital domain. The complexity previously associated with coherent detection is hence significantly diminished and coherent detection is once again considered a feasible detection alternative.

In this thesis, several aspects of coherent detection (with or without subsequent DSP) are addressed. Coherent detection is presented as a means to extend the dispersion limit of a duobinary signal using an analog decision-directed phase-lock loop. Analytical bit-error ratio estimation for quadrature phase-shift keying signals is derived. To validate the promise for high spectral efficiency, the orthogonal-wavelength-division multiplexing scheme is suggested. In this scheme the WDM channels are spaced at the symbol rate, thus achieving the spectral efficiency limit. Theory, simulation and experimental results demonstrate the feasibility of this approach. Infinite impulse response filtering is shown to be an efficient alternative to finite

impulse response filtering for chromatic dispersion compensation. Theory, design considerations, simulation and experimental results relating to this topic are presented.

Interaction between fiber dispersion and nonlinearity remains the last major challenge deterministic effects pose for long-haul optical data transmission. Experimental results which demonstrate the possibility to digitally mitigate both dispersion and nonlinearity are presented. Impairment compensation is achieved using backward propagation by implementing the split-step method. Efficient realizations of the dispersion compensation operator used in this implementation are considered. Infinite-impulse response and wavelet-based filtering are both investigated as a means to reduce the required computational load associated with signal backward-propagation.

Possible future research directions conclude this dissertation.

## TABLE OF CONTENTS

LIST OF FIGURES .....	ix
LIST OF COMMON ACRONYMS AND ABBREVIATIONS .....	xii
CHAPTER 1. INTRODUCTION .....	1
1.1. Historical Perspective.....	1
1.2. Modern Perspective.....	3
1.3. Coherently Detected Optical Systems with Subsequent DSP.....	7
1.4. Generic Scheme .....	10
1.5. Noise Sources in Coherent Detection .....	13
1.6. Dissertation Outline .....	17
CHAPTER 2. DUOBINARY TRANSMISSION USING COHERENT DETECTION .....	22
2.1. Introduction .....	22
2.2. Evolution of the Duobinary Constellation Diagram.....	24
2.3. Chromatic Dispersion Tolerance of Direct and Coherent Detection .....	28
2.4. Conclusions .....	32
CHAPTER 3. FEED-FORWARD CARRIER PHASE ESTIMATION .....	33
3.1. Introduction .....	33
3.2. BER Estimation for QPSK Homodyne Detection .....	33
3.2.1. Distribution of the Phase Error $\Delta\phi$ .....	37

3.2.2. Comparison with Monte-Carlo Simulation .....	43
3.3. Cycle Slips in Feed-Forward Carrier Recovery Schemes .....	44
3.4. Conclusions .....	54
CHAPTER 4. ORTHOGONAL WAVELENGTH-DIVISION MULTIPLEXING .....	56
4.1. Introduction .....	56
4.2. Theory .....	56
4.3. OFDM Simulation .....	58
4.4. Experimental Results .....	60
4.5. Effect of Receiver Bandwidth and Front End Filtering.....	63
4.6. Conclusion .....	64
CHAPTER 5. CHROMATIC DISPERSION COMPENSATION USING DIGITAL INFINITE-IMPULSE RESPONSE FILTERING .....	65
5.1. Introduction .....	65
5.2. Theory .....	66
5.2.1. Real Coefficients IIR Filters .....	66
5.2.2. Complex Coefficients IIR Filters .....	69
5.3. Simulation .....	70
5.4. Experimental setup .....	72
5.5. Extension to Larger Dispersion Values.....	74



5.6. Conclusion .....	77
CHAPTER 6. DISTRIBUTED COMPENSATION .....	78
6.1. Introduction .....	78
6.2. Backward Propagation Scheme .....	80
6.2.1. Step-size Dependence.....	81
6.3. Experimental Setup.....	82
6.4. Experimental Results .....	85
6.5. SSM with Infinite-Impulse Response Filtering .....	88
6.5.1. Complex-IIR filtering Computational Load Reduction .....	91
6.6. Wavelet-Based Split-Step Method for Backward-Propagation .....	92
6.6.1. Theory of Wavelet-Based Dispersion Compensation .....	93
6.6.2. Numerical Simulation and Results .....	95
6.7. Conclusions .....	99
CHAPTER 7. SUMMARY AND FUTURE RESEARCH DIRECTIONS .....	101
REFERENCES .....	107

## LIST OF FIGURES

Figure 1-1: Spectral efficiency vs. SNR and number of channels .....	4
Figure 1-2: Generic transmission scheme with coherent detection and subsequent DSP .....	10
Figure 1-3: 90° optical hybrid .....	11
Figure 1-4: Effect of phase noise on constellation and correction.....	16
Figure 1-5: Arrangement of dissertation .....	18
Figure 2-1: (left) Generation of PCD signal, (center) NRZ and PCD spectra, (right) NRZ, IM/Duobinary and PCD constellations.....	23
Figure 2-2: Partial optical waveform at 0km (solid line) and 275km (dotted line) .....	24
Figure 2-3: Constellation diagrams at (a) 0 (b) 200 (c) 275 (d) 350 km. ....	26
Figure 2-4: Evolution of 9 representative bits, through 350 km .....	28
Figure 2-5: ECP at 283 km versus rotation angle .....	29
Figure 2-6: Homodyne DDPLL Receiver .....	31
Figure 2-7: ECP for coherent detection (rotated and DDPLL) and DD receivers versus fiber length .....	31
Figure 3-1: Schematic of feed-forward carrier recovery using DSP .....	34
Figure 3-2: Processing unit block diagram.....	35
Figure 3-3: (top) Generated and approximated pdfs of $\Delta\phi$ , (bottom) accumulation of BER integral for the two pdfs .....	42
Figure 3-4: $\log_{10} \text{std} \Delta\phi$ vs. SNR and block size with optimal $Nb$ superimposed. Left: Beat LW of 600kHz, Right: 2MHz .....	43
Figure 3-5: Comparison of $\text{var} \Delta\phi$ from MC simulation and analytical expression .....	43

Figure 3-6: Monte Carlo simulation and analytical BER. Beat LW of (Left)600kHz, (Right)2MHz. .....	44
Figure 3-7: Phase estimation post processing .....	46
Figure 3-8: Example of cycle slip for $LW = 20MHz$ , $\gamma b = 6dB$ , $Nb = 9$ .....	47
Figure 3-9: LW/SNR/ $Nb$ values for FEC limit BER .....	49
Figure 3-10: Theoretical and simulation results for BER floor vs. $Ts\Delta\nu$ .....	50
Figure 3-11: Complex plane graphical representation of $P$ , $LW = 30MHz$ , $SNR = 10.5dB$ , $Nb = 1$ .....	52
Figure 3-12 : Cycle slip probability .....	54
Figure 4-1: Eye diagram simulation; single channel (left) two OFDM channels (right).....	59
Figure 4-2: Experimental setup.....	61
Figure 4-3: Q-factor vs. channel spacing.....	61
Figure 4-4: Simulation (top) and experimental (bottom) eye diagrams for single channel (left) and with adjacent channels spaced at 6GHz (right) .....	62
Figure 4-5: Simulation of 10Gbaud center channel eye, without (left) and with (right) an anti- aliasing filter.....	64
Figure 5-1: Block diagram for DC of the real part of a transmitted signal .....	69
Figure 5-2: Desired and complex IIR GD vs. normalized frequency .....	70
Figure 5-3: ECP as a function of total dispersion/ IIR filter order.....	71
Figure 5-4: Experimental setup for BPSK transmitter/phase diversity receiver.....	72
Figure 5-5: Eye diagrams with and without IIR DC, 80km and 160km .....	73
Figure 5-6: 10GBaud BPSK recirculating loop experimental setup.....	75

Figure 5-7: Q-factor vs. total dispersion/IIR order.....	76
Figure 5-8: Number of operations ratio vs. total dispersion .....	77
Figure 6-1: Symmetric-SSM backward propagation block diagram .....	81
Figure 6-2: Experimental setup for backward-propagation .....	84
Figure 6-3: Q-factor penalty vs. step size for varying $PL$ .....	86
Figure 6-4: Eye diagrams for (a) back-to-back and after 760km with compensation using: (b) CDC (c) Lumped (d) Distributed .....	87
Figure 6-5: Q-factor vs. propagation distance .....	88
Figure 6-6: Desired and complex IIR filter group delays vs. normalized frequency .....	89
Figure 6-7: Eye diagrams for SSM using IIR, complimentary IIR and FFT .....	90
Figure 6-8: Q-factor vs. propagation distance after SSM using various compensation methods	91
Figure 6-9: Wavelet interpolation function $\phi t$ for $s = 5, 39$ .....	94
Figure 6-10: Phase standard deviation vs. total launching power .....	97
Figure 6-11: Impulse response of dispersion compensation FIR filter with IFT, IFT/Tukey and Wavelets-based designs (left), magnitude response (top right) and group-delay response (bottom right). .....	98
Figure 6-12: Performance comparison of IFT/Tukey and wavelets-based FIR filter design vs. filter length. ....	99

## LIST OF COMMON ACRONYMS AND ABBREVIATIONS

ADC	Analog to digital conversion
ASE	Amplified spontaneous emission
BER	Bit error rate
CDC	Chromatic dispersion compensation
DD	Direct detection
DSP	Digital signal processing
EDFA	Erbium doped fiber amplifier
FIR	Finite impulse response
FT	Fourier transform
GD	Group delay
IIR	Infinite impulse response
LO	Local oscillator
LW	Linewidth
NZ-DSF	Non-zero dispersion-shifted fiber
OWDM	Orthogonal wavelength division multiplexing
PRBS	Pseudo random bit sequence
QPSK	Quadrature phase shift keying
RF	Radio frequency
SNR	Signal-to-Noise ratio
SSM	Split-step method
SSMF	Standard single-mode fiber
WDM	Wavelength division multiplexing

## CHAPTER 1. INTRODUCTION

### 1.1. Historical Perspective

The introduction of telegraphy in the 1830s ushered in the era of electrical communication. Telephony followed and became a major driving force in the development and design of many electrical and electronic technologies as the requirement for capacity grew. By the mid-1950s, migration from wire pairs to coaxial cable and microwave allowed the capacity-distance product (a figure of merit used in communication systems) to increase dramatically. Around that time it became clear that order-of-magnitude increase in the capacity-distance product could be attained using optical waves where the carriers are at much higher frequencies allowing wider bandwidths. Two technological barriers hindered the possibility to pursue lightwave communications: the lack of a coherent optical source to provide a carrier to modulate and an optical transmission medium [1]. The first problem was solved with the demonstration of the laser in 1960 by T. Maiman [2]. Attention was drawn on utilizing the new light source for communication application. Many ideas were put forth as to the design which would allow transportation of the modulated lightwave; ultimately, the prevailing idea which is used till today is the optical fiber, as suggested by Kao and Hockham [3]. At that time, the high losses of optical fibers (in excess of  $1000\text{dB}/\text{km}$ ) prevented implementation of lightwave communication systems. When fiber losses were reduced to below  $20\text{dB}/\text{km}$  and with the introduction of the semiconductor lasers, the road was paved for the nascent technology to emerge as the backbone for the worldwide telecommunication network. The increase in capacity-distance product has been approximately six orders of magnitude between 1975 and

2000 [4], roughly doubling every year. The advancement of lightwave communication technology is divided to several generations, each building upon and improving the previous.

Gallium Arsenide (GaAs) semiconductor lasers (at a wavelength of  $0.8\mu m$ ) were used in the first lightwave systems generation. As with other communication systems, periodically-spaced repeaters (where data is received and re-transmitted) were placed to detect and re-transmit the signal. The repeater spacing was approximately  $10km$ , as compared to  $1km$  for coaxial systems, which reduced the installation and maintenance costs. Beyond the actual capacity, repeater spacing increase was another fundamental drive to migrate to lightwave systems. Fiber loss at a wavelength of  $1.3\mu m$  is lower than at  $1\mu m$ . Moreover, the optical fiber minimum dispersion wavelength is  $1.3\mu m$ . The requirement to extend repeater spacing drove development efforts of the InGaAsP semiconductor lasers and detectors which operate at  $1.3\mu m$ . The second generation lightwave systems operated at this wavelength and using single-mode fibers the bit-rate limitation due to modal dispersion was alleviated. Third generation systems operated at  $1.55\mu m$  where the fiber loss is minimal while dispersion is still manageable. Electronic repeaters were still required every  $60 - 70km$ . The required repeater spacing could be extended using coherently-detected systems. Moreover, potential benefits of coherently-detected systems such as superior sensitivity have been extensively demonstrated [5]. The invention (By D. Payne, [6]) and rapid commercialization of the Erbium-doped fiber amplifier (EDFA) starting in the mid-80s has halted further development of coherent systems and commercial deployment never materialized. Fourth generation systems utilize optical amplification which allows an increase in repeater spacing and wavelength-division multiplexing

(WDM), increasing the bit-rate. Thus, lightwave communication systems have become the primary means of information transportation on a global scale.

## **1.2. Modern Perspective**

The ultimate goal of any optical fiber communication system is to provide the highest information throughput for a given transmission distance. The required transmission distance dictates the system configuration to be used; transmitter, fiber and receiver architectures are all designed to accommodate the capacity/distance requirements while considering the cost constraints. Optical fibers are utilized in a range of communication applications, from very short links using plastic multi-mode fibers to trans-oceanic multi-channel systems employing several types of fused-silica single-mode fibers. Laying the foundation for information theory, Shannon provided the fundamental metric for data throughput of a system, known as capacity and measured in bits/s [7]. The notion of capacity may be extended by normalizing the total capacity to a given bandwidth, a measure referred to as spectral efficiency, having units of bits/s/Hz. The spectral efficiency determines not only the maximum theoretical data throughput of a system, but also how efficiently is the total available bandwidth being used.

In general, the spectral efficiency of a specific system is determined by the signal-to-noise ratio (SNR) and the ratio between the utilized and total bandwidth. In a multi-channel setup such as WDM with a fixed total power, the maximum spectral efficiency is an increasing function with channel count and SNR, as shown in Figure 1-1.



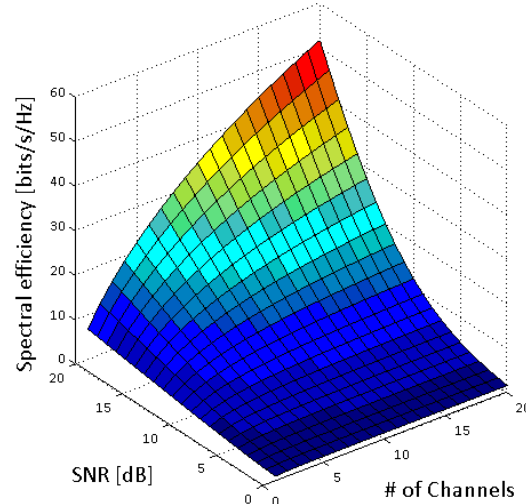


Figure 1-1: Spectral efficiency vs. SNR and number of channels

The best efficiency is then achieved with a larger channel count [8], assuming a band-limited scenario, with fixed power per channel. However, this limits the SNR per channel. Under that limitation, in order to maintain performance a modulation format with the best sensitivity should be employed. The best strategy in this case is to utilize the most degrees of freedom available for modulation. As an example, a polarization-multiplexed binary modulated signal offers higher sensitivity than a 4-level single-polarization amplitude modulated signal. Clearly, the choice of potential modulation formats is dependent on the receiver architecture. In general, three detection schemes are available: non-coherent, differentially-coherent and coherent detection. Of these schemes, only coherent detection preserves complete information of the received optical signal; amplitude, phase, frequency and polarization can all be resolved and become available for further processing as a part of the demodulation process. Still, most (if not all) of the deployed optical fiber systems employ either non-coherent or differentially-coherent detection. This is due to the introduction of the EDFA in the early 90s. Coherent optical technologies were pushed aside as many of the limitations of intensity modulation/direct detection (IM/DD) could be overcome by optical amplification. The EDFA's

wide gain bandwidth coupled with its high gain enabled long haul transmission, up to transoceanic distances. Although coherent receiver sensitivity is up to  $20\text{dB}$  higher than that of IM/DD systems [1], with optical amplification available, the lower sensitivity associated with IM/DD systems was no longer a major concern.

However, as the IM/DD technology is maturing, the advantages of coherent detection are becoming more attractive and it is drawing renewed interest. In a WDM configuration, coherent detection enables higher spectral efficiency through electrical domain channel selectivity, compared to IM/DD system with filtering in the optical domain. Furthermore, coherent detection may also obtain a much higher sensitivity. Even when considering all the above advantages of coherent detection, the commercial deployment of coherent detection systems has been delayed due to the fact that coherent receivers are substantially more complex to implement. Moreover, coherent detection involves several noise sources which degrade the sensitivity, among which are laser phase and intensity noises and polarization mismatch between the incoming signal and local oscillator (LO). All these and more are to be taken into consideration when implementing coherent detection. Current research in this field aims at addressing the issues discussed above with the ultimate goal of taking advantage of all the benefits coherent detection can offer.

At this point, it is important to note that all the above benefits have been considered in the context of coherent detection since the early days of optical communication (e.g., [5, 9, 10]). A crucial element of successful deployment of coherently detected optical transmission systems lies in minimizing the overhead incurred by coherent detection compared to direct or differential detection. The fundamental problem revolves around phase estimation of the

carrier (and LO). Many modulation formats highly compatible with optical fiber transmission are carrier suppressed [e.g., phase-coded-duobinary (PCD) or M-ary phase-shift keying] and thus require carrier recovery to perform phase locking. Even if carrier recovery is achieved, the linewidth (LW) requirements for both the transmitter and LO lasers are a limiting factor. This is due to the fact that the phase-locked loop (PLL) is intolerant to delay in the feedback loop [11]. Receiver architecture which avoids carrier phase locking altogether yet maintains the benefits of coherent detection is essential. Another issue is the alignment of the LO polarization to that of the incoming signal.

Recent advancements in analog-to-digital conversion (ADC) and high-speed digital signal processing (DSP) technology allow the phase estimation to be done without feedback (i.e. without implementation of an electrical or optical PLL). In this case the optical signal is digitized at a rate which allows both impairment compensation (of linear and nonlinear fiber transmission effects) and phase/polarization tracking in the digital domain. It is envisioned that by using proper algorithms all but non-deterministic effects (e.g. amplified spontaneous emission and shot noises) can be almost completely compensated in the digital domain [12, 13]. Coherent detection coupled with DSP technology provides an overwhelming solution to the detection problem of long-haul transmission systems.

Indeed, the coherent detection/DSP approach has attracted tremendous focus in recent years. High-speed sampling and post-processing of the complex received optical field (only available through coherent detection) alleviate the need for phase locking [14]. Moreover, post processing algorithms suggested so far include estimation of the carrier phase, chromatic dispersion, polarization mode dispersion and self-phase modulation compensation [15-17].

Most recently, impairment compensation of both dispersion and nonlinearity using the split-step method (SSM) has been suggested and demonstrated [13, 18]. Much of the current research and implementation extends previous knowledge from the RF to the optical domain while considering noise sources and impairments specific to optical systems (e.g., feed-forward carrier phase recovery for phase modulation has been suggested in the RF domain [19]).

### **1.3. Coherently Detected Optical Systems with Subsequent DSP**

In the 1980s and through the 90s, significant focus was given to the research of coherent lightwave systems [5, 9-11, 20-22]. There were even a few successful field trials (e.g., [23]) but the successful implementation of WDM systems using EDFA technology has been the solution of choice for optical communication systems as the implementation complexity and cost of coherent systems overshadowed its benefits. In the meantime, analog-to-digital conversion (ADC) speeds have increased dramatically [24]. The possibility to convert wide-band analog signals (such as optical signals having multi-Gigahertz modulated bandwidths) to digital signals and subsequently employ channel impairment compensation and demodulation algorithms in the digital domain allows unprecedented flexibility in WDM system architecture design. The degree of freedom DSP allows introduced a myriad of research options and possibilities. The design and integration of the three constituting elements of the optical transmission system (i.e. transmitter, channel and receiver) are now subject to re-examination in light of this advancement.

The outputs from either direct or coherent detection can be handled in the digital domain; however, coherent detection retains complete information about the incoming signal which allows all the available degrees of freedom to be considered in the modulation and

demodulation process. Channel impairments may also be handled to the extent that only non-deterministic effects degrade the performance. With direct detection this is not possible because of loss of the phase information. For these reasons, the combination of coherent detection and high-speed ADC and DSP has drawn tremendous attention in the past few years both in an academic context and commercially. The first demonstration of this approach came in early 2004 with the work of Taylor [25] where the coherent/DSP approach was used to achieve dispersion compensation of  $1470 \frac{ps}{nm}$ . Both Taylor and Noé [26] show the possibility to reduce the complexity of a coherent receiver by using a free-running LO (i.e. without a PLL). The concept of an LO which is not locked to the carrier frequency (homodyning) or away from the signal bandwidth (heterodyning), but is tuned to somewhere around the center of the spectrum is known as intradyning and was first introduced by Derr [27]. Instead of phase locking in hardware, the combined phase of the incoming signal and LO are tracked in the digital domain. In his work, Noé showed that the Viterbi & Viterbi algorithm [19] can be used to achieve phase tracking in the digital domain. The ability to use a free-running LO paved the way for coherent receivers to become simple enough to be considered as an alternative to direct detection.

A torrent of research papers soon followed, several are outline in the following. In 2006 Ly-Gagnon *et al.* demonstrated QPSK transmission and 8-PSK demodulation [28, 29]. In [30] Charlet *et al.* showed transmission of a  $40Gbps$  QPSK signal with  $3060km$  standard single-mode fiber (SSMF) with digital nonlinear phase noise mitigation. Pfau *et al.* were able to achieve real-time operation (although at relatively modest signaling rate of  $400Mbaud$ ) for QPSK modulation using Xilinx Virtex 2 field-programmable gate array (FPGA) [31]. At the end of 2006, Savory demonstrated the ability to demultiplex a polarization-multiplexed QPSK signal

using DSP, which alleviates the need for hardware polarization tracking [15]. The use of higher modulation format (QPSK) with dual polarization quadruples the spectral efficiency compared to an IM/DD channel. In 2007, Goldfarb *et al.* [32] demonstrated the orthogonal-WDM concept which allows ultra-high spectral efficiency, close or even at the theoretical limit [32] by tight channel spacing. A tremendous boost to the coherent/DSP approach from the industrial/commercial aspect was provided by Nortel Networks Corporation with the introduction of a dual polarization Quadrature (2-Pol. QPSK) MODEM; its features are outlined in [33]. In 2008 the ability to post-compensate both linear and nonlinear impairments in fiber was demonstrated numerically by Li *et al.* [13] and experimentally by Goldfarb *et al.* [18]. Efficient DSP algorithms to reduce the amount of operations required by the resource-hungry dispersion compensating operator were introduced in [34] and by Taylor in [35].

All the above mentioned work is limited to receiver-side DSP. DSP can also be performed at the transmitter (or both at the transmitter and receiver); e.g., Roberts *et al.* and Killey *et al.* demonstrated in 2005 and 2006 electronic pre-compensation in SSMF with direct detection [12, 36]. The work presented throughout this dissertation concentrates on receiver-side DSP techniques, since this allows the use of conventional transmitters; the entire compensation and demodulation process can be done at the receiver where adaptive processing may be considered in order to adjust for time-varying parameters in the link. Moreover, in order to take advantage of coherent detection, DSP must be employed at the receiver side. It is likely that implementing DSP both at the transmitter and the receiver would be more costly and complex compared to receiver-side only DSP implementation. As a caveat it is noted that pre-compensation is usually more efficient and better performing (as noted [35]),

since pre-compensation acts on the transmitted signal before the noise is introduced by optical amplification and detection processes. The tradeoff between hybrid (pre- and post-) compensation and receiver-side only should be considered on a case-by-case basis.

Clearly, the implementation of DSP in a real system cannot rely on offline processing as in most of the experimental demonstrations. Consideration of efficiency and computational load must be taken into account. Ongoing academic research is conducted to find better algorithms and real-time compatible implementations which would be of interest not only in an academic context, but also to the industry. Some practical issues are outlined in [37].

#### 1.4. Generic Scheme

A generic transmission system employing coherent detection with subsequent DSP is presented in Figure 1-2.

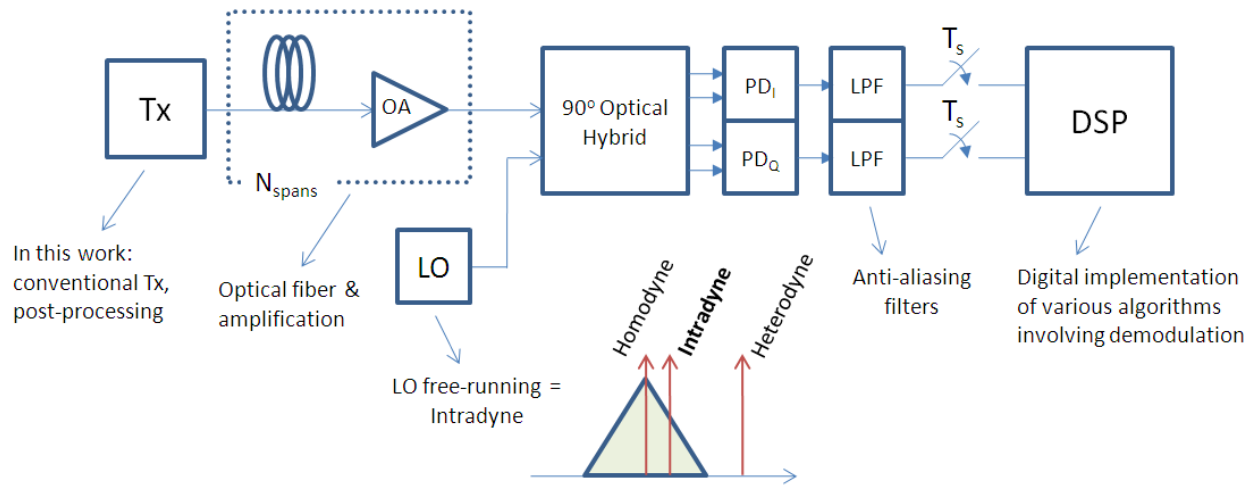


Figure 1-2: Generic transmission scheme with coherent detection and subsequent DSP

As mentioned previously, the work detailed in this dissertation does not involve transmitter (Tx) side DSP. The optical signal is launched into fiber and periodically amplified to

overcome the fiber's inherent loss  $\left(0.2 \frac{dB}{km}\right)$ . After transmission coherent detection is employed. The structure of a  $90^\circ$  optical hybrid is shown in Figure 1-3.

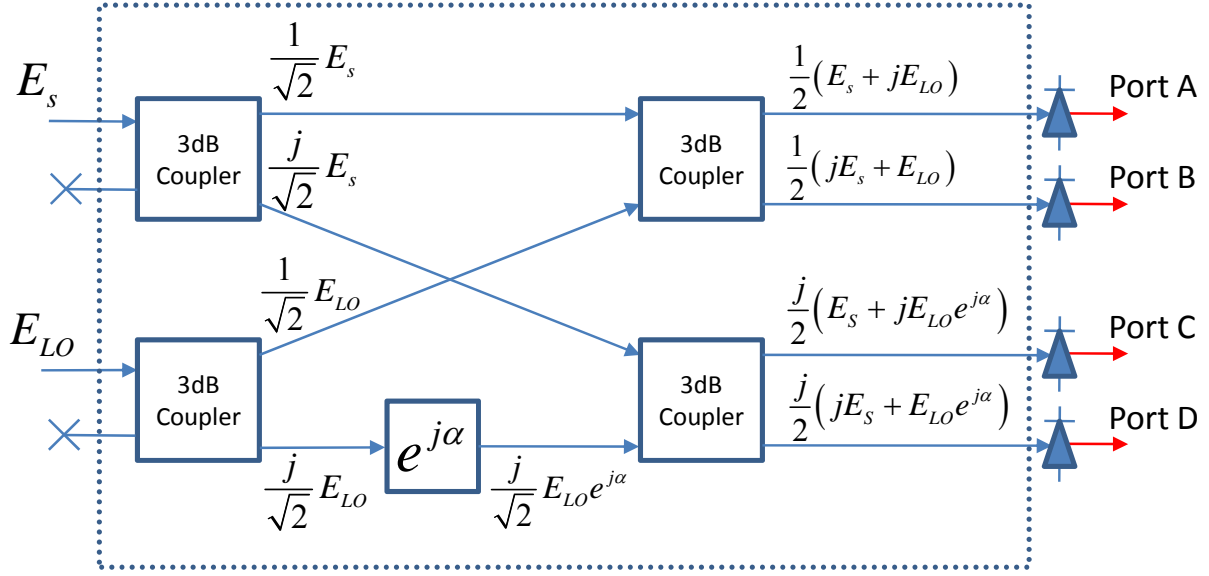


Figure 1-3:  $90^\circ$  optical hybrid

Setting the phase shift to  $\alpha = 90^\circ$ , the electrical outputs [after the PIN photo-detectors (PD) which serve as square-law devices for the optical signal] at ports A-D are given by:

$$\begin{aligned}
 \text{Port A} \quad & \frac{R}{4} [ |E_{LO}|^2 + |E_S(t)|^2 + 2|E_{LO}||E_S(t)| \sin(\Delta\varphi(t)) ] \\
 \text{Port B} \quad & \frac{R}{4} [ |E_{LO}|^2 + |E_S(t)|^2 - 2|E_{LO}||E_S(t)| \sin(\Delta\varphi(t)) ] \\
 \text{Port C} \quad & \frac{R}{4} [ |E_{LO}|^2 + |E_S(t)|^2 + 2|E_{LO}||E_S(t)| \cos(\Delta\varphi(t)) ] \\
 \text{Port D} \quad & \frac{R}{4} [ |E_{LO}|^2 + |E_S(t)|^2 - 2|E_{LO}||E_S(t)| \cos(\Delta\varphi(t)) ]
 \end{aligned} \tag{1-1}$$

where  $E_s(t)$ ,  $E_{LO}(t)$  and are the incoming signal and LO electric fields, respectively.  $\Delta\varphi(t) = \varphi_s(t) - \varphi_{LO}(t)$  is the phase difference between the incoming signal phase and LO phase. The proportionality factor  $R = \frac{\eta q}{h\nu}$  (in  $[A/W]$ ) is the receiver responsivity, where  $\eta$ ,  $q$  and  $h\nu$  are the



quantum efficiency of the PD, electron charge and the photon energy, respectively [38]. There are two options for photodetection: single-ended and balanced detection. The single ended detection is based on using only a single PD, under the assumption that  $P_{LO} \gg P_s$  where  $P_x = |E_x|^2$  is the instantaneous power of the impinging field, which can be time varying (from the signal) or not (LO is continuous wave throughout this dissertation). Moreover, it is assumed that either a DC block or a digital operation are employed in order to eliminate the constant term stemming from the LO constant power. In the single-ended detection case, the obtained signals are proportional to  $|E_s(t)| \sin(\Delta\varphi(t))$  and  $|E_s(t)| \cos(\Delta\varphi(t))$ , the two signal quadratures. In the balanced detection case, the signal from ports A and B and those from C and D (seen in Figure 1-3) are subtracted electrically after the PDs and no assumption needs to be made on the relative power of the LO and signal, nor is a DC block necessary. Balanced detection implementation is more complex, yet it alleviates the problem of relative-intensity noise (RIN) in the LO, as will be discussed in section 1.5. The noise characteristics of both single-ended and balanced detection are practically equivalent. The low-pass filters (LPFs) seen in Figure 1-2 are used to limit the bandwidth of the analog signal (on the two quadratures) before sampling at  $T_s$  to prevent aliasing stemming from the ADC process. Ultimately, the process described above results in the complex optical field being mirrored to the digital domain (at baseband), with no loss of information. A polarization diversity receiver (sensitive to the polarization of the incoming signals) operates in much the same way, with double the hardware necessary. It does, however, provide full information of the vectorial-complex optical field. This dissertation concentrates on a single-polarization signal with the LO always assumed to be co-polarized with the incoming signal polarization.

### 1.5. Noise Sources in Coherent Detection

The fact that full information of the incoming signal is available through coherent detection also implies that this detection scheme is susceptible to noise sources and impairments which are irrelevant to directly detected systems. A common example for this is laser phase noise. With direct detection the phase of the incoming signal is irrelevant since the PD is insensitive to phase (or polarization). Coherent detection is actually sensitive to laser phase noise (of both the signal carrier and LO), resulting in rotation of the constellation at an angle proportional to the carrier and LO instantaneous phase difference. Other noise sources are common to direct (or differential) detection and coherent detection, but manifest themselves differently for each detection scheme. Following is a short discussion of the noise sources affecting coherent detection and DSP.

Several fundamental noise sources exist in a practical receiver: shot noise, thermal noise and dark current. Shot noise stems from the quantum nature of light which dictates that the creation of electron-hole pairs at the detector follows a Poisson distribution. For a large enough number of photons the discrete Poisson distribution may be approximated as a white Gaussian distribution [39]. Thermal noise originates from front-end circuitry and amplifier. Thermal motion of electrons in the front-end load resistance are manifested as current fluctuations, namely Thermal noise [1]. The third noise source is dark current which exists even in the absence of light impinging on the photodetector (e.g., from random generation of electron-hole pairs).

When considering an optically amplified transmission system with  $N_A$  cascaded amplifier stages placed to compensate fiber loss, amplified spontaneous-emission (ASE) noise must be

taken into account. This noise is characterized as additive and white. To see the effect of this additive noise, one may consider the output of one of the 90° optical hybrid ports, e.g., Port A. The incoming signal with additive noise ( $E_s + E_{ASE}$ ) beats with the LO field ( $E_{LO}$ ) to produce the following photocurrent:

$$I = \frac{R}{4} [P_{LO} + P_s + P_{ASE} + 2(\text{Im}\{E_s E_{LO}^*\} + \text{Im}\{E_{ASE} E_{LO}^*\} + \text{Re}\{E_s E_{ASE}^*\})] + i_{noise} \quad (1-2)$$

where  $i_{noise}$  includes all the shot, thermal and dark current noise sources discussed above. In a balanced detection setup,  $P_{ASE}$  will manifest itself through the mixing terms  $E_{ASE} E_{LO}^*$  and  $E_s E_{ASE}^*$  which are referred to as LO-ASE and Signal-ASE beat noises, respectively. Since the LO is usually set much higher than the signal (one is free to arbitrarily increase the LO power, subject to power consumption considerations and detector damage specifications), LO-ASE beat product is the dominant of the two.

The one-sided power spectral-densities (PSDs) for the various noise sources are summarized below, assuming  $P_{LO} \gg P_s$ :

Shot	$S_{SN}(f) = 2qRP_{LO}$	(1-3)
------	-------------------------	-------

Thermal	$S_{TH}(f) = \frac{4k_B T}{R_L}$	(1-4)
---------	----------------------------------	-------

Dark current	$S_d(f) = 2qI_d$	(1-5)
--------------	------------------	-------

ASE-LO beat	$S_{ASE}(f) = 2R^2 P_{LO} N_A n_{sp} (G - 1) h\nu$	(1-6)
-------------	--	-------

where  $k_B$ ,  $R_L$ ,  $I_d$ ,  $n_{sp}$  and  $G$  are Boltzmann's constant, the load resistance, dark current, the spontaneous emission factor and amplifier, respectively [40].

The Shot and ASE-LO beat noises can be made to dominate all other noise sources by increasing the LO power. Moreover, between these two noise sources, ASE-LO beat noise will dominate since the ratio between the two is:  $RN_A n_{sp}(G - 1) \frac{h\nu}{q} \gg 1$ , assuming parameters relevant to optically amplified transmission systems.

Other noise sources affecting the performance of a coherently detected system are phase noise, relative intensity noise (RIN) and polarization mismatch [1, 22]. Spontaneous emission of photons in any laser causes both amplitude and phase to change. In general, laser phase noise broadens the spectrum from a single spectral line to a Lorentzian line-shape. The temporal phase excursion follows a random-walk [41]. The distribution of the phase difference on an interval  $\Delta t$  is Gaussian,  $\Delta\phi(\Delta t) \sim N(0, 2\pi\Delta\nu\Delta t)$  where  $\Delta\nu$  is referred to as the laser linewidth, the width of the Lorentzian line-shape.

Phase noise is a critical topic in coherent systems since coherent systems actually capture this phase variation with time. As seen in Eq. (1-1), the difference between signal and LO phases appears as noise contribution on the coherently detected signal. The end effect of phase noise is to rotate the received constellation at an angle proportional to the instantaneous phase difference between the signal and LO. If not addressed properly, this effect renders demodulation impossible. An example of the effect of phase noise on the constellation is seen in Figure 1-4 (left). Digital phase tracking allows proper demodulation of the signal, with a finite sensitivity penalty; the resulting constellation after correction is seen in Figure 1-4 (right).

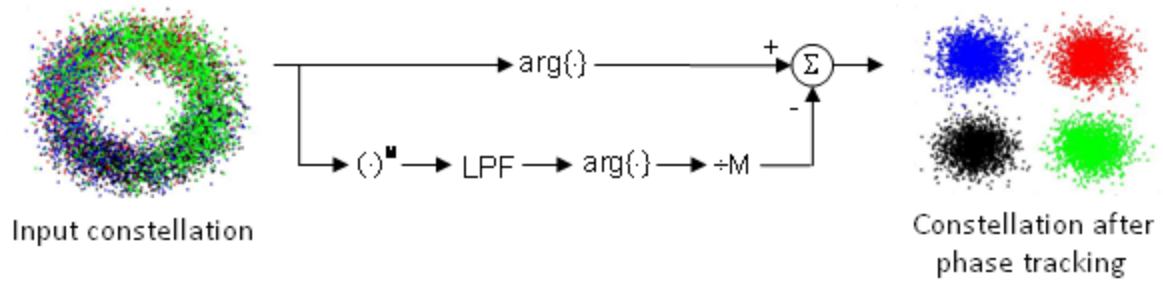


Figure 1-4: Effect of phase noise on constellation and correction

Another noise source coherent detection suffers from is relative intensity noise (RIN). Spontaneous emission causes not only phase noise, but also intensity fluctuations at the laser output. RIN is modeled as a zero-mean, wideband Gaussian process [22]. The effect of RIN can be appreciated by noting in Eq. (1-2) that the powers of the LO and signal ( $P_{LO}, P_S$ ) both appear. Fluctuations in the power levels are manifested as noise. RIN is not a major contributor to degradation in sensitivity since balanced detection can be used to eliminate the stand-alone power terms [9]. Clearly, the power fluctuations still play a role even if balanced detection is employed, but the effect is limited since the LO and signal beat power terms appear under a square root operator [1].

Lastly, the polarization mismatch between the LO and signal may lead to degradation in sensitivity. The treatment presented above assumes perfect polarization matching between the LO and signal, while in practice a mismatch between the two would cause the (desired) interference term to decrease as a function of the angle mismatch [1]. A solution to this problem is the polarization-diversity receiver [9], which captures both polarization tributaries of the incoming signal. Indeed, this setup doubles the amount of required components for coherent detection; however, polarization multiplexing can be employed in this case and the doubling of hardware translates to doubling in data throughput. Polarization of the incoming

signal changes with time due to fiber birefringence. Polarization tracking may be achieved in the digital domain. One possibility to do so is using the constant-modulus algorithm which is employed adaptively due to the time-dependence of the polarization state of the incoming signal [42].

Another noise source which must be considered is associated with the ADC resolution, namely the quantization noise. The ADC process has a finite resolution depending on the number of quantization bits used. The process of converting an analog signal (which is continuous in magnitude by nature) to a digital one (described by discrete levels) is a nonlinear noise process. This noise contribution as it affects coherent optical systems was investigated in [36, 43]. With enough effective bits, the added quantization noise does not present a significant contributor to signal quality deterioration and will be discarded throughout this dissertation.

## **1.6. Dissertation Outline**

This dissertation is sectioned into the several main topics of research, with the aim of presenting the work with an ascending level of complexity as it pertains to the various transmission regimes and issues associated with each regime. In Figure 1-5, the various topics covered in this dissertation are shown in order.

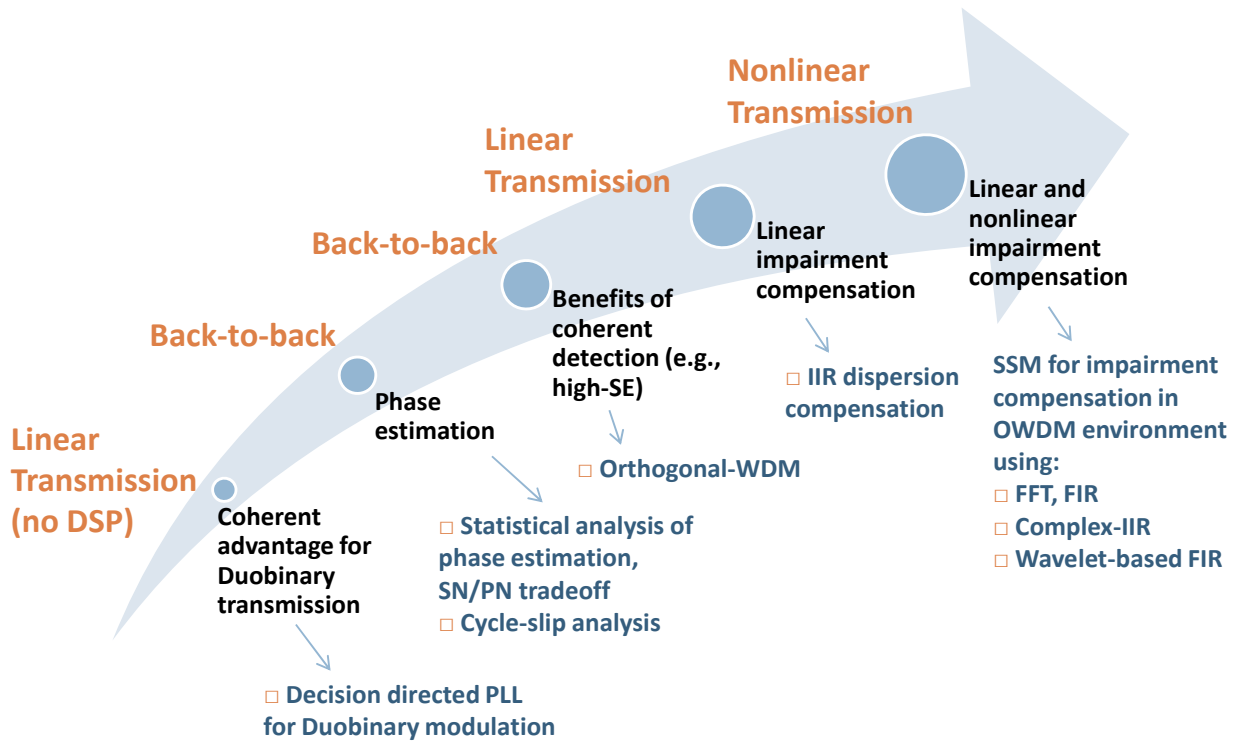


Figure 1-5: Arrangement of dissertation

The first topic addressed is the use of coherent detection to improve the dispersion limit of a duobinary signal. This was demonstrated (through simulation) by observing the evolution of the constellation diagram of a duobinary signal as it propagates through fiber. The dispersion limit can be improved by approximately 33%, as will be shown in chapter 2. The feasibility of using coherent detection in the case of PCD modulation was demonstrated through the use of a decision-directed PLL [44] specifically designed to be compatible with the PCD transmitted signal. This chapter presents preliminary work in the field of coherent detection; however, it does not directly relate with the use of DSP in conjunction with coherent detection. In chapters 3 to 6, research involving coherent detection/DSP techniques is presented.

One of the major issues concerning the DSP architecture was to analytically determine the bit error rate (BER) curves associated with the DSP algorithms used for demodulation. As a first step in the research, an analytical approximation of the BER of a power-law feed-forward

carrier recovery scheme was established [45]. This analytical approximation enables one to determine various parameters associated with to the DSP algorithm used for phase estimation without resorting to time and resource consuming Monte Carlo simulations. This work is presented in CHAPTER 3.

Coherent detection is often quoted as allowing very tight channel spacing due to the fact that channel demultiplexing is performed in the radio frequency (RF) domain rather than the optical domain. This is a critical feature as the spectral efficiency limit may be reduced considerably when using coherent detection. Theoretically, WDM channels can be packed at the symbol rate (e.g. 10GHz channel spacing is possible for a 10Gbaud system), when the proper transmitter and receiver pulse shapes are employed. It was experimentally demonstrated that although significant spectral overlap exists between channels, these can still be spaced at the symbol rate with relatively small penalty. Experimental demonstration of spectral efficiency close to  $1 \frac{\text{bits}}{\text{s}\cdot\text{Hz}}$  for binary modulation is presented in chapter 4.

The research topics presented earlier concern the transmitter and receiver architecture. Following is research regarding the mitigation of the transmission channel (fiber) impairments, namely, chromatic dispersion and Kerr nonlinearity.

Compensation of linear channel distortion (known in general as equalization) can be implemented in either analog or digital domain for RF signals. For optical signals experiencing chromatic dispersion, chromatic dispersion compensation (CDC) fibers or electronic CDC can be used. Equalization using electrical signal processing techniques have also been suggested in the early 90's [46], but only recently ADC and DSP technology have reached a stage where



mitigation of various optical impairments can be done in the digital domain, making this approach compatible with high-speed optical signals. One of the major challenges in achieving CDC is the high number of operations needed to perform this task. Traditionally, CDC (using DSP) is achieved using finite impulse response (FIR) filtering. The number of (complex) FIR taps required for dispersion compensation may vary depending on how the FIR filtering is implemented (e.g. constant tap values [25] or combination of constant and adaptive taps [15]). Infinite impulse response (IIR) filtering is considered as an alternative to FIR approach since IIR filters have a feedback path which allows reduction of the number of operations required for this task. A general approach of using IIR filtering for CDC is suggested in [34]. This work is discussed in chapter 5.

Fiber nonlinearity is another major contributor to the deterioration of quality of an optical signal transmitted in fiber. More specifically, the interaction between dispersion (which causes power fluctuations) and nonlinearity (which translates these power fluctuations to phase fluctuations) leads to a large penalty. In a nonlinear channel, such as optical fiber, the traditional approach of launching a stronger signal to combat the deterioration of signal quality with propagation may fail. Optical spectral inversion [47], dispersion management, [1] or other techniques (e.g., [12]) may be used to mitigate this problem. However, digital post-compensation is highly beneficial as adaptive compensation is possible. Moreover, the use of receiver-side DSP is an enabling architecture for high spectral efficiency and advanced modulation formats. Digital post compensation of both chromatic dispersion and nonlinearity was suggested in [13], where the authors outline the architecture for real-time implementation

of this feature. An offline demonstration of distributed impairment compensation was recently accepted for publication [18]. Research on this topic is presented in chapter 6.

Summary and conclusions are included in chapter 7. The various issues pertaining to real-time implementation of DSP are considered and current open challenges involving the coherent/DSP architecture are discussed.

## CHAPTER 2. DUOBINARY TRANSMISSION USING COHERENT DETECTION

In this chapter, research related to the improvement of the chromatic tolerance of a phase-coded-duobinary (PCD) signal is presented. Observation of the evolution of the duobinary signal constellation diagram as it propagates in fiber shows that coherent detection can be used to improve the dispersion limit compared to direct detection (DD) by 33%.

### 2.1. Introduction

PCD modulation over standard single-mode fiber (SSMF) has attracted significant attention due to a multitude of factors. Compared to binary modulation, it occupies half the bandwidth yet enjoys the same sensitivity. Its simple implementation [48], high tolerance to chromatic dispersion, [49-52] and improved spectral efficiency [52, 53] are all desirable properties for wavelength-division multiplexing (WDM) transmission systems. A PCD signal is obtained as shown in Figure 2-1(left). The PCD signal is reversed in its intensity compared to the binary input, making it straightforward to detect using either DD or coherent detection. Moreover, it is readily seen that its amplitude levels never swing between two extremes (-1 and +1 marks) without going through a space. This fact explains the reduced bandwidth of the duobinary signal, compared with a binary non return-to-zero (NRZ) signal. This is shown in Figure 2-1(center) where the PCD and NRZ signal spectra are superimposed. Also seen is the fact that the PCD signal is carrier suppressed, thus reducing nonlinear transmission impairments.

Figure 2-1(right) shows the constellation diagrams for NRZ, IM/Duobinary and PCD where the IM/Duobinary is similar to the PCD without subtracting 1 after the delay-and-add sequence. Using these constellations, it is readily shown why the PCD signal bears no sensitivity penalty compared with NRZ. The distance between constellation points is calculated assuming equal

average powers for the different signal types. The average power  $P$  is obtained by multiplying the power for each symbol by its respective probability. For NRZ:  $P = \frac{1}{2}0^2 + \frac{1}{2}d_1^2$ , IM duobinary:  $P = \frac{1}{4}0^2 + \frac{1}{2}d_2^2 + \frac{1}{4}(2d_2)^2$  and for PCD  $P = \frac{1}{4}(-d_3)^2 + \frac{1}{2}0 + \frac{1}{4}d_3^2$ . This results in the following relationship between constellation symbol distances:  $d_1 = d_3 = \sqrt{3}d_2$ . Hence, the symbol distances for the NRZ and PCD cases are equal (no sensitivity penalty). Noting that IM/Duobinary is not carrier-suppressed; sensitivity penalty is thus incurred with this signal.

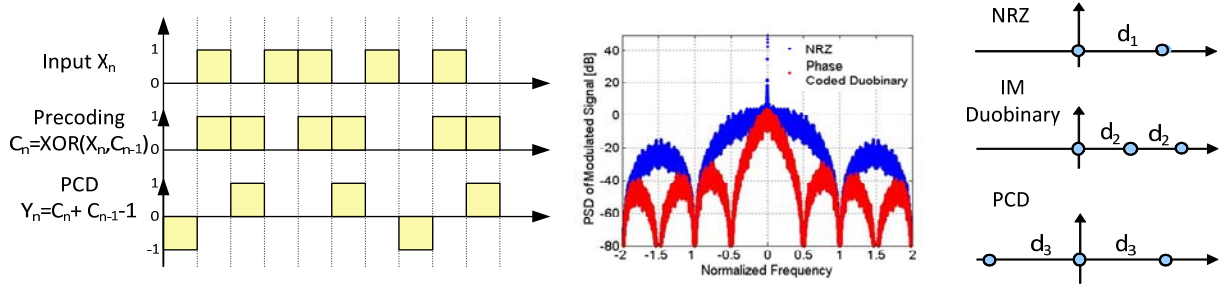


Figure 2-1: (left) Generation of PCD signal, (center) NRZ and PCD spectra, (right) NRZ, IM/Duobinary and PCD constellations

Through simulations and experiments, it is generally accepted that dispersion tolerance of a  $10\text{GBaud}$  PCD signal with DD is about 200km in SSF. The underlying waveform distortion mechanism due to fiber dispersion is investigated by observing the (complex) field rather than the (real) intensity of the duobinary signal. Numerical simulations show that the optical constellation of the transmitted signal is distorted compared to the constellation at the input, directly resulting in eye closure penalty (ECP) for a DD receiver. In the case of coherent detection, this distortion does not necessarily lead to significant eye closure. With coherent detection, the dispersion limit corresponding to 1dB ECP is 283km compared to 213km for the DD case. To show the feasibility of this approach, a phase locking scheme compatible with the

PCD modulation format is suggested. Simulations show that the suggested scheme achieves this dispersion limit.

## 2.2. Evolution of the Duobinary Constellation Diagram

Consider a 10Gbaud PCD signal generated by a standard duobinary transmitter [48]. A precoded binary signal is filtered using a 5<sup>th</sup>-order Bessel low-pass filter (LPF) with a cutoff frequency of 2.8GHz to obtain a 3-level duobinary signal. A properly biased 7GHz Mach-Zehnder modulator is used to produce an optical PCD signal. The use of a Bessel LPF to achieve duobinary coding has been shown to be advantageous compared to the delay-and-add method in terms of ease of implementation and dispersion tolerance [50]. The solid lines in Figure 2-2 show the intensity and phase of a typical phase-coded duobinary signal at the transmitter. The optical signal is transmitted through a SSF (  $D = 16 \frac{ps}{km \cdot nm}$ , nonlinearity was not considered).

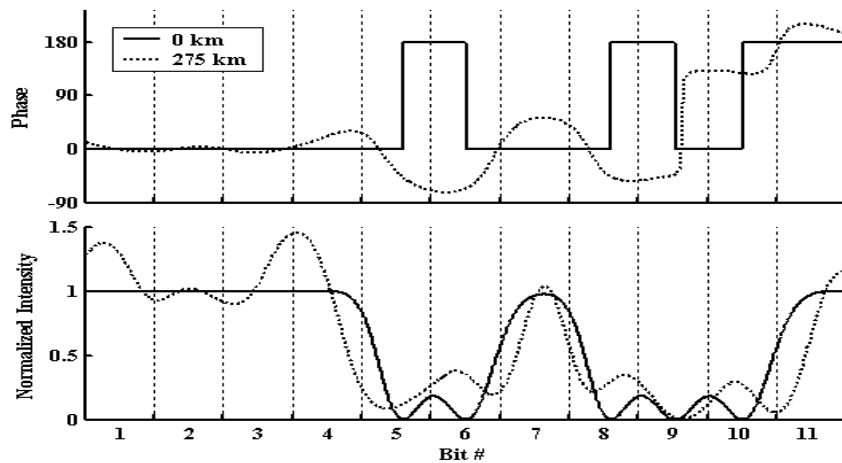


Figure 2-2: Partial optical waveform at 0km (solid line) and 275km (dotted line)

Duobinary coding dictates that the phase flips (between 0° and 180°) at the middle of each space[49] (e.g., bits #5 and #6 in Figure 2-2, 0km). As a Bessel LPF is used for duobinary coding, there is always finite energy within the space bit slot. The phase flip, combined with this

finite energy causes destructive interference between the energies on either side of the middle of the space, enabling confinement of the energies as the signal propagates. When the energies on both sides of a space are not equal, destructive interference will not be preserved as the signal propagates and energy will be transferred from one side of the space to the other. Accompanying this energy transfer, the relative phase on the two sides of the space deviates from  $180^\circ$ . To demonstrate this, the dotted lines in Figure 2-2 show the intensity and phase at a transmission distance of 275km. Taking bit #6 as an example, the energies on both sides of the middle of this bit do not maintain a relative phase of  $180^\circ$  after transmission. Starting at roughly 250km, the relative phase is maintained around  $180^\circ$ , causing rapid eye closure. By comparison, bit #9's energy doesn't change significantly with propagation, owing to the balanced energy levels on both sides of the middle of this bit. The same argument can be applied to bits #2 and #7, for example. In fact, at the first stage of transmission, a pulse (centered at bit #7 for example) can actually be compressed before broadening. Broadening will eventually occur at longer transmission distances as the energies of bits #6 and #8 are not equal to that of bit #7.

Both intensity and phase evolution can be better illustrated on the constellation diagram. Figure 2-3 shows the constellation diagrams at distances of 0, 200, 275 and 350km. The constellation of the (normalized) duobinary signal at the input is plotted in Figure 2-3(a). The finite energy in the spaces (due to the use of a Bessel filter to generate the duobinary signal) is clearly shown by the multiple points near the origin, as opposed to the ideal single point at the origin when no filter is used. The change in the constellation up to 350km transmission is clearly seen in Figure 2-3(b-d). Each constellation point at the transmitter

disperses into roughly a line due to data pattern effects. Furthermore, the three lines corresponding to the space and +1 and -1 marks are almost parallel. This type of constellation diagram consisting of three nearly parallel lines exists for a wide range of transmission distances, up to . This behavior of the constellations at various transmission distances was observed for pseudo-random bit sequence (PRBS) of length to . Higher PRBS orders were not simulated due to lack of available computational resources. The concentric circles superimposed on the plots in Figure 2-3 assist in demonstrating the limitation when using DD. When DD is used, the intensity of each bit is measured and compared with a threshold to distinguish between marks and spaces. At (Figure 2-3b) the maximum intensity of spaces and minimum intensity of marks get closer, making erroneous bit detection more probable.

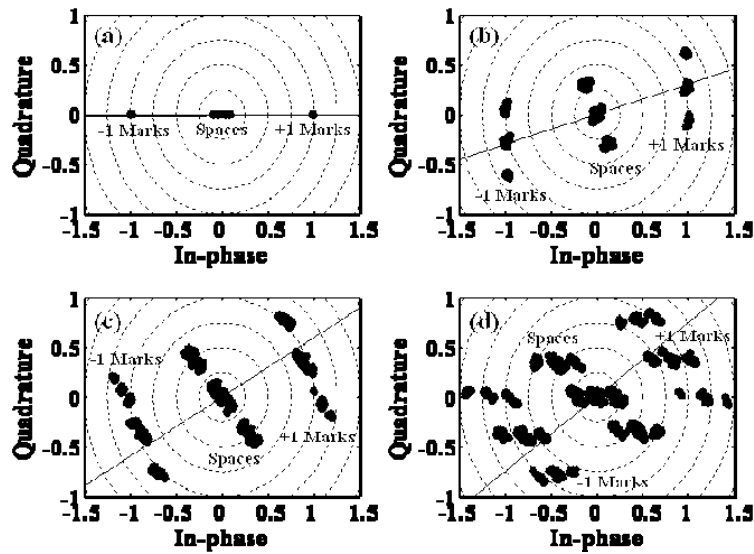


Figure 2-3: Constellation diagrams at (a) 0 (b) 200 (c) 275 (d) 350 km.

In Figure 2-4, traces of 9 bits are plotted in the complex plane as a function of distance. The numerical designations of the bits in Figure 2-4 correspond to those in Figure 2-2. These bits were verified to be qualitatively representative of all the bits in the PRBS. By mapping each

bit trace in Figure 2-4 to the associated bit in the waveform, it is possible to isolate which characteristics of the waveform lead to the constellation diagram distortion. Each trace has 5 crosses on it, marking increasing propagation distances of 0, 150, 200, 275 and 350km. Figure 2-4 reveals that some bits deviate significantly from their initial positions. The symmetry observed in Figure 2-4 allows determination of the conditions leading to the distortion of the constellation by observing only bits #4, #7 and #10, without loss of generality. As seen in Figure 2-4, bit #7 (+1 mark) shows the largest deviation from its initial position. Referring to the optical waveform in Figure 2-2 reveals that this bit is a mark adjacent to two spaces, implying large energy difference on both of its sides. It is observed that bit #7 starts to lose energy to the adjacent spaces at roughly 200km transmission and its phase relative to those of the adjacent spaces is maintained almost constant at about  $90^\circ$  (e.g. bits #6 and #7), allowing the energy in the spaces (marks) to grow (diminish) efficiently. However, the vector distance between the spaces and marks  $[(+1, -0), \text{ or } (-1, +0)]$  does not necessarily decrease substantially because the marks and spaces rotate in the same direction. This rotation is responsible for the formation of the three lines in the constellation observed in Figure 2-3. Bit #4 (a +1 mark) is seen in Figure 2-2 as adjacent to only one space. Hence, the severe effect seen in bit #7 is less significant for bit #4. Bit #10 is a space adjacent to a mark and another space. The argument regarding bit #4 still applies to bit #10, but now (being a space) bit #10 extracts energy from its adjacent mark. The constellation diagrams in Figure 2-3 not only reveal the dispersion limit for DD but also suggest the use of coherent detection as a means for improved dispersion tolerance.



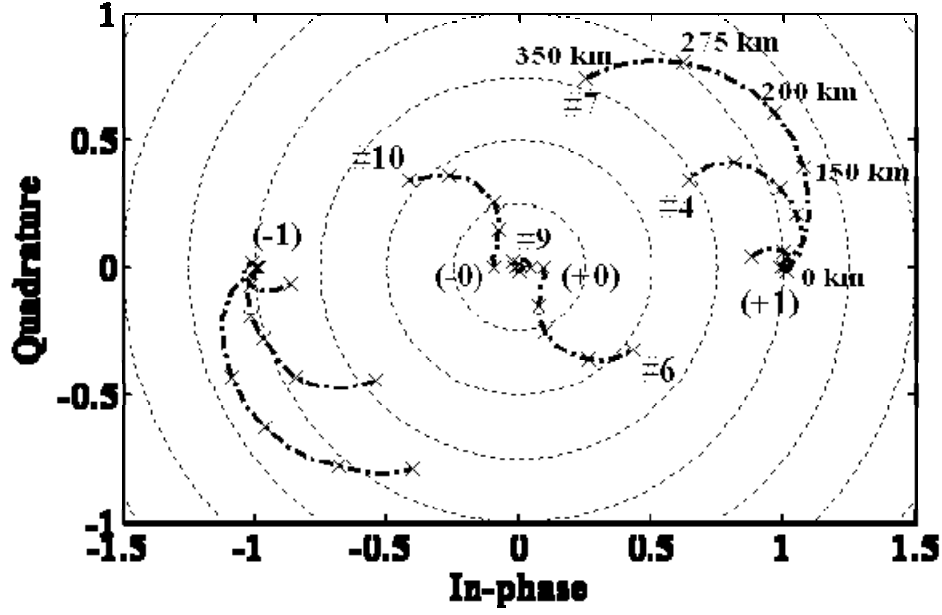


Figure 2-4: Evolution of 9 representative bits, through 350 km

### 2.3. Chromatic Dispersion Tolerance of Direct and Coherent Detection

In DD, the receiver consists of a PIN photodiode detecting the power of the received optical signal [48]. When DD is used, the eye opening is the difference between the intensities of the mark closest to the origin and the space farthest from the origin. From Figure 2-3(c) it is seen that the DD eye is almost closed at a transmission distance of \_\_\_\_\_ since the largest intensity of the spaces is almost equal to the smallest intensity of the marks. However, when considering coherent detection, the constellation is rotated at an angle determined by the phase of the local oscillator (LO). Using the received signal and the LO as inputs to a \_\_\_\_\_ optical hybrid, the outputs from the hybrid can be detected using balanced detectors to obtain the in-phase and quadrature electrical signals: \_\_\_\_\_ and \_\_\_\_\_ where \_\_\_\_\_, \_\_\_\_\_ and \_\_\_\_\_ are the signal and LO powers, and \_\_\_\_\_ signal and LO phases, respectively. The signal phase is modeled as \_\_\_\_\_

where  $\varphi_{data}(t)$  is the duobinary signal phase and  $\varphi_{disp}(t)$  is the contribution to the phase from chromatic dispersion.

The ECP of the in-phase signal can be minimized by rotating the constellation diagram corresponding to a constant value of  $\varphi_{LO}$  for each distance (solid lines on Figure 2-3 demonstrate these angles at various distances). In the coherent detection case there are two eyes for the received signal as  $x(t)$  is proportional to a cosine function which can be positive or negative. The worst ECP of the two eyes was used. A comparison of DD and coherent detection (using a constant LO angle) ECP versus fiber length is presented in Figure 2-7. The 1dB ECP propagation distance for the coherent receiver is 283km, compared to 213km for DD.

The impact of phase locking accuracy is estimated by observing the ECP while varying the LO phase around the angle achieving minimal ECP. Large tolerance to locking accuracy was observed for all fiber lengths (e.g. 26° for 1dB additional ECP at 283km, Figure 2-5).

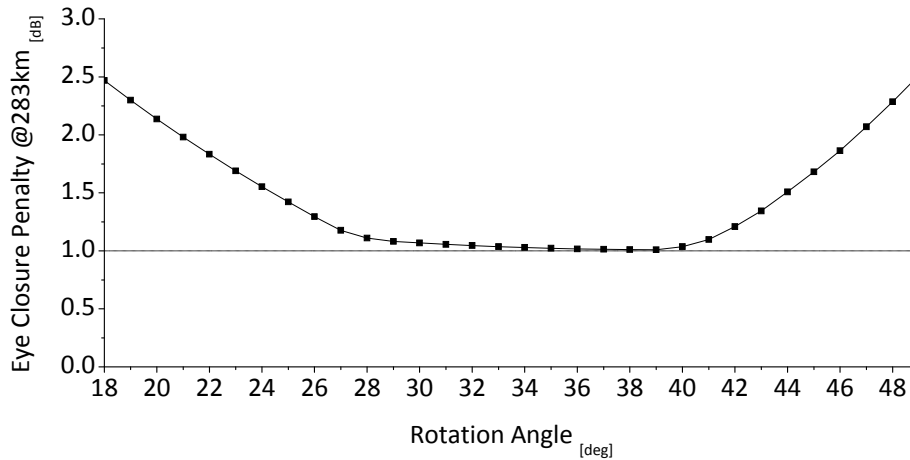


Figure 2-5: ECP at 283 km versus rotation angle

Although the ECP obtained by rotating the received constellation can be used to obtain a general estimation of the benefit of coherent detection, it is essential to show that coherent

detection can be implemented in a practical manner. Figure 2-6 describes such an implementation using a decision-directed phase-locked loop (DDPLL) [54]. The signals  $x(t)$  and  $y(t)$  are sampled using sample-and-hold circuits. The decision circuit determines the

demodulated output  $D_n = \begin{cases} 1 & |x_n|^2 > \frac{\langle P_x \rangle}{2} \\ 0 & \text{else} \end{cases}$  and a feedback coefficient

$$c_n = \begin{cases} 1 & D_n = 1 \\ -1 & x_n^2 + y_n^2 > \frac{\langle P_x \rangle}{2} \text{ and } D_n = 0 \\ 0 & \text{else} \end{cases}, \text{ where } \langle P_x \rangle \text{ is the average power of } x(t). \text{ For a 1}^{\text{st}}$$

order DDPLL, the LO phase is updated according to  $\hat{\phi}_n = \hat{\phi}_{n-1} + k c_n \text{atan}\left(\frac{y_n}{x_n}\right)$ . Coefficient  $k$  may be varied during acquisition and tracking stages. In the acquisition stage a larger value is chosen to promptly obtain phase locking, while in the tracking stage a smaller value ensures slower response to phase noise, thus minimizing tracking error. For the spaces close to the origin,  $c_n = 0$ . This causes the loop to disregard the phase estimation from these spaces as they have random phase distributions between  $0^\circ$  and  $360^\circ$ . Numerical simulation shows that choosing  $c_n = 1$  for all marks and  $c_n = -1$  for the spaces far from the origin ensures successful locking and stable tracking.

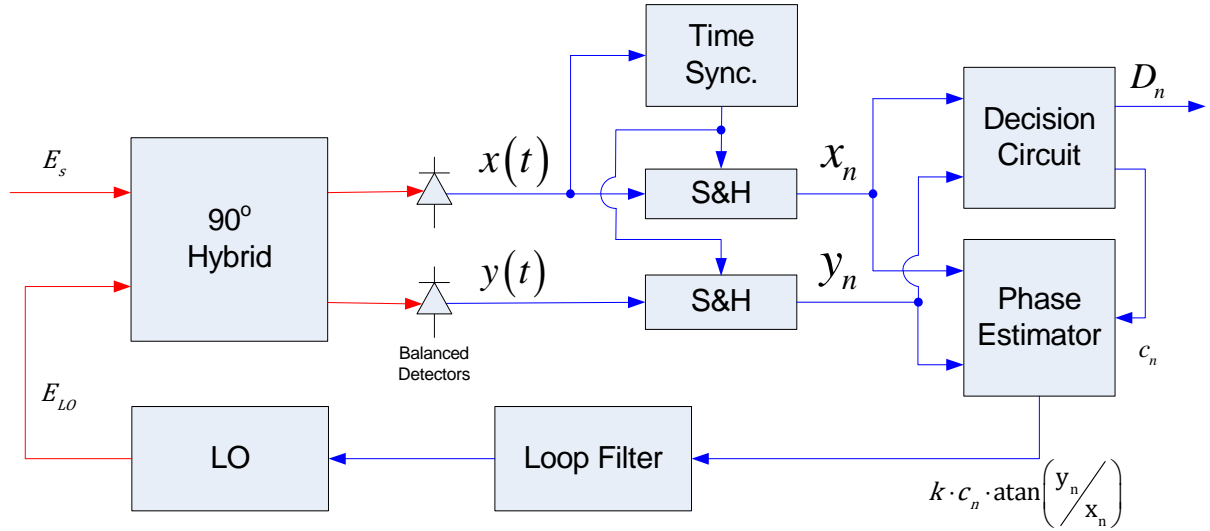


Figure 2-6: Homodyne DDPLL Receiver

Figure 2-7 also shows the ECP of the in-phase signal  $x(t)$  obtained when using DDPLL. Use of the DDPLL incurs a negligibly small added penalty at 283km. The DDPLL may even achieve lower ECP compared to the constant LO phase case at specific transmission distances (e.g., 200km). This can be explained by the adaptive nature of the feedback loop. The coefficient  $c_n$  dictates that the angles of spaces and marks are compensated separately when using DDPLL, as opposed to the constant LO phase case where the marks and spaces are rotated jointly.

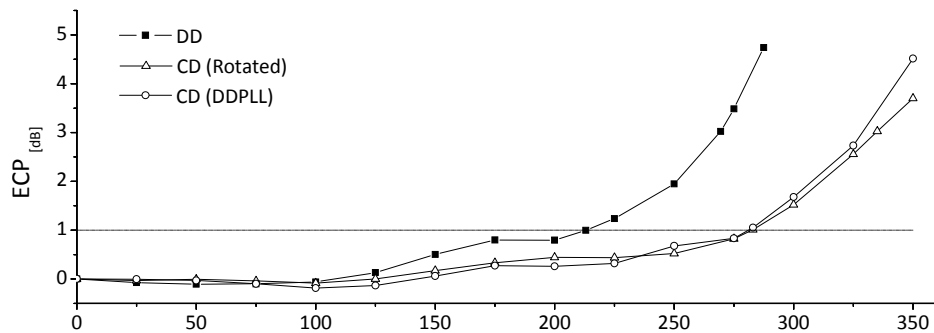


Figure 2-7: ECP for coherent detection (rotated and DDPLL) and DD receivers versus fiber length

Hence, coherent detection achieved through the use of DDPLL is shown to be beneficial compared to DD. Clearly, the ECP is only a first-order estimate of the performance. Use of coherent detection involves various noise sources (e.g. transmitter laser and LO phase noise) not present in the DD case. These noise sources have not been considered here and will contribute to degradation of the system performance.

## 2.4. Conclusions

The effect of chromatic dispersion leading to the distortion of the constellation diagram of a PCD optical signal was studied using numerical analysis. Through comparison between the optical waveform and corresponding constellation it was determined that the energy imbalance on both sides of a space combined with the phase flip ( $0^\circ$  to  $180^\circ$  and vice-versa) incurred by the duobinary modulation format will eventually cause this distortion. This distortion may be compensated by using coherent detection which shows a  $1dB$  ECP at  $283km$  compared to  $213km$  for the DD case. A DDPLL type receiver is suggested as a possible implementation for coherent detection compatible with the duobinary received signal.

## **CHAPTER 3. FEED-FORWARD CARRIER PHASE ESTIMATION**

### **3.1. Introduction**

In coherent detection, the best sensitivity is achieved when homodyne detection is used [55]. However, in this case both the transmitter and local oscillator (LO) lasers need to have narrow linewidths (LWs) and be phase-locked. These requirements render the realization of a homodyne receiver difficult to implement. To circumvent this problem, several receiver schemes employing high-speed digital signal processing (DSP) have been suggested [14, 28, 56]. These schemes maintain the advantages of homodyne detection without phase locking, using instead digital feed-forward carrier recovery. Analytical expressions which quantify the performance of such architecture are invaluable since the alternative is time-consuming Monte Carlo (MC) simulations.

In this chapter, an approximate analytical expression for the bit error rate (BER) of a quadrature phase shift keying (QPSK) homodyne receiver employing digital signal processing for carrier recovery is presented [45]. The BER estimated using the analytical expression is in excellent agreement with MC simulations. The analytical approximation leads to an intuitive understanding of the tradeoff between signal-to-noise ratio (SNR) and LW using this carrier phase estimation algorithm and allows optimization of system parameters without resorting to MC simulations. The phenomenon of cycle-slips in feed-forward phase estimation algorithms is addressed and analyzed at the end.

### **3.2. BER Estimation for QPSK Homodyne Detection**

The scheme in [16] demonstrates an intuitive approach to feed-forward carrier estimation for optical QPSK using DSP. This scheme is highly compatible with DSP

implementation of carrier phase recovery of carrier-suppressed modulation formats. The algorithm presented here is by no means the only possible solution to carrier phase recovery using DSP; however, it is relatively simple to implement and its analysis is relevant to all power-law schemes which are based on the Viterbi & Viterbi algorithm [19].

The digital feed-forward carrier recovery scheme under consideration is shown in Figure 3-1. A phase diversity receiver is used to obtain both quadratures of the received signal. Details are provided for the first  $N_b$  bits, without loss of generality. The scheme can be generalized to any number of digital signal processing units (PUs).

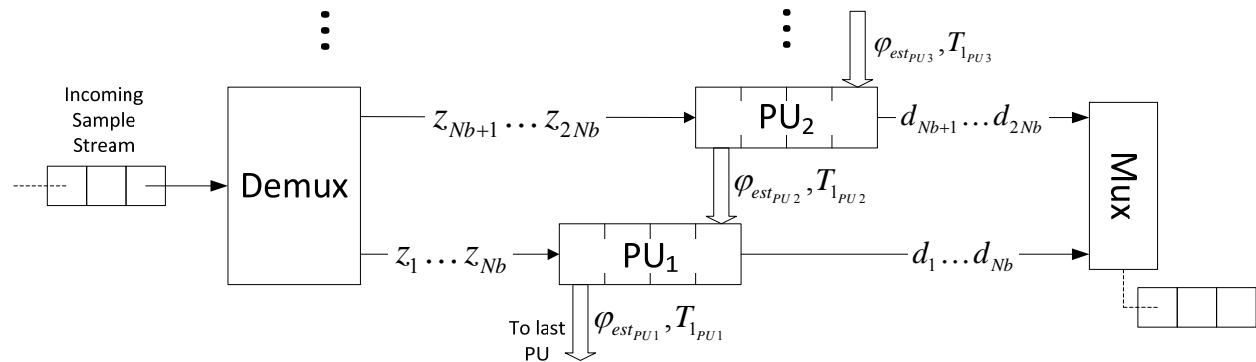


Figure 3-1: Schematic of feed-forward carrier recovery using DSP

Figure 3-2 shows the PU block diagram. This scheme is referred to as a block-window accumulator scheme since the carrier phase estimation is based on a common phase estimate for  $N_b$  samples, which are segmented into blocks. Noè [14] presents a similar scheme for which each phase estimate is unique to each sample. The neighboring samples are used for shot noise filtering. Noè's scheme is referred to as a gliding-window accumulator scheme. The performance was found to be similar when no frequency offset between carrier and LO exists.

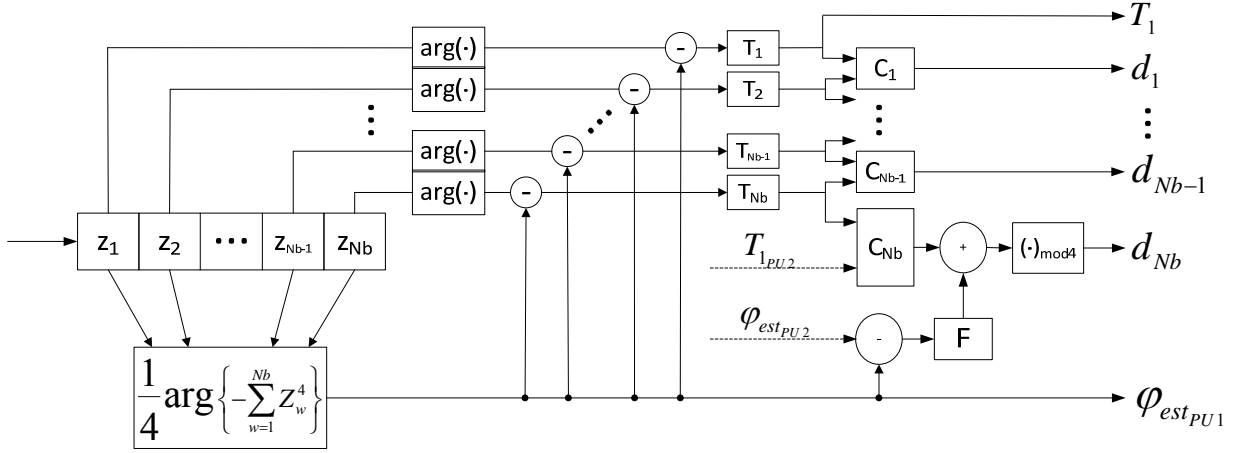


Figure 3-2: Processing unit block diagram

The complex received signal can be written as  $z_k = e^{j(\varphi_{d_k} + \varphi_k)} + n_k$  where  $\varphi_{d_k} = \left(d_k + \frac{1}{2}\right)\frac{\pi}{2}$ ,  $\varphi_k$  and  $n_k$  are the data phase modulation, carrier phase error (with the LO phase as reference) and shot noise, respectively.  $d_k$  is the differentially encoded quadrant number associated with the QPSK data stream, as in [14], and  $n$  is a complex zero mean Gaussian random variable (RV) characterized by  $n \sim N(0, \sigma_n^2)$ . The received signal  $Z_k$  is first demultiplexed so that each PU collects  $N_b$  samples for which the carrier phase is to be estimated. The QPSK data modulation is eliminated by calculating  $z_k^4$  (this is essentially an M-law operation [19]) since, in the absence of noise,  $z_k^4 = -1$ . These complex amplitudes are summed, and the argument of this sum is taken as the phase estimate for the entire block (with a factor of  $\frac{1}{4}$  to account for the  $(\cdot)^4$  operation on  $Z_k$ ). The carrier phase estimate,  $\varphi_{est_{PU1}} \in \left(-\frac{\pi}{4}, \frac{\pi}{4}\right)$ , is given by [16]:

$$\varphi_{est_{PU1}} = \frac{1}{4} \arg \left\{ - \sum_{w=1}^{N_b} z_w^4 \right\} \quad (3-1)$$



The phase threshold operator  $T$  extracts the  $i^{\text{th}}$  symbol quadrant:  $T_i = \left\lfloor \frac{\arg\{z_i\} - \varphi_{estPU1}}{\frac{\pi}{2}} \right\rfloor$ ,

where the  $\lfloor X \rfloor$  operator eliminates the fractional part of  $X$ . In order to resolve the phase ambiguity arising from the  $\frac{1}{4}$  factor in Eq. (3-1), the data is differentially precoded. By employing this coding, error propagation due to cycle slips (arising from this ambiguity) is avoided. The detection process is still synchronous coherent detection, not differential detection. The operator  $C$  in Figure 3-2 decodes the data such that  $d_i = (T_i - T_{i-1})_{mod4}$ ;  $\forall i = 1..N_b - 1$ . To decode the last symbol in  $PU_1$ , the first symbol from  $PU_2$  and its phase estimate (i.e.  $T_{1PU2}$ ,  $\varphi_{estPU2}$  when decoding  $d_{NbPU1}$ ) are used:

$$d_{Nb} = \left( T_{1PU2} - T_{NbPU1} + F(\varphi_{estPU2} - \varphi_{estPU1}) \right)_{mod4} \text{ where } F(x) = \begin{cases} 1 & x > \frac{\pi}{4} \\ -1 & x < -\frac{\pi}{4} \\ 0 & \text{else} \end{cases}$$

The BER of a QPSK signal with noisy phase reference is given by [57]:

$$P_e = \int_{-\infty}^{\infty} \text{erfc} \left( \sqrt{\gamma_b} (\cos(\varepsilon) - \sin(\varepsilon)) \right) P_{\Delta\varphi}(\varepsilon) d\varepsilon \quad (3-2)$$

where  $\gamma_b = \frac{E_b}{N_0}$  is the SNR per bit,  $P_{\Delta\varphi}(\varepsilon)$  is the probability density function (pdf) of the RV  $\Delta\varphi$  which is the phase estimation error. A factor of 2 in Eq. (3-2), compared to [58], originates from differential encoding where any error in symbol decoding manifests itself twice through the differential decoding equation  $d_i = (T_i - T_{i-1})_{mod4}$ . The phase estimation error is defined using Eq. (3-3):

$$\Delta\varphi_k = \varphi_k - \frac{1}{4} \arg \left\{ - \sum_{w=1}^{N_b} z_w^4 \right\} \quad (3-3)$$

It is therefore necessary to obtain the distribution of  $\Delta\varphi$  in order to evaluate  $P_e$  in Eq. (3-2).

### 3.2.1. Distribution of the Phase Error $\Delta\varphi$

To see how  $\Delta\varphi$  is distributed, start by considering the  $(\cdot)^4$  operation:

$$z_w^4 = \left( e^{j(\varphi_{dk} + \varphi_k)} + n_k \right)^4 = -e^{j4\varphi_k} + 4\rho_w + o(n_w^3) \quad (3-4)$$

where  $\rho_w = n_w e^{j3(\varphi_{dk} + \varphi_k)} \cdot (1 + 1.5e^{-j(\varphi_{dw} + \varphi_w)} n_w)$ . For high SNR, all terms containing the shot noise of third order and higher can be neglected because  $o(n^3) \ll n^2$ . Subsequent simulation results and analytical considerations will confirm the validity of this assumption for high SNR. Substituting Eq. (3-4) into Eq. (3-3), while making this approximation, yields:

$$\Delta\varphi_k \cong \varphi_k - \frac{1}{4} \arg \left\{ \sum_{w=1}^{N_b} [e^{j4\varphi_w} - 4\rho_w] \right\}. \quad (3-5)$$

We consider first the phase estimation error in the absence of shot noise, given by:

$$\begin{aligned} \Delta\varphi_k &\cong \varphi_k - \frac{1}{4} \arg \left\{ \sum_{w=1}^{N_b} e^{j4\varphi_w} \right\} \\ &= \varphi_k - \varphi_1 - \arg \left\{ 1 + e^{j4(\varphi_2 - \varphi_1)} + \dots + e^{j4(\varphi_{N_b} - \varphi_1)} \right\} \end{aligned} \quad (3-6)$$

Eq. (3-6) is simplified by noting that the laser phase noise is a Wiener process [10] characterized by a zero mean white Gaussian frequency noise  $\delta \sim N\left(0, \sigma_\delta^2 = 2\pi \frac{2\Delta\nu}{B_r}\right)$  where  $2\Delta\nu$  and  $B_r$  are the beat LW of the transmitter and LO laser and symbol rate, respectively. The

frequency noise is independent of data modulation and shot noise. The instantaneous phase  $\varphi_k$  may then be written as  $\varphi_k = \sum_{q=1}^k \delta_q$ , where  $\delta_q$  is the carrier frequency noise at time  $q = \frac{k}{B_r}$ .

The phase difference within a time interval of  $\frac{n}{B_r}$  is then given by:

$$\varphi_m - \varphi_{m-n} = \sum_{q=1}^m \delta_q - \sum_{q=1}^{m-n} \delta_q = \sum_{q=m-n+1}^m \delta_q \quad (3-7)$$

Hence,

$$\Delta\varphi_k \cong \varphi_k - \varphi_1 - \frac{1}{4} \arg\{B(N_b)\} \quad (3-8)$$

where  $B(N_b) = 1 + \sum_{w=2}^{N_b} \exp\{j4 \sum_{p=2}^w \delta_p\}$ .  $B(N_b)$  can be derived through an example for the case of  $N_b = 4$ :  $B(4) = 1 + e^{j4\delta_2} (1 + e^{j4\delta_3} (1 + e^{j4\delta_4}))$ . Assuming that  $|4 \sum_{p=2}^w \delta_p| \ll 1$ ,  $\forall w = 2, 4$ , one may use the fact that  $e^{jx} \cong 1 + jx$  for  $x \ll 1$  to approximate  $B(4) \cong 4 + j4(3\delta_2 + 2\delta_3 + \delta_4) \cong 4 \exp\{j(3\delta_2 + 2\delta_3 + \delta_4)\}$ . In general, the approximated expression for  $B(N_b)$  is given by:

$$B(N_b) \cong N_b e^{j4\theta(N_b)} \quad (3-9)$$

where  $\theta(N_b) \cong \frac{1}{N_b} \sum_{p=0}^{N_b-2} (p+1) \delta_{N_b-p}$ . Both approximation [on  $B(N_b)$  and  $\theta(N_b)$ ] are valid assuming  $\left| \frac{4}{N_b-1} \sum_{p=0}^{N_b-2} (p+1) \delta_{N_b-p} \right| \ll 1$ , which can be shown to be applicable within the range of SNR of interest. Hence,

$\Delta\varphi_k \cong \varphi_k - \varphi_1 - \frac{1}{4} \arg\{B(N_b)\} \cong \varphi_k - \varphi_1 - \theta(N_b)$ .  $\Delta\varphi$  is a linear combination of independent, identically-distributed (iid) Gaussian RVs, which is written conveniently in matrix notation:

$$\begin{bmatrix} \Delta\varphi_k \\ \vdots \\ \Delta\varphi_{N_b} \end{bmatrix} \cong \frac{1}{N_b} \underbrace{\begin{bmatrix} 1-N_b & 2-N_b & & -2 & -1 \\ & 1 & 2-N_b & & \\ & \vdots & 2 & \ddots & \vdots \\ & & \vdots & \ddots & -2 \\ 1 & 2 & & N_b-2 & -1 \\ & & & N_b-2 & N_b-1 \end{bmatrix}}_M \begin{bmatrix} \delta_2 \\ \vdots \\ \delta_{N_b} \end{bmatrix}.$$

The variance of  $\Delta\varphi$  is the sum of the variances of the iid RVs, so that

$$\Delta\varphi \sim N\left(0, \frac{\sigma_\delta^2}{N_b} \sum_{p=1}^{N_b} \sum_{q=1}^{N_b-1} M_{p,q}^2 = \frac{N_b^2-1}{6 \cdot N_b} \sigma_\delta^2\right).$$

We proceed to incorporate the shot noise contribution to the distribution of  $\Delta\varphi$ . Eq. (3-5) can

be re-written as:  $\Delta\varphi_k \cong \varphi_k - \varphi_1 - \frac{1}{4} \arg\{B(N_b) + 4e^{-j4\varphi_1} \sum_{w=1}^{N_b} \rho_w\} \cong \sum_{q=2}^{N_b} M_{k,q} \delta_q - \frac{1}{4} \arg\left\{1 + \frac{4}{N_b} \sum_{w=1}^{N_b} \rho_w\right\}.$

Noting that the phase of a complex Gaussian white noise is uniformly distributed as  $\arg\{\rho\} \sim U(0, 2\pi)$ , any other arbitrarily distributed angle can be lumped into the phase of the shot noise without affecting its statistical attributes. Assuming  $\left|\frac{4}{N_b} \sum_{q=1}^{N_b} \rho_w\right| \ll 1$  and noting that  $\arg\{1 + |x|e^{j \cdot \arg\{x\}}\} \cong \text{Im}\{x\}$  for  $|x| \ll 1$ , this relation is written as:

$$\Delta\varphi_k \cong \sum_{q=2}^{N_b} M_{k,q} \delta_q - \frac{1}{N_b} \sum_{q=1}^{N_b} \text{Im}\{\rho_w\} \quad (3-10)$$

As the shot noise and phase noise are independent, the shot noise contribution to the variance of  $\Delta\varphi$  is additive. To determine this contribution, the distribution of  $\rho_w$  is to be established. Let  $\rho = n(1 + 1.5n)e^{j\eta}$  where  $\eta \in (0, 2\pi)$  represents an angle with an arbitrary pdf, independent of the angle of  $n$  ( $\rho_w$  is a random sample of  $\rho$ ).  $E\{n\} = E\{n_x + jn_y\} = 0$  and  $E\{n_x n_y\} = 0$ , from independence of shot noise quadratures. Hence,  $E\{ne^{j\eta}(1 + 1.5n)\} =$

$E\{e^{jn}\}E\{n(1 + 1.5n)\} = E\{e^{jn}\}E\{n^2\} = 1.5E\{e^{jn}\}E\{n_x^2 - n_y^2 + 2jn_xn_y\} = 0$ , since  $E\{n_x^2\} = E\{n_y^2\}$ . Also,  $var\{ne^{jn}(1 + 1.5n)\} = 2E\{|n^3|\}E\{\cos(\arg\{n\})\} + E\{|n|^2\} + 1.5^2E\{|n|^4\}$ .  $|n|^2$  is central-chi-square distributed with two degrees of freedom.  $\arg\{n\}$  is uniformly distributed:  $E\{\cos(\arg\{n\})\} = 0$ . From all the above,  $var\{\rho\} = E\{|n|^2\} + 1.5^2E\{|n|^4\} = \sigma_n^2(1 + 4.5\sigma_n^2)$ . Noting that  $Im\{\rho\}$  is one of the quadratures of  $\rho$ , its variance is half of that of  $\rho$ . Hence,  $var\{Im\{\rho\}\} = \frac{var\{\rho\}}{2} = \sigma_n^2 \frac{(1+4.5\sigma_n^2)}{2}$ .

Even though the term  $Im\{\rho\}$  contains a second order shot noise term, which becomes non-Gaussian distributed, the central limit theorem may be applied to obtain an approximation of the distribution of  $\Delta\varphi$  as a Gaussian [8]:

$$\Delta\varphi \sim N\left(0, \frac{1}{2N_b} \left( \frac{N_b^2 - 1}{3} \sigma_\delta^2 + \frac{(1 + 4.5\sigma_n^2)}{2} \sigma_n^2 \right)\right) \quad (3-11)$$

For a QPSK signal in the complex baseband representation with normalized symbol power, the complex noise variance is given in terms of SNR per bit ( $\gamma_b$ ) by  $\sigma_n^2 = \frac{1}{2\gamma_b}$ . Subsequent plots use  $\gamma_b$ , where substitution into Eq. (3-11) is made.

Special care should be taken when invoking the central limit theorem, since at high SNR levels the block size  $N_b$ , which determines the number of summands, is reduced. Presence of heavy tails might render the central limit theorem approximation invalid beyond first order. However, as the SNR increases, even though  $N_b$  becomes smaller, the significance of the 2<sup>nd</sup> order shot noise is diminished and the distribution of  $\Delta\varphi$  approaches Gaussian anyway. To verify the validity of this approach, a series of  $5.5 \times 10^{11}$  samples following the distribution of RV  $\Delta\varphi$  as defined in Eq. (3-11) was generated using several computers. The beat  $LW$ ,  $SNR$ , and

block size  $N_b$  used were  $2\text{MHz}$ ,  $13.5\text{dB}$ , and  $8$ , respectively. The pdf of the obtained series (generated pdf) was compared to a Gaussian pdf defined by Eq. (3-11), using the same parameters. Figure 3-3 presents the two pdfs and the associated BERs as these are accumulated under the integral in Eq. (3-2) as a function of the integration variable. As seen in Figure 3-3(top), the tails of the generated pdf are somewhat wider compared to the Gaussian pdf. However, by observing the respective BER curves, it is seen that this tails' widening does not significantly affect the final BER; i.e. the difference in BER in both cases is negligible (approximately 5%). The series of generated samples must be long enough to allow for enough events at the tails. It is observed in Figure 3-3(bottom) that the series used is indeed long enough since the BER curve for the generated pdf case levels off at roughly  $\Delta\varphi = 0.325$  where the generated pdf still has enough samples to validate this test. Similar results were obtained for a  $600\text{KHz}$  beat LW, SNR of  $13\text{dB}$  and  $N_b = 15$  (parameters which also achieve an approximate BER of  $10^{-9}$ ). When lower SNR values are considered, the second order noise becomes more significant. However, a higher shot noise level requires tighter filtering, thus  $N_b$  is increased. This in turn improves the accuracy of the Gaussian approximation since the number of summed terms is now increased. The above explanation does not imply that the actual phase estimation error variance is better approximated at a lower SNR, but simply justifies the use of a Gaussian approximation of the phase estimation error pdf at the SNR range under consideration.

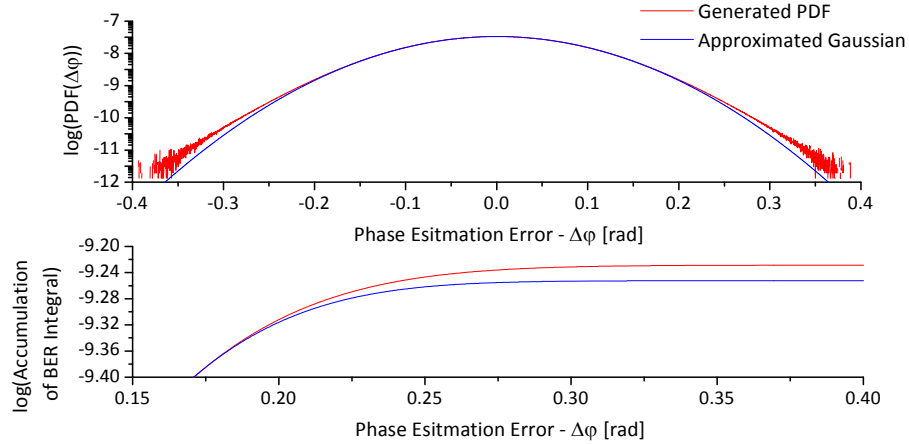


Figure 3-3: (top) Generated and approximated pdfs of  $\Delta\phi$ , (bottom) accumulation of BER integral for the two pdfs

It can be seen from Eq. (3-11) that the contribution of the phase noise to the variance of  $\Delta\phi$  increases with increasing  $N_b$ , while the impact of shot noise is reduced. The field summation within this scheme is viewed as a shot noise filtering operation. As  $N_b$  increases, the shot noise is reduced, yet this is done at the expense of slower following of the phase noise. Using Eq. (3-11), it is possible to find the optimal  $N_b$  which gives minimal standard deviation (std) of the phase estimate error and hence, smallest BER, considering Eq. (3-2):

$$N_{b_{opt}} = \text{round} \left( \sqrt{3 \frac{(1 + 4.5\sigma_n^2)\sigma_n^2}{\sigma_\delta^2} - 1} \right) \quad (3-12)$$

$\log(\text{std}(\Delta\phi))$  is shown in Figure 3-4, as a function of SNR and block size for two beat LWs of 600KHz external-cavity distributed feedback laser (DFB) and 2MHz (DFB). The symbol rate was 10GBaud. Superimposed on these plots is the optimal  $N_b$  at each SNR. The  $\log$  function was used to obtain better contrast on the figure. As shown in Figure 3-4, when the SNR is increased,  $N_b$  is reduced as a wider filter becomes sufficient.

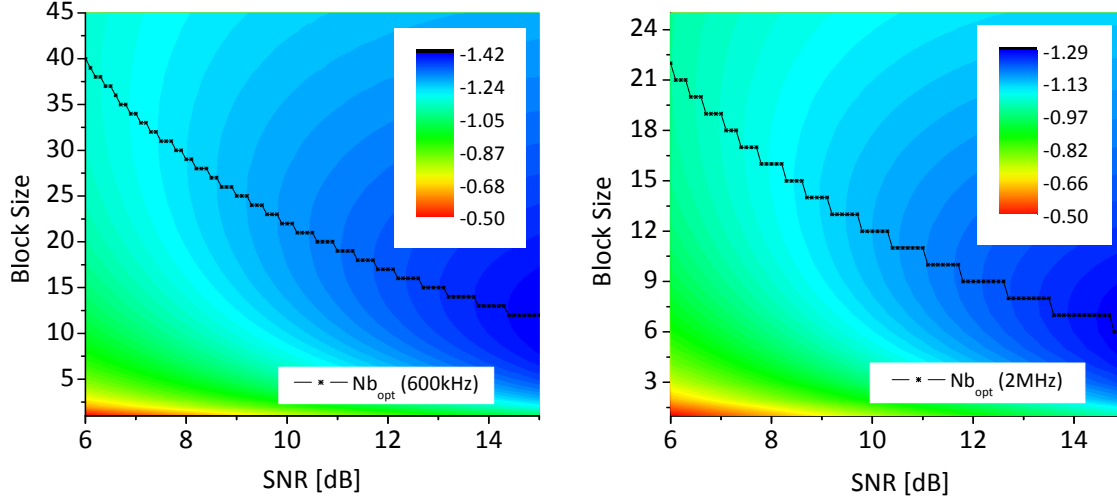


Figure 3-4:  $\log(\text{std}(\Delta\phi))$  vs. SNR and block size with optimal  $N_b$  superimposed. Left: Beat LW of 600kHz, Right: 2MHz

### 3.2.2. Comparison with Monte-Carlo Simulation

MC simulations have been performed to verify the validity of the obtained results. A comparison between the MC simulation and approximate analytical expression for  $\text{var}\{\Delta\phi\}$  is presented in Figure 3-5. The MC simulation and analytical approximation show excellent agreement, supporting the approximations made in order to reach at the analytical expression given in Eq. (3-11). As expected, the analytical expression is more accurate for smaller LWs, as seen in Figure 3-5.

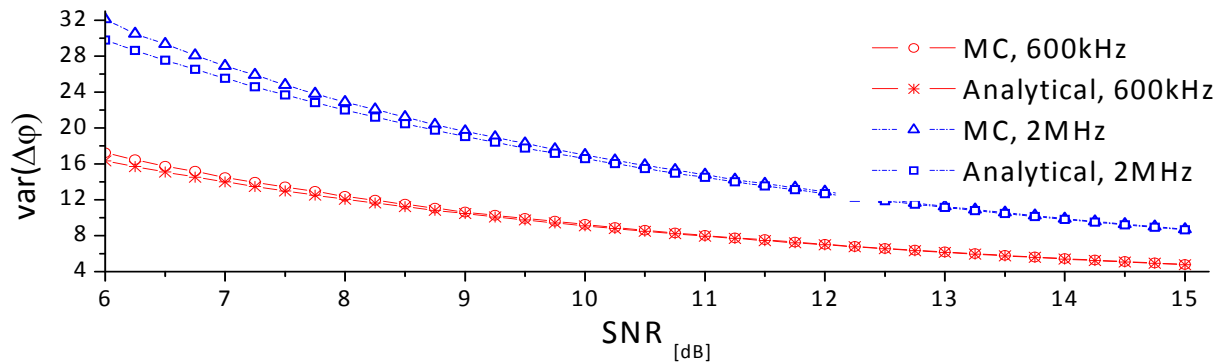


Figure 3-5: Comparison of  $\text{var}(\Delta\phi)$  from MC simulation and analytical expression

The BER curves obtained from MC simulations were also compared to the approximate BER calculated using Eq. (3-2) with  $\Delta\phi$  distributed as in Eq. (3-11). The optimal block size for



each SNR and LW considered [given in Eq. (3-12)] was used. The BER curves are presented in Figure 3-6. The MC simulations were performed using a series of  $10^6$  samples. Results of simulations with at least 100 errors are included in the BER comparison. Excellent agreement can be observed between the two cases. The limit curve shown in Figure 3-6 is the numerical evaluation of Eq. (3-2) taking  $P_{\Delta\varphi} = \delta(\varepsilon)$ . This curve corresponds to perfect following of the carrier phase. The differential-QPSK (DQPSK) limit is obtained using a differential interferometer [59]. This would serve as an upper bound on the coherent detection receiver performance. If a coherent detection receiver can't out-perform a differential interferometer (DI) receiver, it is clearly preferred to use a DI receiver, for its simplicity. Since the approximations used in the analytical derivation become more accurate with higher SNR, it is expected that the analytical approximation for BER and its MC simulation will have even better agreement at high SNR values.

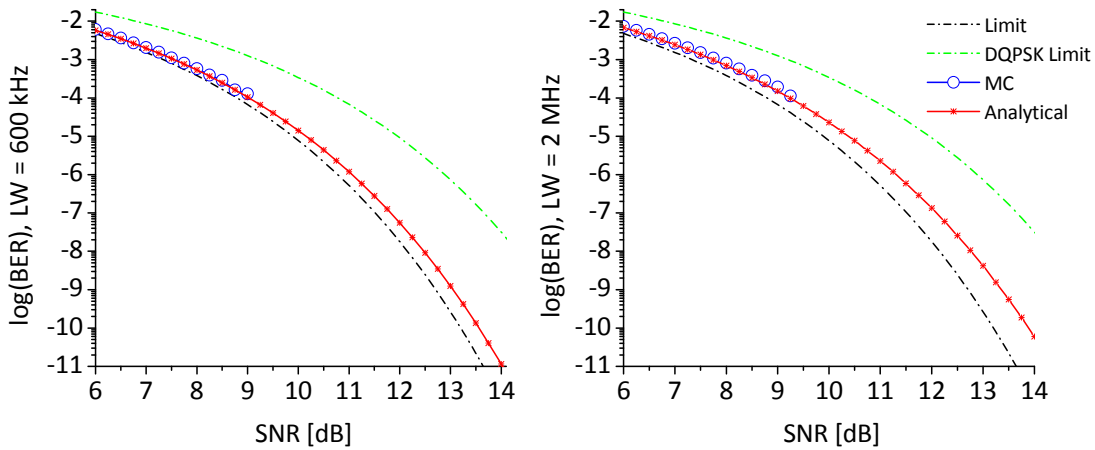


Figure 3-6: Monte Carlo simulation and analytical BER. Beat LW of (Left)600kHz, (Right)2MHz.

### 3.3. Cycle Slips in Feed-Forward Carrier Recovery Schemes

Similar to feedback type carrier synchronization schemes, feed-forward carrier phase estimation schemes manifest a phenomenon known as cycle slipping. A cycle slip occurs when

(either phase or shot) noises are large enough so that the phase estimator loses track of the actual phase and stabilizes around a different working point. This phenomenon is also known as equivocation and has been considered in [60]. In feed-forward phase estimation schemes, the occurrence of cycle-slips is due to the post-processing required for phase unwrapping [61], as described in the following.

In general, two methods can be considered for phase estimation: the block window accumulator (BWA) which divide incoming samples into blocks of size  $N_b$ , the phase estimation is common to all samples in the block, as analyzed earlier. The second approach is a gliding window accumulator (GWA), where phase estimation is done on a sample-by-sample basis by averaging several samples in the past and future. Since the information for an M-PSK modulated signal is embedded in the phase, an M-LAW operation is used to remove the information from the signal. For the BWA, the *wrapped phase estimate* is given by:

$$\hat{\phi}_k = \frac{1}{M} \arg \left\{ \sum_{q=0}^{N_b-1} z_{\left\lfloor \frac{k-1}{N_b} \right\rfloor N_b + q}^M \right\} \in \left[ 0, \frac{2\pi}{M} \right) \quad (3-13)$$

where  $z_q$  is the  $q^{th}$  information-bearing symbol (phase estimation is employed after channel equalization). For the GWA scheme the wrapped phase estimate is  $\hat{\phi}_k = \frac{1}{M} \arg \left\{ \sum_{q=-GD}^{GD} (Z_{k+q})^M \right\}$  where  $GD = \frac{N_b-1}{2}$  is the group delay for the additive-noise reducing filter. The GWA can be shown to lead to more accurate phase estimation, especially if a frequency offset exists between the signal carrier and LO. It is however somewhat more resource-consuming since the BWA calculates a common phase for  $N_b$  symbols, rather than symbol-by-symbol estimation.

In order to obtain a proper phase estimate covering the entire range  $[0, 2\pi)$ , the angle  $\hat{\varphi}_k$  must be unwrapped. This is achieved through post processing, as follows. The unwrapped phase estimate  $\tilde{\varphi}_k$  is written as  $\tilde{\varphi}_k = \hat{\varphi}_k + N_k \frac{2\pi}{M}$  where  $N_k$  is an integer to be chosen using the criterion:  $|\tilde{\varphi}_k - \tilde{\varphi}_{k-1}| < \frac{\pi}{M}$ . This is effectively a maximum-likelihood type estimation since the constraint here is that the phase absolute difference between two successive phase estimates is less than  $\frac{\pi}{M}$ . From the above discussion, the following post-processing constraint is derived:  $\tilde{\varphi}_k - \tilde{\varphi}_{k-1} = \hat{\varphi}_k + N_k \frac{2\pi}{M} - \tilde{\varphi}_{k-1}$ . The right-hand side of this equation can be written as a saw-tooth function with periodicity  $\frac{2\pi}{M}$ . The post-processing block diagram is shown in Figure 3-7.

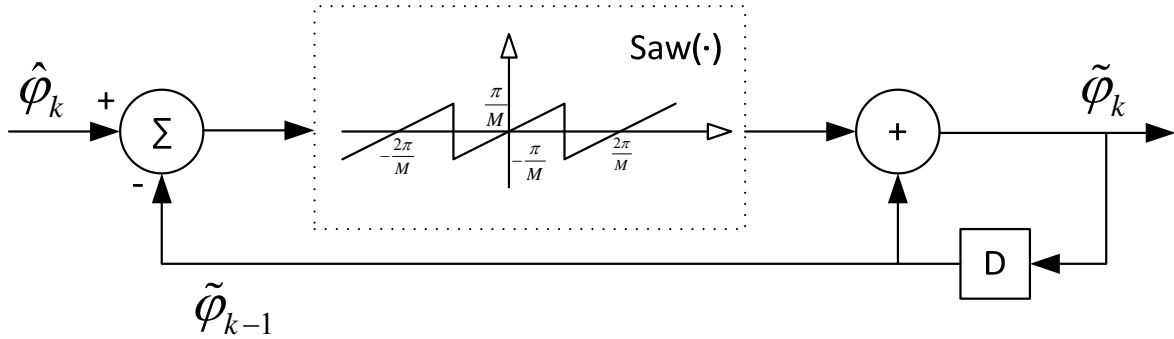


Figure 3-7: Phase estimation post processing

The PP procedure involves feedback which is not feasible in high-speed parallel DSP environment. This procedure may be re-cast as an all feed-forward as follows.  $\tilde{\varphi}_k - \tilde{\varphi}_{k-1} = \hat{\varphi}_k + N_k \frac{2\pi}{M} - \hat{\varphi}_{k-1} + N_{k-1} \frac{2\pi}{M} = \hat{\varphi}_k - \hat{\varphi}_{k-1} + \Delta N_k \frac{2\pi}{M}$  where  $\Delta N_k$  is again chosen so  $|\hat{\varphi}_k - \hat{\varphi}_{k-1} + \Delta N_k \frac{2\pi}{M}| < \frac{\pi}{M}$ . In order to unwrap the phase  $\Delta N_k$ , must be determined at the symbol rate [26]. To remedy this, a differential encoding scheme is used so that only a phase jump is considered, not the absolute phase. This also aids in case of a cycle slip where non-differential

encoding leads to catastrophic BER between synchronization frames. The all feed-forward scheme is equivalent to the one presented in [61], with the post-processing re-cast here so feedback is not a concern if a proper level of parallelism is available. Note that the differential encoding is at the expense of receiver sensitivity.

The following cycle-slip analysis concentrates on the BWA scheme. To illustrate this phenomenon, a cycle-slip event is presented in Figure 3-8, for SNR per bit ( $\gamma_b$ ) of 6dB and block size  $N_b = 9$  using a BWA:

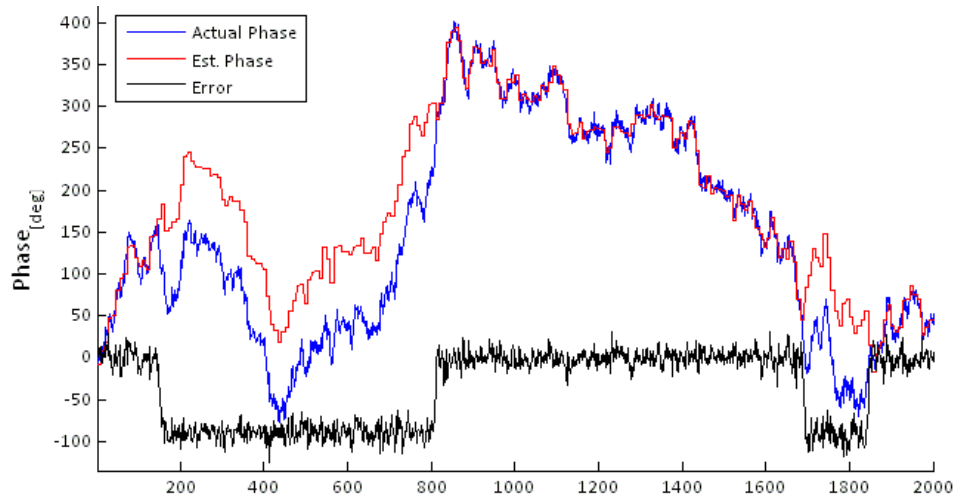


Figure 3-8: Example of cycle slip for  $LW = 20\text{MHz}$ ,  $\gamma_b = 6\text{dB}$ ,  $N_b = 9$

A cycle slip event causes the phase estimation to jump by a multiple of  $\pm \frac{2\pi}{M}$ . As opposed to an error induced by phase noise and shot noise which doesn't involve a cycle slip, here the influence of the error is limited to a single symbol, rather than two. A cycle slip occurs when  $\Delta N_i$  is chosen erroneously due to either  $\hat{\varphi}_i$  or  $\hat{\varphi}_{i-1}$  being sufficiently corrupted by noise. Since  $\hat{\varphi}$  is corrupted by both shot noise and phase noise, both have to be taken into account when analyzing the phase estimation statistics. In the RF domain, this problem has been addressed (e.g., [62, 63]) with a limited degree of success due to the highly nonlinear nature of the cycle

slip phenomenon. The cycle slip issue in the optical domain is different in that the optical oscillator linewidth plays a big role when cycle slip is concerned. Oscillators in the RF domain exhibit exceedingly small linewidths and therefore the problem is limited to the effect of shot noise on cycle slips.

In order to determine the cycle slip statistics, the first task is to observe when exactly a cycle slip occurs. This is required in order to define a pdf which is to be used to calculate the cycle slip probability. Moreover, the conditions on this pdf (i.e. integration limits) should also be established to complete this task. Determining when exactly a cycle slip occurred is not trivial due to the nonlinear nature of this phenomenon and the fact that there are multiplicative (phase noise) and additive (shot noise) random processes involved. It is practically impossible to isolate one from the other, except for the most trivial case (i.e. when the block size  $N_b = 1$ ).

Indeed  $N_b = 1$  serves as the starting point of this study. Using MC simulations (for QPSK,  $M = 4$ ), it is possible to determine a combination of values ( $\text{SNR}/\text{LW}/N_b$ ) which corresponds to operation around the forward error-correction (FEC) limit (in this work this corresponds to a BER of  $10^{-3}$ ). The LW may be arbitrarily chosen as the independent variable; SNR and  $N_b$  were scanned and optimized to achieve the FEC limit. In Figure 3-9, the SNR and  $N_b$  are plotted as a function of LW corresponding to the FEC-limited BER.

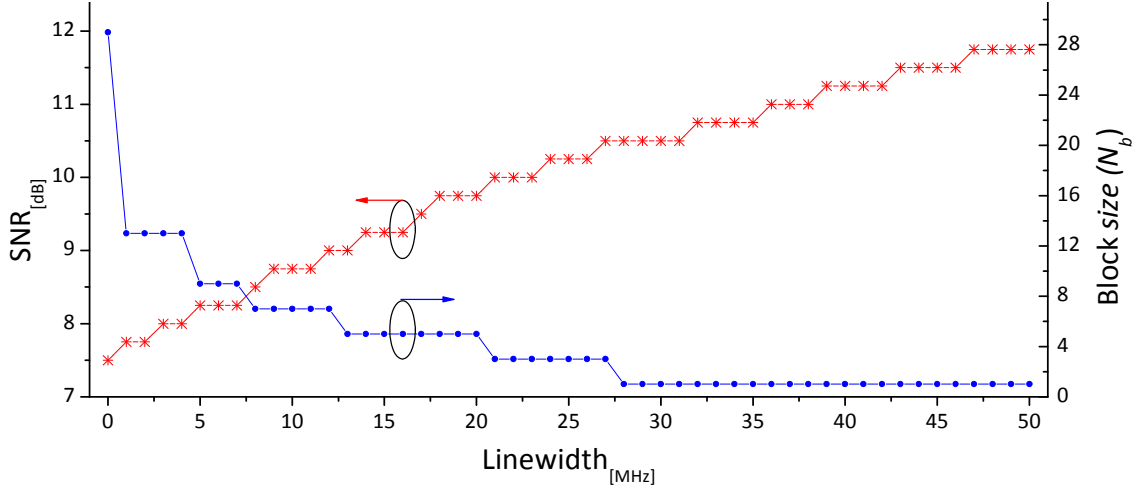


Figure 3-9: LW/SNR/ $N_b$  values for FEC limit BER

As expected, for higher LW values, the SNR must be kept high to maintain the same performance. Moreover,  $N_b$  is also reduced. The case where  $N_b = 1$  bears special interest since, in the absence of shot noise, the phase can be followed perfectly so long that the actual phase deviation doesn't exceed  $45^\circ$  between consecutive samples. Such a phase excursion is very unlikely event when reasonable laser LWs are considered and high signaling rate is used. It is reasonable to suspect that a cycle slip occurs when the contribution from shot noise is considerable. This leads to the following argument regarding cycle slip events: a cycle slip occurs when the phase estimation in the presence of shot noise deviates by more than  $\pi$  from what it would be in the absence of shot noise. The reason why  $\pi$  determines the cutoff value for a cycle slip is that the combined values of the wrapped phase estimation and its correction  $\Delta N_i$  have a maximum (absolute) value of  $\pi$ .

Neglecting shot noise, define  $X_k = e^{j4\varphi_{PNk}}$  as the output from the filter where  $\varphi_{PN}$  is the phase noise term (no filtering effectively takes place here since  $N_b = 1$ ). The factor of 4 comes from the nonlinear operation used to eliminate the data. Let  $aX_k = \arg\{X_k\}$ . Since a cycle slip is a phase estimation discontinuity, we are interested in the phase estimates

differential:  $daX_k = \arg\left\{\frac{X_k}{X_{k-1}}\right\} = \arg\{e^{j4(\varphi_{PNk}-\varphi_{PNk})}\} = \arg\{e^{j4\delta_k}\}$ . Note that in general  $\arg\{e^{j4\delta_k}\} \neq 4\delta_k$  unless  $|\delta_k| < 45^\circ$  as the function  $\arg\{\cdot\}$  is defined on the interval  $[-\pi, \pi)$ .

The BER floor ( $SNR \rightarrow \infty$ ) can be readily obtained as a function of  $\Delta\nu/B_r$  product since, as mentioned earlier, a cycle slip must occur when the phase estimation is more than  $45^\circ$  off from the actual phase ( $B_r$  is the symbol rate). The theoretical BER floor is obtained by noting that each cycle slip contributes a single error to the BER. Since  $\delta \sim N(0, \sigma_{PN}^2 = 2\pi\Delta\nu/B_r)$ ,

$$BER_{floor} = \frac{1}{2}P_r\left(|\delta| > \frac{\pi}{4}\right) = \frac{1}{2}erfc\left\{\frac{\frac{\pi}{4}}{\sqrt{2}\cdot\sigma_{PN}}\right\} = \frac{1}{2}erfc\left\{\frac{1}{8}\sqrt{\frac{\pi}{\Delta\nu/B_r}}\right\}. \quad (3-14)$$

Verification of this argument is done via direct counting of single errors in the known output data stream (single error probability) and comparison of the actual phase vs. phase estimation by looking for discrete jumps (cycle slip probability). Simulation and theoretical results match closely as seen in Figure 3-10. The confidence level marks a BER level guaranteeing more than 100 errors within the MC simulation. BER levels above this line are statistically trustworthy.

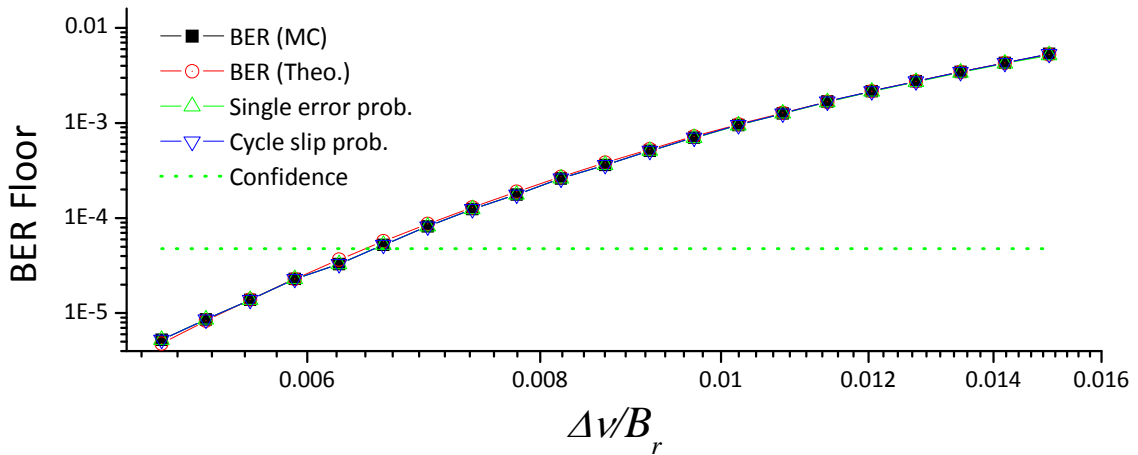


Figure 3-10: Theoretical and simulation results for BER floor vs.  $T_s\Delta\nu$

In order to incorporate the effect of additive (e.g. shot) noise, we define the shot noise corrupt phase estimation as follows,  $Z_k = (e^{j\varphi_{PNk}} + n_k)^4 = e^{j4\varphi_{PNk}}(1 + n_k)^4$  where  $n$  is the additive white Gaussian noise. Note that the uniform distribution of the complex Gaussian noise allows extracting the term  $e^{j4\varphi_{PNk}}$  in the last expression, leaving the noise statistics unchanged. Similar to the definition for  $aX_k$ , the angle of  $Z_k$  is defined as  $aZ_k = \arg \{Z_k\}$ , and the differential angle is

$$daZ_k = \arg \left\{ \frac{Z_k}{Z_{k-1}} \right\} = 4\delta_k + \arg \left\{ \frac{w_k}{w_{k-1}} \right\} \quad (3-15)$$

where  $w_k = (1 + n_k)^4$ . It is clearly seen that for  $N_b = 1$ , the shot noise and phase noise terms are easily separated. In order to clarify how these two constructed variables are associated with the cycle slip phenomena, a graphic representation is beneficial. Define  $P_k = daX_k + jdaZ_k$ .  $P$  is plotted point-wise on the complex plain. Using MC simulation, it is possible to determine when a cycle slip occurred by isolating single errors from the output bit stream. Complex  $P$  is shown in Figure 3-11. Each  $P_k$  for a value of  $k$  which was determined as a cycle slip is marked with a red circle. Using the MC simulation to depict cycle slip occurrences, it is established that the constructed variables  $daX$  and  $daZ$  are highly relevant to the cycle slip study.

From Figure 3-11 the regions of integration of pdfs of  $daX$  and  $daZ$  required for the calculation of the cycle-slip probability are evident. Next, the pdfs of  $daX$  and  $daZ$  must be established.  $daX = \arg \{e^{j4\delta_k}\} = 4\delta_k$  so that its distribution is  $daX \sim N \left( 0, \sigma_{daX}^2 = 16 \cdot 2\pi \frac{2\Delta\nu}{B_r} \right)$ . Since  $daX \in [\pi, -\pi)$  the Gaussian pdf must be folded such that



$f_{daX}(x) = \sum_{k=-\infty}^{\infty} \left( \frac{1}{\sqrt{2\pi\sigma_{daX}^2}} e^{-\frac{(x+2\pi k)^2}{2\sigma_{daX}^2}} \right)$ . As the variance  $\sigma_{daX}^2$  decreases, summation can be

done on less terms, where usually  $k = 0$  is sufficient for practical linewidths.

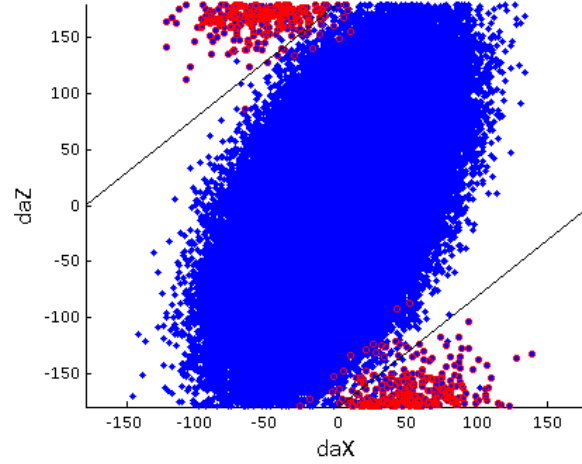


Figure 3-11: Complex plane graphical representation of  $P$ ,  $LW = 30\text{MHz}$ ,  $SNR = 10.5\text{dB}$ ,  $N_b = 1$

From Eq. (3-15) it is seen that  $daZ = daX + daQ$  where  $daQ = \arg\left\{\frac{w_k}{w_{k-1}}\right\}$ . Since  $daQ$  is a summation of two iid RVs, its pdf is simply the convolution of the pdf of  $\arg\{w_k\} = \arg\{(1 + n_k)^4\}$  with itself. The derivation begins with  $v(x, y) = 1 + n = 1 + x + jy$ . The pdf of  $v$  in Cartesian coordinates is  $f_v(x, y) = \frac{\sqrt{x^2+y^2}}{\pi\sigma_{SN}^2} e^{-\frac{(x-1)^2+y^2}{\sigma_{SN}^2}}$  where  $\sigma_{SN}^2$  is the variance of the

complex additive noise [64]. After transformation to polar coordinates

$f_v(r, \eta) = \frac{r}{\pi\sigma_{SN}^2} e^{-\frac{r^2-2rcos(\eta)+1}{\sigma_{SN}^2}}$ . The marginal angle pdf is obtained by integrating  $f_v(r, \eta)$  over  $r$ :

$f_\eta(\eta) = \frac{1}{2\pi} \left( e^{-\frac{1}{\sigma_{SN}^2}} + \sqrt{\frac{\pi}{\sigma_{SN}^2}} \cos(\eta) e^{-\frac{\sin^2(\eta)}{\sigma_{SN}^2}} \text{erfc}\left\{-\frac{\cos(\eta)}{\sigma_{SN}}\right\} \right)$ . The 4-law operation (considering

QPSK here) must be taken into account before the  $\arg\{\cdot\}$  function is considered. This operation also folds the angle at the boundary. Taking all these considerations into account the results in

the distribution for  $aQ$ :  $f_{aQ=\arg\{(a+n)^4\}}(\mu) = \frac{1}{4} \sum_{k=-2}^1 f_{\eta} \left( \frac{\eta}{4} + \frac{\pi}{2} k \right)$ ,  $\eta \in [-\pi, \pi)$ . Ultimately, the pdf for  $daQ$  is obtained by convolution:

$$f_{daQ}(q) = \int_{-\pi}^{\pi} f_{aQ}(m) f_{aQ}(q - m) dm \quad (3-16)$$

Given the integration regions seen in Figure 3-11 and the pdfs for  $daX$  and  $daQ$ , the probability of a cycle-slip,  $P_j$ , with ( $N_b = 1$ ) is calculated using the following integration:

$$P_j = 2 \int_0^{\pi} f_{daX}(x) \left( \int_{\pi-x}^{\pi} f_{daQ}(q) dq \right) dx \quad (3-17)$$

The analytical cycle-slip probability for a linewidth of  $40MHz$  is plotted in Figure 3-12. To verify the accuracy of the obtained expression, MC simulations were conducted and the probability of cycle-slips was obtained for  $LW = 40MHz$ , as a function of SNR. The optimal block size is  $N_b = 1$  for all the SNR values considered here. It is observed that for high values of SNR, the theoretical cycle-slip probability is in excellent agreement with the MC simulation. At lower SNR values, the analytical and numerical cycle-slip probabilities somewhat diverge. This is due to the fact that the integration limits in Eq. (3-17) do not take into account cycle-slips which stem from a large additive noise contribution and hence, the integration regions in Eq. (3-17) are not as accurate as for the high SNR case.

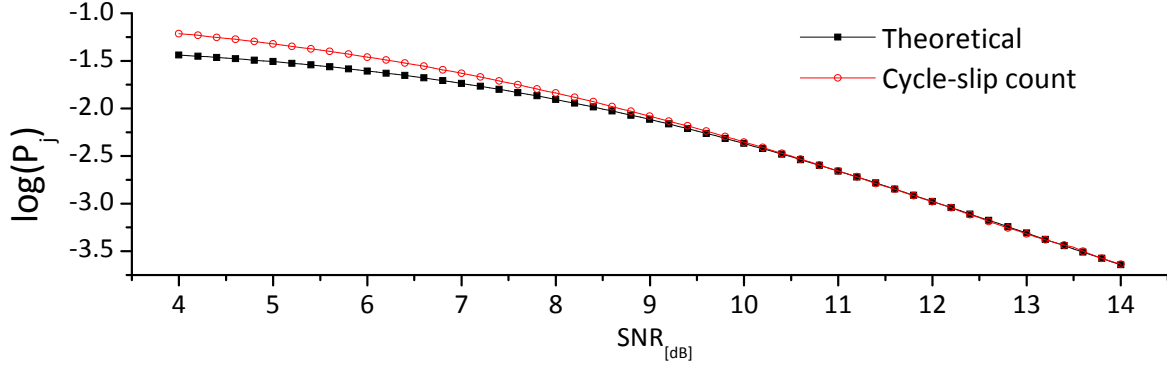


Figure 3-12 : Cycle slip probability

The case where  $N_b > 1$  is entirely non-trivial since the shot noise and phase noise terms cannot be separated as easily as when  $N_b = 1$ . This is easily demonstrated by taking a seemingly simple example for  $N_b = 2$ . Define  $Z_1 = (e^{j\varphi_{PN1}} + n_1)^4 + (e^{j\varphi_{PN2}} + n_2)^4 = e^{j4\varphi_{PN1}w_1} + e^{j4\varphi_{PN2}w_2}$  and  $Z_2 = e^{j4\varphi_{PN3}w_3} + e^{j4\varphi_{PN4}w_4}$ . Like previously,  $daZ = \arg\left\{\frac{Z_2}{Z_1}\right\} = \arg\left\{\frac{e^{j4\varphi_{PN3}w_3} + e^{j4\varphi_{PN4}w_4}}{e^{j4\varphi_{PN1}w_1} + e^{j4\varphi_{PN2}w_2}}\right\} = \arg\left\{\frac{e^{j4\varphi_{PN3}(w_3 + e^{j4\delta_4}w_4)}}{e^{j4\varphi_{PN1}(w_1 + e^{j4\delta_2}w_2)}}\right\} = \arg\left\{\frac{e^{j4\delta_3}(w_3 + e^{j4\delta_4}w_4)}{w_2 + e^{-j4\delta_2}w_1}\right\}$ .  $daX$  is defined similarly, with the exception that all shot noise contributions  $w_k \equiv 1$  since the shot noise is eliminated:  $daX = \arg\left\{\frac{e^{j4\delta_3}(1 + e^{j4\delta_4})}{1 + e^{-j4\delta_2}}\right\}$ . In this case the contribution from shot and phase noises can't be separated as easily as for  $N_b = 1$ . The problem here is to define the proper integration conditions to allow determining the cycle slip probability when  $daX$  and  $daZ$  are correlated in an intricate manner. This remains an open topic still.

### 3.4. Conclusions

In this chapter, an analytical approximation to the BER expression for a feed-forward, block window phase estimation algorithm was obtained. The approximation assumes working conditions (SNR and LW) relevant to modern day optical devices. It was shown that the phase estimation error is affected by both additive noise and laser LW and its distribution can be

approximated by a Gaussian, using the central limit theorem. Monte-Carlo simulations verify that the approximations taken are valid by excellent agreement of the BER curves between theory and simulation, for several linewidth values considered. A tradeoff between linewidth and additive noise (SNR) was observed, where higher linewidth values force the SNR to be lower in order to maintain equivalent performance. The derived analytical approximation allows finding an optimal block size as a tradeoff between SNR and linewidth.

The cycle slip-phenomenon in feed-forward phase tracking schemes was presented. For a block size of 1 (reached at high SNR and linewidth values), the probability of occurrence of cycle-slips was obtained. This allows incorporating the cycle-slip phenomenon into the analytical expression for the BER of a system in which such feed-forward phase-tracking algorithms are used.

## CHAPTER 4. ORTHOGONAL WAVELENGTH-DIVISION MULTIPLEXING

### 4.1. Introduction

An advantage of coherent detection often quoted is the inherent ultra-narrow optical filtering capability, because optical filtering is effectively performed in the electrical domain. A wavelength-division multiplexing (WDM) channel spacing of 1.3 times the symbol rate has been demonstrated, with a penalty of over  $10\text{dB}$  [65]. The penalty monotonically increased with decreasing channel spacing in that experiment. In principle, it is possible to have a WDM channel spacing equal to the symbol rate with no penalty [54]. Orthogonal-frequency division multiplexing (OFDM) is known to achieve this condition, but arranging for the WDM channels to be orthogonal relative to one another would require too much transmitter and receiver bandwidth. In this chapter the case is investigated theoretically and experimentally where the channel spectra are allowed to overlap, but realistic pulse shapes are used.

### 4.2. Theory

The experiment and simulations described in this chapter are for single-polarization binary phase shift keyed (BPSK) transmission format, with all WDM channels co-polarized. A higher data rate would be obtained using quadrature phase-shift keying and polarization-division multiplexing, but the impact of crosstalk should be approximately same as for single polarization BPSK.

A model of the communication system considered is described as follows. The electric field of the transmitted optical signal is given by:

$$x(t) = \sum_{k=1}^C \sum_{q=0}^{\infty} a_{k,q} g(t - qT) e^{j\omega_k t} \quad (4-1)$$

where  $C, g(t), T$  and  $\omega_k$  are the total number of optical channels, pulse shape, symbol rate and angular carrier frequency of the  $k^{\text{th}}$  channel, respectively.  $a_{k,q}$  is the  $q^{\text{th}}$  information symbol of the  $k^{\text{th}}$  channel, and for BPSK the values of the  $a_{k,q}$  are selected from  $\{-1, 1\}$ . At the coherent receiver, the transmitted signal is mixed with the local oscillator (LO). ASE-induced additive noise  $n(t)$ , expressed in baseband, is added to the signal by the communications channel, and then it is detected by the coherent receiver. The output signal from the receiver is

$$y(t) = \left( x(t) e^{-j\omega_{LO} t} + n(t) \right) \otimes h(t) \quad (4-2)$$

where  $h(t)$  is the net receiver impulse response, composed of the impulse response of the receiver front end combined with additional equalization filtering. When the coherent receiver is like that of [25] the receiver output is in digital form, and post-detection equalization is implemented by a digital filter, but it is assumed that the sampling rate is high enough that continuous time functions  $y(t)$  and  $h(t)$  can be considered.  $\omega_{LO}$  refers to the effective LO frequency, given by the actual LO frequency together with any adjustments applied in the digital domain.

In general reducing channel spacing in a WDM system is expected to lead to increased penalty due crosstalk where the spectra of adjacent channels starts to overlap. However, if the channel spacing along with the transmit and receive pulse shapes is such that adjacent channels are orthogonal to each other, this penalty can be cancelled even though the adjacent channel spectra still overlap. For OFDM the pulse shape  $g(t)$  is a perfectly square pulse (of

width  $T$ ) and  $h(t)$  is the same square pulse (the matched filter). In this case, there is no crosstalk from the adjacent channels. To illustrate this principle, Eq. (4-1) and Eq. (4-2) are written for two channels spaced by  $\frac{2\pi}{T}$  where  $\omega_{LO} = \omega_1$ :

$$\begin{aligned}
 x(t) &= \sum_{q=0}^{\infty} \left( a_{1,q} g(t - qT) + a_{2,q} g(t - qT) e^{j\frac{2\pi t}{T}} \right) \\
 y(t) &= \sum_{q=0}^{\infty} \int_0^T \left( a_{1,q} g(t - \tau - qT) + a_{2,q} g(t - \tau - qT) e^{j\frac{2\pi t}{T}} \right) dt \\
 &= \sum_{q=0}^{\infty} a_{1,q} g \otimes h(t - qT)
 \end{aligned} \tag{4-3}$$

The second channel is extinguished by convolution with the receive filter.  $g \otimes h$  is a triangular pulse shape. The data streams of the two channels must be aligned in time, otherwise any change in the information carried by  $a_2$  within the integration period would prevent the term  $a_2 e^{j\frac{2\pi t}{T}}$  from canceling. It is not usual to align the symbol periods of WDM channels; introduction of this feature might be considered in order to reach the spectral efficiency limit.

### 4.3. OFDM Simulation

Simulation of the eye diagram for the two-channel system (for  $6\text{GBaud}$  BPSK) is presented in Figure 4-1. The carrier phase of channel 2 was slowly ramped so that all phases were explored. This leads to the filled-out appearance of the channel 1 eye, but notice that the phase does not affect the perfect crosstalk cancellation at the eye center. The average inter-channel crosstalk of this OFDM case is high ( $8.3\text{dB}$ ) which can be thought of as the average

crosstalk over a whole symbol period or as the amount of overlap of the spectra of the two channels. The symbol intervals of the two channels are perfectly aligned in the simulation of Figure 4-1(left). A small misalignment would clearly result in a substantial crosstalk penalty at the symbol center.

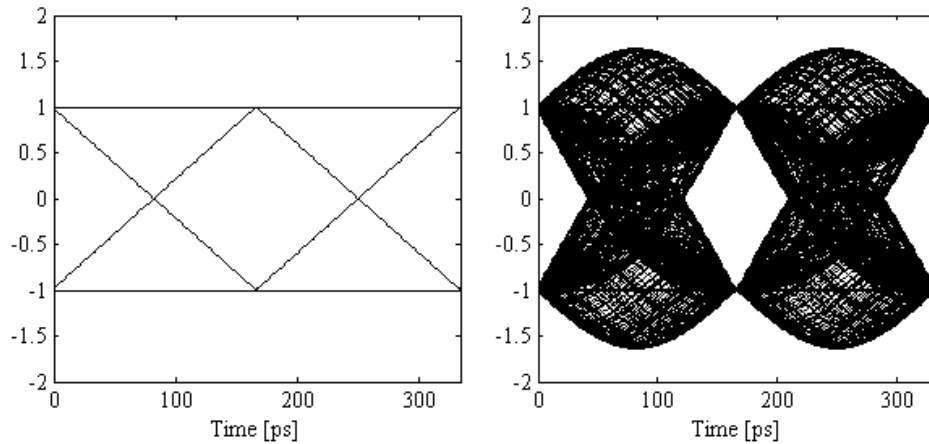


Figure 4-1: Eye diagram simulation; single channel (left) two OFDM channels (right)

The principle illustrated above is referred to as OFDM. However, the square pulse condition cannot be met for the high symbol rates used in fiber optic transmission as it would require too much transmitter and receiver bandwidth. Orthogonal WDM aims for the narrow channel spacing without the requirement of perfectly square pulse shapes. This may lead to a penalty when the channel spacing is equal to the symbol rate. A mode of OFDM that has been proposed recently for optical communications is where closely spaced digital sub-carriers are generated within each WDM channel, carrying information having very long pulse duration. This OFDM realization is efficient in mitigating inter-symbol-interference due to fiber dispersion effects [66-68]. However it is not clear that this method allows WDM channels to be spaced any more closely than with conventional WDM channels using direct detection. An additional



advantage of the orthogonal-WDM (OWDM) scheme is that it allows tight WDM channel spacing while the transmitter employs simple binary modulation.

#### 4.4. Experimental Results

To verify the viability of the suggested OWDM scheme, an experiment was performed as presented in Figure 4-2. The center channel ( $\omega_c$ ) is BPSK modulated using a Mach-Zehnder modulator driven at  $6\text{Gbaud}$  by a pattern generator (PG). Pseudo-random bit sequence of length  $2^{23} - 1$  was used. Two adjacent channels ( $\omega_R$  and  $\omega_L$ ) are also modulated and combined with the center channel. The adjacent channels have synchronized symbol times but decorrelated data content compared to the center channel. Noise is loaded by combining the three modulated channels with the output of several cascaded EDFAs with no input, inducing amplified spontaneous emission (ASE). A  $90^\circ$  hybrid and real-time oscilloscope (RTO) are used to coherently detect and sample the noise-loaded signal. The LO was set to match  $\lambda_c$ . The obtained samples were processed offline. The ASE level was set so the decision-threshold Q-factor in the absence of adjacent channels was approximately 14 dB. An adaptive equalization algorithm was employed to obtain a filter which maximizes the Q-factor in the absence of adjacent channels. This filter was used in subsequent measurements. To determine the channel crosstalk penalty, the channel spacing was scanned by varying  $\lambda_R$  and  $\lambda_L$ , the Q-factor measured for each case.  $1.5 \times 10^5$  symbols were used to determine the performance at each channel spacing.

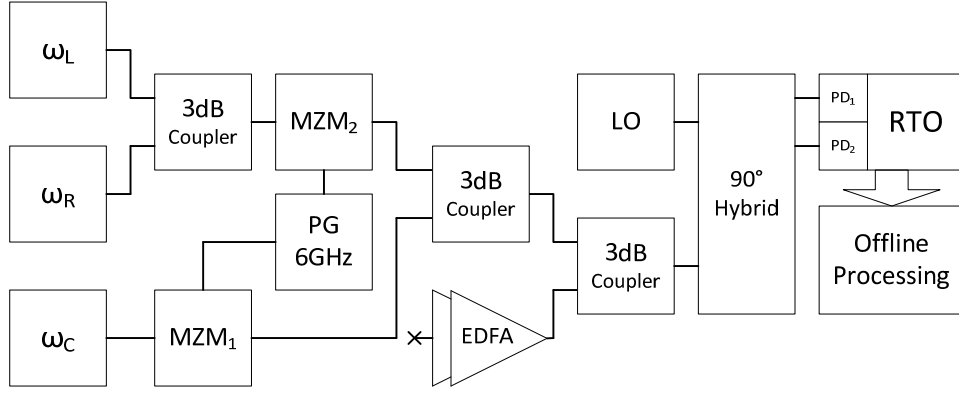


Figure 4-2: Experimental setup

The decision-threshold Q-factor for each channel spacing is shown in Figure 4-3. When the channel spacing is much tighter than the symbol rate, a large penalty is incurred. This penalty is reduced as the channel spacing increases to an optimal point (7.5GHz for OWDM, compared to 6GHz for OFDM). This shift in optimum channel spacing to a higher value than the symbol rate is due to asymmetries in the pulse shape. Increasing the channel spacing even further actually increases the penalty. From certain channel spacing, the channels are sufficiently spaced so that the spectral overlap is diminished and the Q-factor levels off.

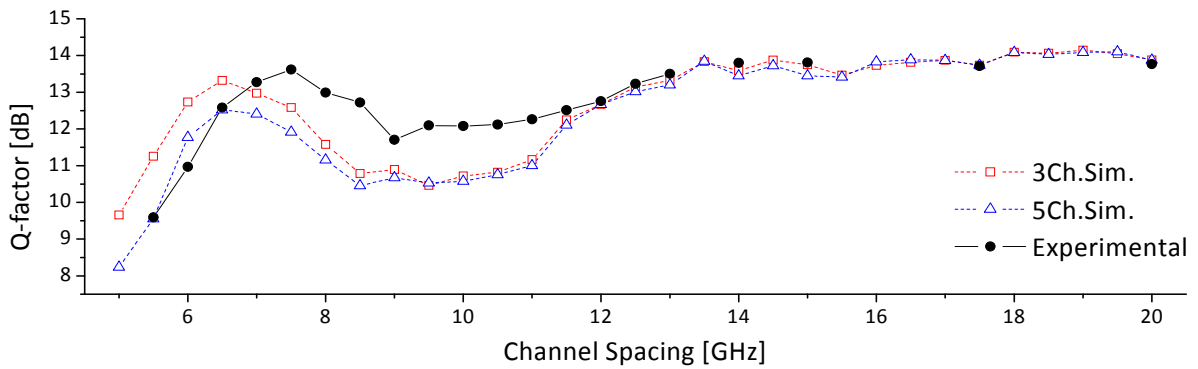


Figure 4-3: Q-factor vs. channel spacing

It is seen that the best result is obtained for a channel spacing of 7.5 GHz (penalty of 0.15dB), while at the symbol rate (6 GHz) the penalty is 2.8 dB. Also shown in Figure 4-3 are the

simulation results when 3 and 5 WDM channels are present. There is a slight penalty ( $0.8dB$ ) when 5 channels are considered which arises because the next-to-nearest neighbors have a small spectral overlap with the center channel. Simulations show slightly lower optimum channel spacing than the experiment, probably because the actual pulse shape deviates from raised cosine shape assumed for the simulations.

Simulated (top) and experimental (bottom) eye diagrams without crosstalk (single channel, left) and with 2 adjacent channels separated by  $6GHz$  (right) are presented in Figure 4-4. Crosstalk is suppressed at the center of the eye with adjacent channels. The simulation assumes a raised cosine shaped transmit pulse and receiver impulse response, with roll-off factor 0.3. The OWDM eye diagram with adjacent channels shows that the crosstalk is lower (but not zero) at the center of the symbol compared to the average over the whole symbol. The OWDM simulation indicates that the average crosstalk is  $-8.9dB$ , while the symbol center crosstalk is  $-16.0dB$ . There is a good correspondence between simulation and experiment.

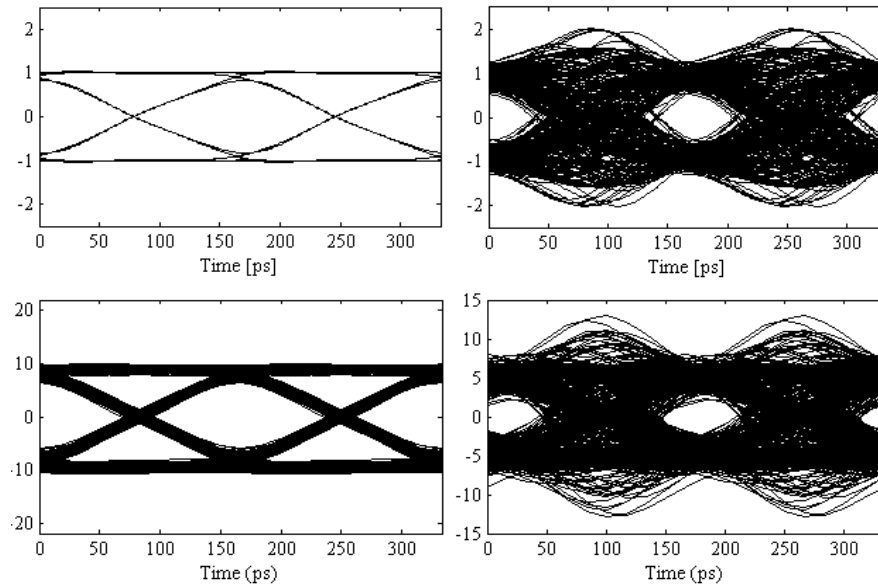


Figure 4-4: Simulation (top) and experimental (bottom) eye diagrams for single channel (left) and with adjacent channels spaced at  $6GHz$  (right)

#### 4.5. Effect of Receiver Bandwidth and Front End Filtering

The reason for choosing a  $6\text{GHz}$  symbol rate in the experiment is that it was found to be necessary to use a low symbol rate to avoid a crosstalk penalty associated with the clipping of the optical spectra of the adjacent channels. The real-time oscilloscope (RTO) front end includes an anti-aliasing filter with a steep cut-off at  $12.5\text{GHz}$ . This means that although the center channel's spectrum was detected in full, the two adjacent channels were effectively clipped. The symmetry condition that leads to crosstalk suppression at the center of the symbol requires the entire spectra of the adjacent channels to be present, even though the aim is to suppress the adjacent channels. The anti-aliasing filter was represented as a  $10^{\text{th}}$  order Butterworth filter in the simulation, and could be switched on and off. Figure 4-5 shows the eye diagrams for a simulation of three  $10\text{Gbaud}$  channels separated by  $10\text{GHz}$ , with and without the anti-aliasing filter. Suppression of the crosstalk at the symbol center compared to the average of the whole symbol is  $6.0\text{dB}$  in the absence of the anti-aliasing filter, and only  $1.9\text{dB}$  with the filter present. Introducing the anti-aliasing filter adds a Q-factor penalty of  $2.1\text{dB}$ .

The requirement that the receiver bandwidth be wide enough to see three adjacent WDM channels adds expense to the receiver. In our experiment a  $40 \frac{\text{GSamples}}{\text{s}}$  digitizer with  $12.5\text{GHz}$  bandwidth was used to detect a  $6\text{Gbaud}$  signal. In the future one might have several coherent receivers observing neighboring blocks of channels and sharing information between them, so that the electric field envelope of one channel is obtained from digitized samples from two coherent receivers with their respective LOs tuned so that spectral stitching may be implemented. In that scenario the requirement for excess sample rate is alleviated, when averaged over all the WDM channels.

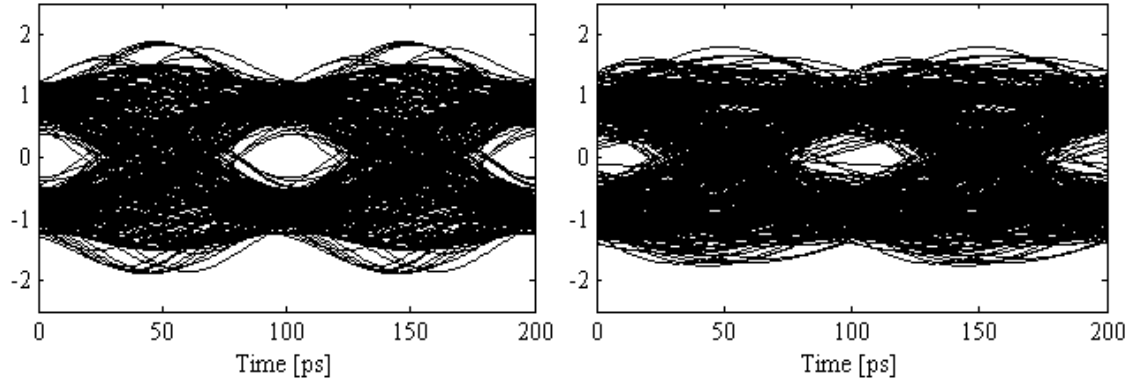


Figure 4-5: Simulation of 10Gbaud center channel eye, without (left) and with (right) an anti-aliasing filter

#### 4.6. Conclusion

The OWDM channel spacing reported here (i.e. 6GHz with 6Gbaud channels) represents the highest spectral efficiency and lowest penalty obtained to date for a binary modulation format, reaching  $1 \frac{\text{bits}}{\text{s}\cdot\text{Hz}}$ . This is achieved using ordinary transmitter architecture. The requirements to achieve this tight channel spacing are proper channel spacing and digital receiver filtering to match the response of all the preceding filtering processes. The only other condition is time-alignment of the symbols on the different WDM channels. This feature may be considered in future WDM systems in order to achieve the spectral efficiency limit.

## CHAPTER 5. CHROMATIC DISPERSION COMPENSATION USING DIGITAL INFINITE-IMPULSE RESPONSE FILTERING

### 5.1. Introduction

The use of digital signal processing (DSP) technology in conjunction with coherent detection enables mitigation of various degrading effects unique to an optical fiber as a transmission channel. Among these are chromatic dispersion and polarization-mode dispersion [42]. As suggested in several papers [25, 69], for a symbol rate of  $T$ , a  $\frac{T}{2}$  tap delay finite impulse response (FIR) filter may be used to reverse the effect of fiber chromatic dispersion. The number of FIR taps required grows linearly with increasing dispersion. The number of (complex) FIR taps required to compensate first order chromatic dispersion is approximately [42]:

$$N = \frac{8Dz}{T_s^2} \quad (5-1)$$

where  $D$ ,  $z$  and  $T_s$  are the dispersion coefficient in  $\left[\frac{ps}{km \cdot nm}\right]$ , propagation length in  $[km]$  and analog-to-digital sampling interval in  $[ps]$ , respectively. This translates to approximately 51 complex taps to compensate for 1000km standard single-mode fiber (SSMF) propagation of a 10GBaud signal. The square dependence on bandwidth (and correspondingly-sampling rate) indicates how quickly this task becomes computationally intense. Moreover, a longer FIR filter introduces a longer delay and requires more area on a DSP chip. Efficient FIR filtering algorithms were suggested in [35], however, it is unclear how well these may perform for an arbitrary amount of accumulated dispersion. An efficient alternative to FIR filtering for dispersion compensation is clearly highly desirable.

In this chapter, infinite-impulse response (IIR) filtering for chromatic dispersion compensation (CDC) is considered as an alternative to FIR filtering. IIR filters inherently require a reduced number of taps for a similar response compared to their FIR counterparts due to the feedback path. Simulations and experimental results for real-coefficients IIR filtering used for CDC are discussed.

## 5.2. Theory

The underlying theory and design considerations for two classes of IIR filters, real-only and complex coefficients filtering, is presented in the following two sections.

### 5.2.1. Real Coefficients IIR Filters

The effect of dispersion is modeled as a linear filtering process given by:

$$\begin{aligned} y_r + jy_i &= (x_r + jx_i) \otimes (hf_r + jhf_i) \\ &= x_r \otimes hf_r - x_i \otimes hf_i + j(x_r \otimes hf_i + x_i \otimes hf_r) \end{aligned} \quad (5-2)$$

where  $y$ ,  $x$  and  $hf$  are the received, transmitted signals and the fiber impulse response, respectively and  $\otimes$  denotes convolution. Subscripts  $r/i$  designate the real and imaginary parts for each term. The all-pass (1<sup>st</sup> order) dispersion transfer function of a SSMF is:

$$H_f(\omega) = \exp \left\{ j \frac{\lambda_0^2 D z}{4\pi c} \omega^2 \right\} \quad (5-3)$$

where  $\omega, \lambda_0, D$  and  $z$  are baseband radial frequency, transmitter and local oscillator (LO) wavelength, fiber dispersion parameter at wavelength  $\lambda_0$  and the propagation distance, respectively. It can be readily shown that  $hf_r = F^{-1} \{ H_{f_r} \}$  and  $hf_i = F^{-1} \{ H_{f_i} \}$  where  $H_{f_r}$  and  $H_{f_i}$  are the real and imaginary parts of Eq. (5-3), respectively. Fourier transform (FT) of Eq.

(5-2) yields  $X(\omega) = Y(\omega) \cdot H_f^*(\omega)$ ; where the asterisk denotes complex conjugation. By separating into real and imaginary parts it is obtained that:

$$\begin{bmatrix} X_r \\ X_i \end{bmatrix} = M \begin{bmatrix} Y_r \\ Y_i \end{bmatrix}, M = \begin{bmatrix} H_{f_r} & H_{f_i} \\ -H_{f_i} & H_{f_r} \end{bmatrix} \quad (5-4)$$

where  $X_r, Y_r$  and  $X_i, Y_i$  are the FTs of the real and imaginary parts of the transmitted and received signals, respectively.

Noting that the phase response of the fiber is even, a stable all-pass IIR filter (of real or complex coefficients) cannot be designed to exactly match the fiber's response [70]. It is necessary then to express matrix  $M$  in Eq. (5-4) using monotonous phase response functions only. Defining  $\tilde{H}_f = H_{f_r} - H_{hilb}H_{f_i}$  (where  $H_{hilb} = -j \cdot \text{sign}(\omega)$  is the transfer function of the Hilbert transform), matrix  $M$  can be rewritten as:

$$M = \frac{1}{2} \begin{bmatrix} \tilde{H}_f + \tilde{H}_f^* & H_{hilb}(\tilde{H}_f + \tilde{H}_f^*) \\ H_{hilb}(\tilde{H}_f^* - \tilde{H}_f) & \tilde{H}_f + \tilde{H}_f^* \end{bmatrix} \quad (5-5)$$

In SSMF at  $\lambda_0 = 1550_{nm}$ ,  $D > 0 \frac{ps}{km \cdot nm}$ . This implies that the phase response of  $\tilde{H}_f$  increases monotonously, and the response of  $\tilde{H}_f^*$  monotonously decreases. Hence, the group delay (GD) of  $\tilde{H}_f^*$ , defined as  $GD(\omega) = -\frac{d}{d\omega} \arg\{\tilde{H}_f^*(\omega)\}$ , is always positive, making  $\tilde{H}_f^*$  causal. A real-coefficients IIR filter having a response matching (as much as possible) to  $\tilde{H}_f^*$  may be designed using several methods [71].

The IIR filter's order  $N$  is chosen using the following argument. Each order of the IIR filter contributes a  $\pi$  phase shift in the IIR filter phase response. At the band edge (half the sampling rate) a total phase of  $N\pi$  radians is accumulated [70]. To allow CDC, sampling at  $2B_r$  is



required,  $B_r$  being the symbol rate. To find the filter order which best matches a given dispersion, Eq. (5-3) may be used when the phase at the band edge is considered ( $\omega = 2\pi B_r$ ):

$$N = \text{round} \left( \lambda_0^2 D z \frac{B_r^2}{c} \right) \quad (5-6)$$

Using Eq. (5-6), every additional filter order (i.e., 2 taps) compensates for approximately 78km (using  $D = 16 \frac{ps}{km \cdot nm}$ ,  $B_r = 10GBaud$ ) of SSMF transmission.

The filter  $\tilde{H}_f$ , having an inverse phase response compared to  $\tilde{H}_f^*$ , is non-causal and unstable. It is therefore necessary to implement an equivalent filtering process to  $\tilde{H}_f$  using  $\tilde{H}_f^*$ . By inserting Eq. (5-5) instead of  $M$  in Eq. (5-4), the FT of the real part of the transmitted signal is given by:

$$X_r = \frac{1}{2} [\tilde{H}_f^*(Y_r - H_{hilb} Y_i) + \tilde{H}_f(Y_r + H_{hilb} Y_i)] \quad (5-7)$$

The term containing  $\tilde{H}_f^*$  in Eq. (5-7) is easily obtained since  $\tilde{H}_f^*$  is stable and causal. To obtain the term containing  $\tilde{H}_f$ , an equivalent expression is considered:  $\tilde{H}_f(Y_r + H_{hilb} Y_i) = [\tilde{H}_f^*(Y_r + H_{hilb} Y_i)^*]^*$ . Noting that a complex conjugate of a signal's FT is equivalent to a time-reversal operation, the required filtering process can be implemented using a time reversal device. The time-reversal technique was previously studied for non-causal filtering achieving linear phase response using IIR filters [72]. A block diagram of the required filtering scheme which allows DC for  $x_r$  is presented in Figure 5-1. This approach can be extended to obtain the imaginary part of the transmitted signal,  $x_i$ .

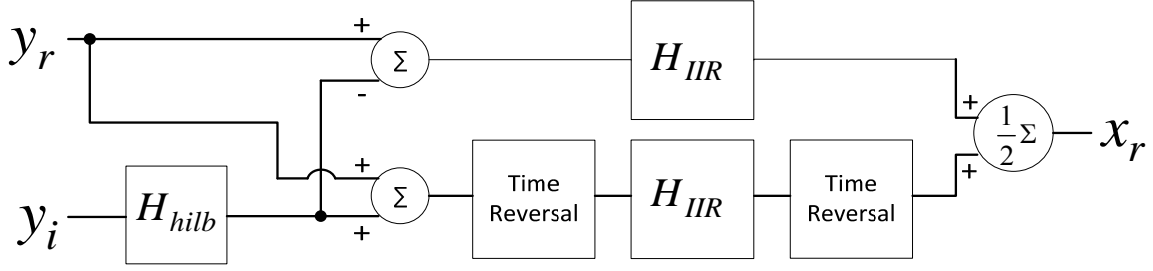


Figure 5-1: Block diagram for DC of the real part of a transmitted signal

### 5.2.2. Complex Coefficients IIR Filters

The Real-coefficients IIR filtering scheme presented above provides good matching with the fiber's phase response. However, there is a large overhead (from the Hilbert transformer) and special design considerations (time-reversal device) that limit the overall value of this approach. A different approach to achieve CDC using IIR filtering is to use a complex-coefficients IIR filter, where the filter coefficients are obtained such that the GD matches the inverse of that of the fiber. The fiber's inverse GD response is given by:

$$GD_{\text{desired}}(\omega) = \beta_2 z \omega \quad (5-8)$$

where  $\beta_2$ ,  $z$  and  $\omega$  are the group velocity dispersion parameter, propagation distance and angular frequency offset (with reference to frequency for which  $\beta_2$  is quoted). The suggested filter's z-domain response is given by [73]:

$$H(z) = p_r p_i \frac{z - \frac{j}{p_i}}{z - j p_i} \frac{z - \frac{1}{p_r}}{z - p_r} \quad (5-9)$$

where  $p_i$  and  $p_r$  are real. This is a 2<sup>nd</sup> order IIR filter (referred to as a bi-quadratic filter).

Figure 5-2 shows the CDC (desired) GD and that of an IIR complex filter for dispersion of  $304 \frac{ps}{nm}$  versus normalized frequency. A complex coefficients IIR filter is practically impossible

to design such that the response is matched in the entire frequency band [73]. However, Figure 5-2 demonstrates that the response can be designed to match well within a limited band (in this case  $[-0.6, 0.6]$ ). This implies that some degree of over-sampling is required when complex IIR filtering is to be employed. The tradeoff between computational efficiency and higher sampling rate must be considered. Moreover, the total amount of CDC that can be achieved using this filtering approach is limited. As with any other filtering scheme, several filters may be cascaded to accumulate the delay required at each frequency, at the cost of computational efficiency. Nevertheless, complex IIR filtering is highly efficient for small dispersion values. The rest of this chapter will concentrate on real-coefficients IIR filtering. The usefulness of complex-coefficients IIR filters will be demonstrated in the following chapter, where distributed compensation is considered.

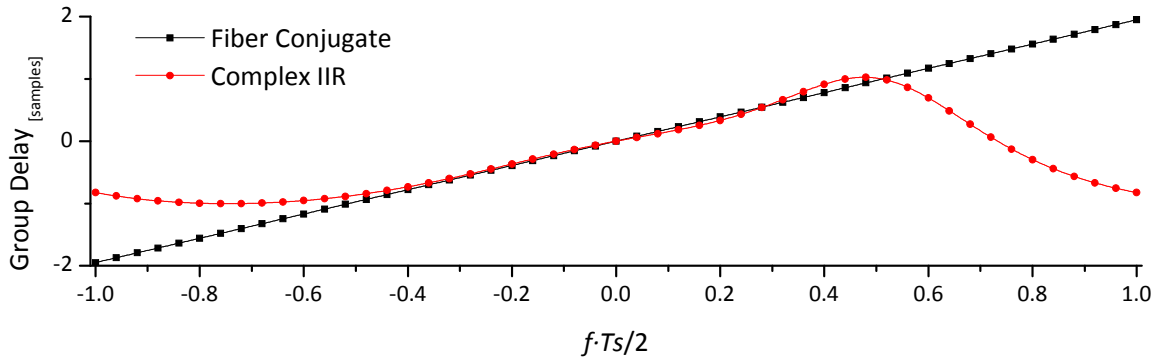


Figure 5-2: Desired and complex IIR GD vs. normalized frequency

### 5.3. Simulation

Simulation of a  $10\text{GBaud}$  BPSK system with  $D = 16 \frac{\text{ps}}{\text{km} \cdot \text{nm}}$  is considered. To isolate the effect of dispersion, laser linewidth and fiber nonlinearity were not considered. CDC was achieved using a 6<sup>th</sup> order IIR Hilbert-transformer and an IIR filter of appropriate order that

matches the dispersion of the fiber, as obtained in Eq. (5-6). Eye closure penalty eye (ECP) is defined as:

$$ECP = -10 \log_{10} \left( \frac{\text{Dispersion compensated eye opening}}{\text{Back to back eye opening}} \right) \quad (5-10)$$

The ECP for the IIR filtering scheme as a function of total dispersion (and IIR filter order) is presented in Figure 5-3. The FIR filter orders which achieve the same ECP as the IIR filter are presented for selected total dispersion values. For the first simulated point, 11 complex FIR taps are required. For FIR filtering approximately 5.8 additional (complex) taps are required to compensate each additional  $1248 \frac{ps}{nm}$  of total dispersion. IIR filtering requires only 1 additional filter order (2 additional real taps). The number of coefficients required for FIR filtering quoted here is approximately 50% higher than suggested by Eq. (5-1). This is due to the fact that for this simulation the FIR coefficients were calculated using an inverse FT (as in [25]) rather than directly in the time-domain (as in [42]). The inverse-FT leads to better performance at the expense of higher computational cost.

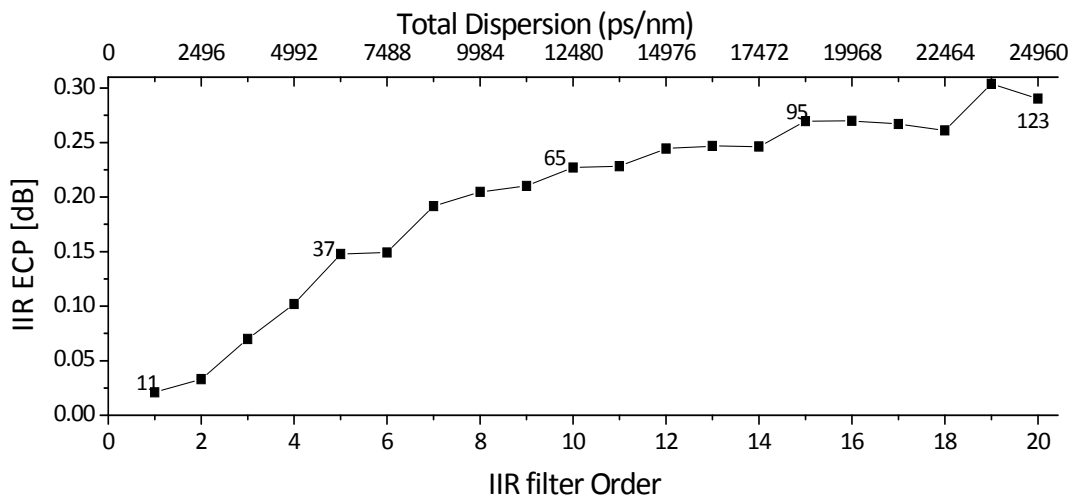


Figure 5-3: ECP as a function of total dispersion/ IIR filter order

At larger total dispersion values, the IIR filter ECP grows slightly. This is explained by the fact that in designing the IIR filter, less degree of freedom is available compared to FIR design because of the reduced filter order. Better IIR design algorithm may reduce this problem.

To compare the actual benefit of IIR versus FIR CDC, the number of operations in each case is considered. At large dispersion values, the overhead incurred by the Hilbert transformer in the IIR case becomes negligible and the ratio between the number of operations needed for FIR versus IIR filtering is given by  $\frac{N_{FIR}}{2 \cdot N_{IIR}}$ , where  $N_{FIR}$  and  $N_{IIR}$  are the FIR and IIR filter orders, respectively. Simulations suggest a reduction of 2.5 times or more in the number of operations required by IIR compared to FIR is achieved starting at  $15,000 \frac{ps}{nm}$ .

#### 5.4. Experimental setup

To verify the effectiveness of the proposed IIR filtering scheme, a 10GBaud BPSK transmission system was set up as shown in Figure 5-4.

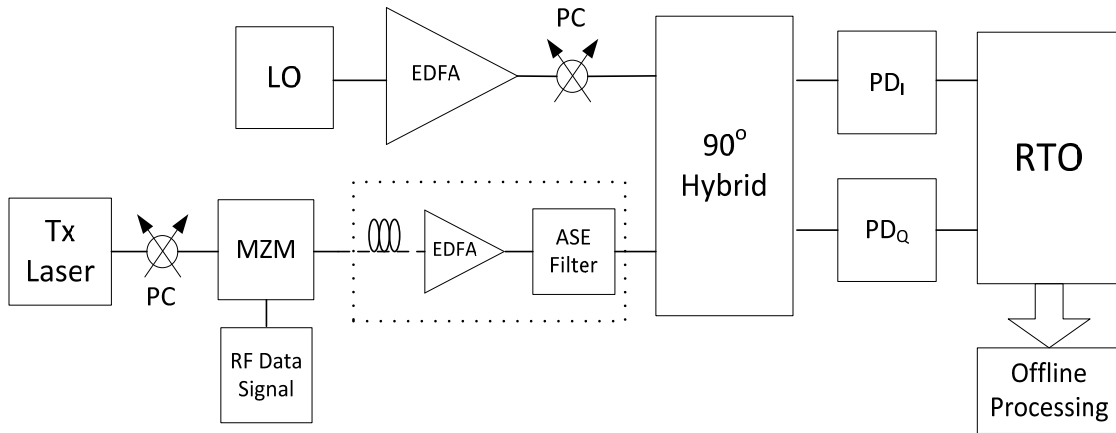


Figure 5-4: Experimental setup for BPSK transmitter/phase diversity receiver

A Mach-Zehnder modulator (MZM) was biased (at 0 transmission) and driven (at  $2V_{\pi}$ ) to achieve BPSK modulation. Pseudo-random bit sequence (PRBS) of length  $2^{15} - 1$  was used. Back-to-back, 80km and 160km transmission distances were considered. SSF used had

dispersion parameter and attenuation coefficient of  $D = 16 \frac{ps}{km \cdot nm}$  and  $\alpha = 0.2 \frac{dB}{km}$ , respectively. Launched optical power into each span was 2.5dBm. An Erbium-doped fiber amplifier (EDFA) with appropriate amplified spontaneous emission (ASE) filter was used at each span to compensate for attenuation. The LO wavelength and polarization were carefully tuned to match that of the transmitter laser. A phase diversity receiver and subsequent sampling using a  $40 \frac{GSamples}{sec}$  real-time oscilloscope (RTO) were used for detection. The samples were re-sampled to  $20 \frac{GSamples}{sec}$  and processed offline. DC was implemented using the IIR filtering technique described above. A 6<sup>th</sup> order IIR Hilbert-transformer was used. Phase estimation was achieved as in [25] and the best back-to-back Q-factor of 17.17dB was measured. DC for 80km and 160km was achieved using 1<sup>st</sup> and 2<sup>nd</sup> order IIR filters, respectively. The eye diagrams for 80km and 160km obtained using IIR filtering are presented in Figure 5-5.

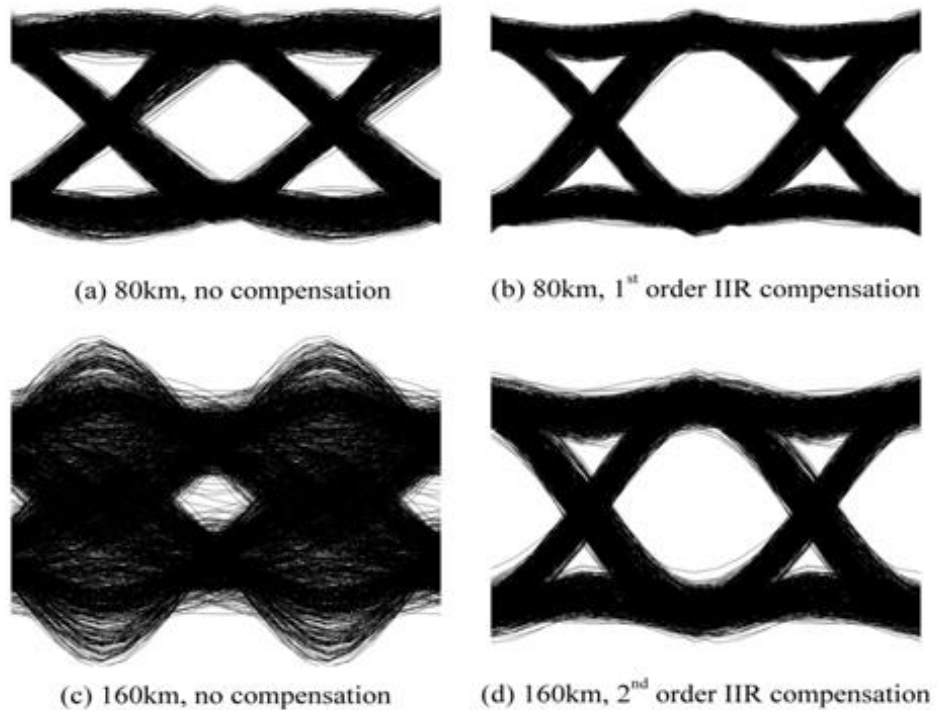


Figure 5-5: Eye diagrams with and without IIR DC, 80km and 160km

When IIR filtering was implemented, the Q-factor was improved from  $9dB$  to  $13.44dB$  and from  $3.64dB$  to  $10.16dB$ , for  $80km$  and  $160km$  transmission distances, respectively. In the FIR filtering case the resulting Q-factors after DC were  $11.91dB$  (using 14 taps) and  $9dB$  (using 20 taps), for  $80km$  and  $160km$  transmission distances, respectively. It can be concluded that an additional  $80km$  span requires only one more order for the IIR filter (2 taps). In the FIR case, 6 complex taps are necessary.

### 5.5. Extension to Larger Dispersion Values

Verification of the IIR filtering approach was presented in the previous section, where experimental results were obtained up to  $160km$  ( $2560 \frac{ps}{nm}$ ) of SSMF transmission. In this section the total accumulated dispersion is extended to higher values, up to  $25192 \frac{ps}{nm}$ . For this purpose, a recirculating loop was constructed, as shown in Figure 5-6. An MZM biased at zero transmission and driven at  $2V_\pi$  was used to generate  $10GBaud$  BPSK modulation; PRBS of length  $2^{23}-1$  was used. EDFA1 and a subsequent ASE filter were included in order to boost the signal going into the loop to a level of  $-2.2dBm$  (at the SSMF input). Acousto-optic switch 1 was used to fill the loop with the signal from the transmitter. Acousto-optic switch 2 closed after the loop was filled and each recirculation loss was compensated by EDFA2 which was set to have gain of  $32.1dB$ . The total loop loss includes all the elements in the loop: fiber loss, ASE filter, PC, acousto-optic switch 2 insertion losses, and the loop coupler loss. The loop included SSMF of length  $78.7km$ , dispersion coefficient  $D = 16 \frac{ps}{km \cdot nm}$  and loss coefficient  $\alpha = 0.2 \frac{dB}{km}$ . A homodyne phase-diversity receiver was implemented using an LO laser boosted by EDFA3 and a PC which was used to align the polarization of the incoming signal after each span. A  $90^\circ$  hybrid

was used to obtain the in-phase and quadrature components of the transmitted signal. The outputs from the  $90^\circ$  hybrid were detected using 2 photo-detectors ( $PD_{I/Q}$ ) and sampled using an Agilent Infinium DSO81204A RTO at  $40 \frac{GSamples}{sec}$ . Subsequent offline processing included resampling to  $20 \frac{GSamples}{sec}$ , CDC and demodulation. Phase estimation was achieved as in [25]. It is sufficient to implement the analog-to-digital conversion at  $20 \frac{GSamples}{sec}$ . However, the RTO used has an anti-aliasing filter which is matched to  $40 \frac{GSamples}{sec}$  rate. Setting the sampling rate at  $20 \frac{GSamples}{sec}$  would lead to unnecessary aliasing. Resampling to the required Nyquist rate ( $2B_r$ ) is hence done in the digital domain where an anti-aliasing filter is implemented within the resampling process. CDC was achieved using the IIR filtering technique described in the section 5.2.1. . The Hilbert-transformer filter is a 6<sup>th</sup> order IIR filter.

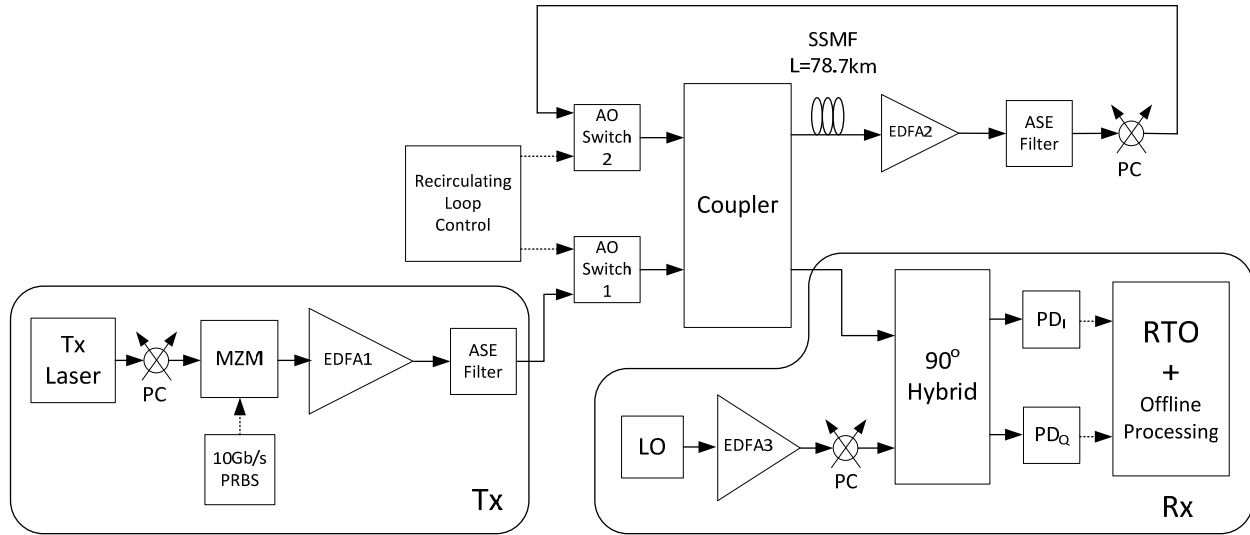


Figure 5-6: 10GBaud BPSK recirculating loop experimental setup

25k samples were used to calculate the decision-threshold Q-factor obtained after phase estimation. The back-to-back Q-factor was found to be approximately 18.8. The Q-factor values as a function of total dispersion (or IIR order/ number of spans, which are linearly



related) are plotted in Figure 5-7. For comparison, the best Q-factor obtained by FIR filtering is also plotted. For the FIR results the filter length can be arbitrarily long.

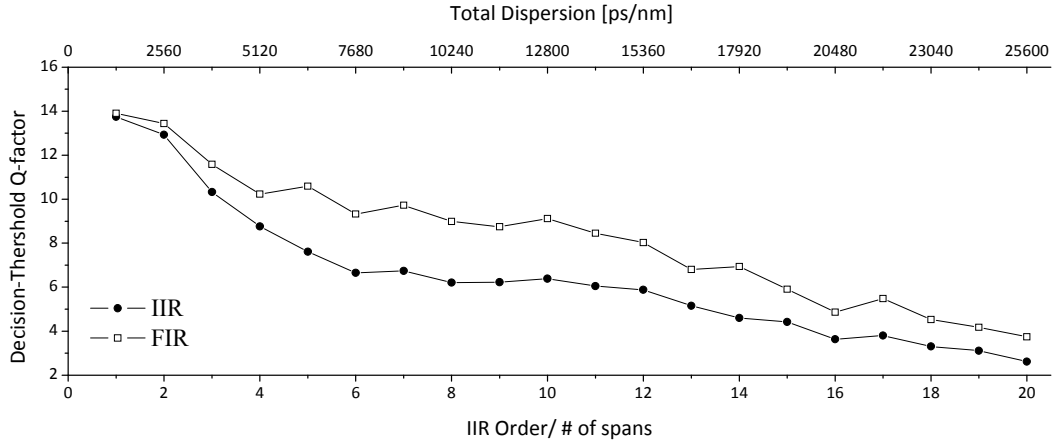


Figure 5-7: Q-factor vs. total dispersion/IIR order

From Figure 5-7 it is clearly seen that IIR filtering can be used for DC of large dispersion values. The FIR filtering scheme slightly out-performs the IIR scheme (FIR Q-factor is on average approximately 1.5dB higher).

To compare the actual benefit of IIR versus FIR DC, the number of operations (NOP) in each case is considered. The FIR filter order is chosen such that a 1dB in Q-factor penalty is allowed (this value also approximates the performance of FIR filtering with that of IIR). It is found that each span (approximately  $1260 \frac{ps}{nm}$ ) requires additional 2.7 complex FIR taps. The obtained FIR filter order (per span) is used for the calculation of NOP required using the formula given in the theoretical section. The NOR ratio (FIR/IIR) is shown in Figure 5-8. FIR filtering requires a factor of approximately 1.7 in NOP compared to IIR, for large dispersion values. Further NOP reduction is expected if a better IIR filter design is implemented.

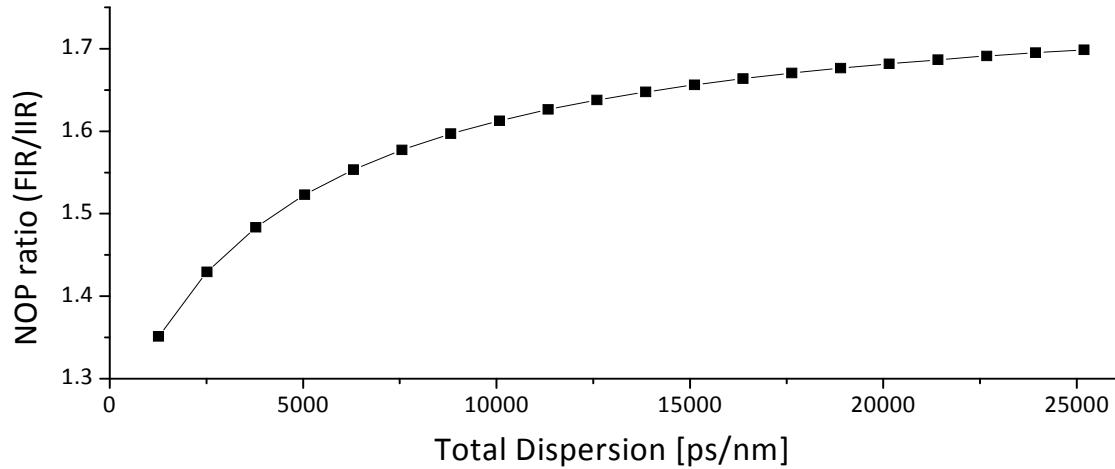


Figure 5-8: Number of operations ratio vs. total dispersion

## 5.6. Conclusion

As seen from both the simulation and experimental results, the IIR filtering approach can be used to mitigate chromatic dispersion for optical transmission systems employing a phase diversity receiver with subsequent sampling and DSP. The benefit obtained by this approach is the reduced tap count required by the IIR filter to achieve CDC, which originates from the inherent feedback process in IIR filtering. This advantage becomes more significant at longer transmission distances since the overhead incurred by the Hilbert transformer is constant. The use of an iterative process to obtain the IIR filter coefficients does not guarantee perfect matching between the actual IIR filter response and the desired response [conjugate of Eq. (5-3)]. This leads to a small penalty for IIR filtering compared to FIR filtering with larger dispersion values. The penalty may be reduced by cascading the IIR filter with a low tap-count (complex) FIR filter to compensate for the small discrepancy between the desired and obtained IIR responses. The IIR scheme involves time-reversal operations. The benefit from the reduced number of operations required by IIR filtering is to be weighed against the added complexity of the time-reversal operation and the effect on real-time implementation through parallelization.

## CHAPTER 6. DISTRIBUTED COMPENSATION

### 6.1. Introduction

As discussed in chapter 4, one of the benefits from coherent detection is the ability to achieve high spectral efficiency. This may be accomplished in several ways: tight channel spacing (e.g. orthogonal wavelength-division multiplexing, OWDM, where channel spacing is equal to the symbol rate [32]), polarization multiplexing [15], advanced modulation formats such as quadrature amplitude modulation or a combination of these techniques. A major difficulty in realizing any of these techniques is the combined degrading effects of fiber nonlinearity and dispersion. One possibility of combating these effects is backward-propagation, which is discussed in this chapter.

The concept of backward-propagation stems from Yariv *et al.* which suggested in 1979 the use of optical phase conjugation for dispersion compensation [74]. Fisher *et al.* extended this notion in 1983 to compensation of both dispersion and Kerr nonlinearity [75]. The use of a medium with negative nonlinear index,  $n_2$ , (such as semiconductors) to reverse the effects of transmission without phase conjugation was suggested in [76]. An examination of the nonlinear Schrödinger equation (NLSE) which governs the evolution of optical signal propagation in fiber reveals that all these techniques amount to reversing the fiber parameters (either dispersion, nonlinear index, or both). This is mathematically equivalent to reversing the spatial variable sign in the NLSE and hence the suggested technique is referred to as backward-propagation. The immense flexibility of DSP allows solving the NLSE without resorting to hardware-based solutions. Using DSP, the various algorithm implementation parameters can be modified freely to accommodate for the transmission medium, power levels and bandwidth.

Mitigation of nonlinear effects may be achieved in the optical domain (e.g. through dispersion-managed systems [1] or optical phase conjugation [47]) or by electronically pre-distorting the signal before propagation [12, 36, 77, 78]. Experimental demonstrations using dispersion-managed links with subsequent nonlinear phase fluctuation mitigation (lumped post-compensation) using DSP are presented in [30, 79]. As opposed to these compensation techniques, digital post-compensation offers great flexibility since adaptive compensation can be incorporated.

A digital real-time universal backward-propagation scheme for post-compensation of both chromatic dispersion and nonlinear effects in a WDM environment was shown to be not only effective but also computationally feasible given advances in integrated circuits [13]. In the backward-propagation scheme, the NLSE with the spatial variable negated is solved by using the split-step method (SSM). The SSM is implemented by dividing the total propagation distance into a finite number of steps; for each step, small nonlinear and dispersion effects are compensated correspondingly [80]. This technique imitates a backward-propagating signal, thus eliminating the degrading effects from the combination of nonlinearity and dispersion and is viewed as distributed compensation.

In this chapter, the possibility of achieving impairment compensation by backward-propagation is demonstrated. An experimental demonstration of viability of the SSM approach is presented. Several techniques to allow a more computationally efficient implementation of the SSM are suggested. These include the use of infinite-impulse response filtering and wavelet-based finite-impulse response filter design for the SSM linear operator implementation.

## 6.2. Backward Propagation Scheme

Backward-propagation is achieved by solving the NLSE with the spatial variable negated. In the following, a single polarization is assumed and hence the desired NLSE can be written in its scalar form [80]:

$$\frac{\partial A}{\partial(-z)} = (\hat{D} + \hat{N})A \quad (6-1)$$

where  $A$  is the complex electric field,  $\hat{D}$  is the differential operator accounting for dispersion and fiber loss and  $\hat{N}$  is the nonlinear operator. These operators are given by [1]:

$$\hat{D} = -\frac{j}{2}\beta_2 \frac{\partial^2}{\partial t^2} - \frac{\alpha}{2} \quad (6-2a)$$

$$\hat{N} = j\gamma_{NL}|A|^2 \quad (6-2b)$$

where  $\alpha$ ,  $\beta_2$  and  $\gamma_{NL}$  are the attenuation factor, group-velocity dispersion parameter and the effective nonlinearity parameter, respectively. The symmetric-SSM is employed by dividing each fiber span into  $N_s$  steps of  $z_{step}$  length each. The total propagation length for  $N_{spans}$  is  $z_{fiber} = N_{spans} z_{span}$  where  $z_{span} = N_s z_{step}$ . For each step the corresponding dispersion [Eq. (6-2a)] and nonlinearity [Eq. (6-2a)] compensation are performed, as shown in Figure 6-1. The symmetric-SSM is used; dispersion is compensated in two steps, each accounting for half of the accumulated dispersion per step. Dispersion compensation can be implemented in the frequency domain [via Fourier transform (FT) of the signal] or directly in the time domain using finite impulse response (FIR) filtering. The FT approach would be more efficient for large dispersion values; however, for this setup, the total amount of dispersion to be compensated per step is small and FIR filtering is sufficient. FIR filtering is also preferred since it does not

require dividing the incoming signal into blocks and hence, it is compatible with real-time implementation of backward propagation. Infinite-impulse response (IIR) filtering can also be considered for dispersion compensation as will be discussed in section 6.5. Fiber loss is accounted for at each step, while amplification is reversed after each span (Figure 6-1, single span module). Compensation for the entire propagation length is achieved by repeating these steps (Figure 6-1, bottom). This process can be viewed as distributed compensation since the entire link is divided into segments, as opposed to lumped techniques (e.g., dispersion compensation only, which acts on the entire link length at once).

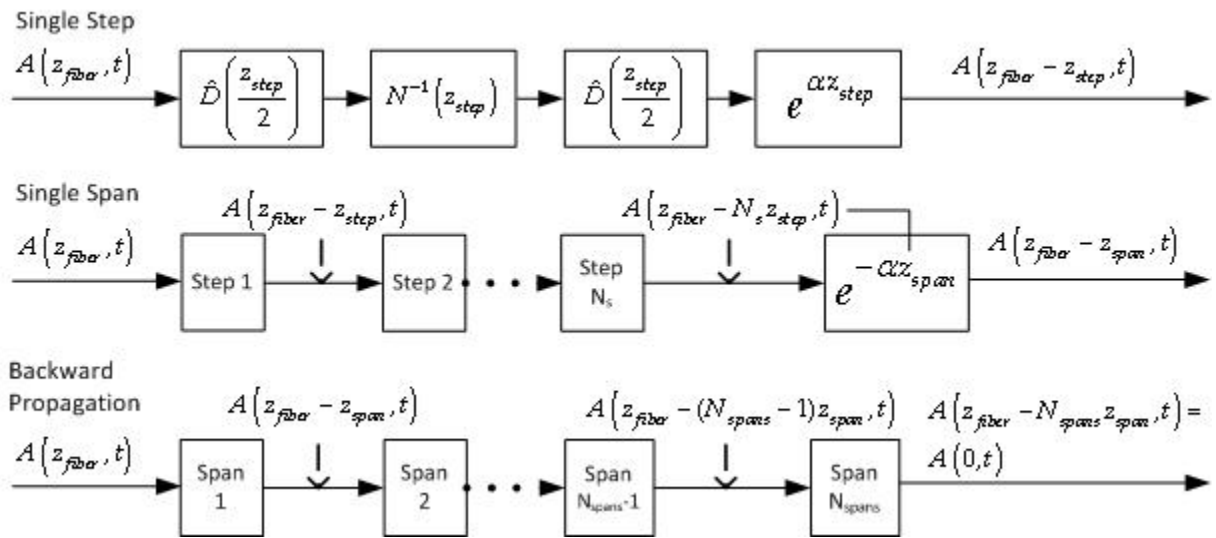


Figure 6-1: Symmetric-SSM backward propagation block diagram

### 6.2.1. Step-size Dependence

In order for the SSM to provide an accurate solution to the NLSE, the step-size should be chosen to be small enough so that the assumption that dispersion and nonlinearity act independently is valid [80]. There are several characteristic lengths which must be taken into account when choosing an appropriate step size. These are the dispersion, cross-phase modulation (XPM) and four-wave mixing (FWM) lengths.

The SSM step-size is chosen to be (preferably much) smaller than the shortest of these characteristic lengths. It is important to note that the step size should provide an adequate solution to the NLSE, yet should not be chosen to be too small since a smaller step size would not achieve better performance, but will introduce higher computational load. The performance limit is due to the non-deterministic effects which cannot be considered in the NLSE. The major contributor to these non-deterministic effects is amplified spontaneous emission (ASE) generated in the optical amplifiers throughout the transmission link. The characteristic lengths are summarized below:

$$\text{Dispersion [1]} \quad L_D = \frac{1}{\beta_2 \Delta f^2} \quad (6-3)$$

$$\text{XPM [80]} \quad L_{XPM} = \frac{1}{\gamma_{NL} \left(2 - \frac{1}{N_{ch}}\right) P_{eff}} \quad (6-4)$$

$$\text{FWM [81]} \quad L_{FWM} = \frac{1}{\pi \Delta \nu^2 |\beta_2| (N_{ch} - 1)^2} \quad (6-5)$$

where  $\Delta f$ ,  $\Delta \nu$  and  $N_{ch}$  are the total bandwidth of interest, channel spacing and total number of channels. The effective power  $P_{eff} = \frac{P_L}{z_{span}} \int_0^{z_{span}} e^{-\alpha z} dz \cong 0.28 P_L$  (where  $P_L$  is the total launching power) is used to accommodate for the variation in nonlinear effects due to fiber loss between amplification stages.

### 6.3. Experimental Setup

To experimentally verify the feasibility of the SSM for backward-propagation, an experiment was conducted (see Figure 6-2). Three distributed-feedback lasers were used as WDM carriers. The center channel ( $\lambda_c$ ) is binary-phase shift keying (BPSK) modulated using a

Mach-Zehnder modulator (MZM) driven at  $6\text{Gbaud}$  by a pattern generator (PG). Pseudo-random bit sequence of length  $2^{23} - 1$  was used. A symbol rate of  $6\text{GBaud}$  was chosen in order to fit three WDM channels within the (full) analog bandwidth of  $24\text{GHz}$  of the real-time oscilloscope (RTO). Larger analog bandwidth would allow higher symbol rates and more OWDM channels. Two adjacent channels ( $\lambda_R$  and  $\lambda_L$ ) are also BPSK modulated and combined with the center channel. The OWDM channels are tightly spaced at  $7\text{GHz}$  rather than  $6\text{GHz}$ , which was found to give the lowest linear crosstalk due to non-ideal waveforms [32]. Adjacent channels have synchronized symbol times (using an electrical delay) but decorrelated data content compared to the center channel (through an optical delay in the center channel path). Polarization controllers (PCs) were placed at the appropriate locations and a polarization analyzer was used to insure that all the channels are launched into the fiber having parallel polarizations. The power levels of the center and adjacent channels were equalized using optical attenuators.



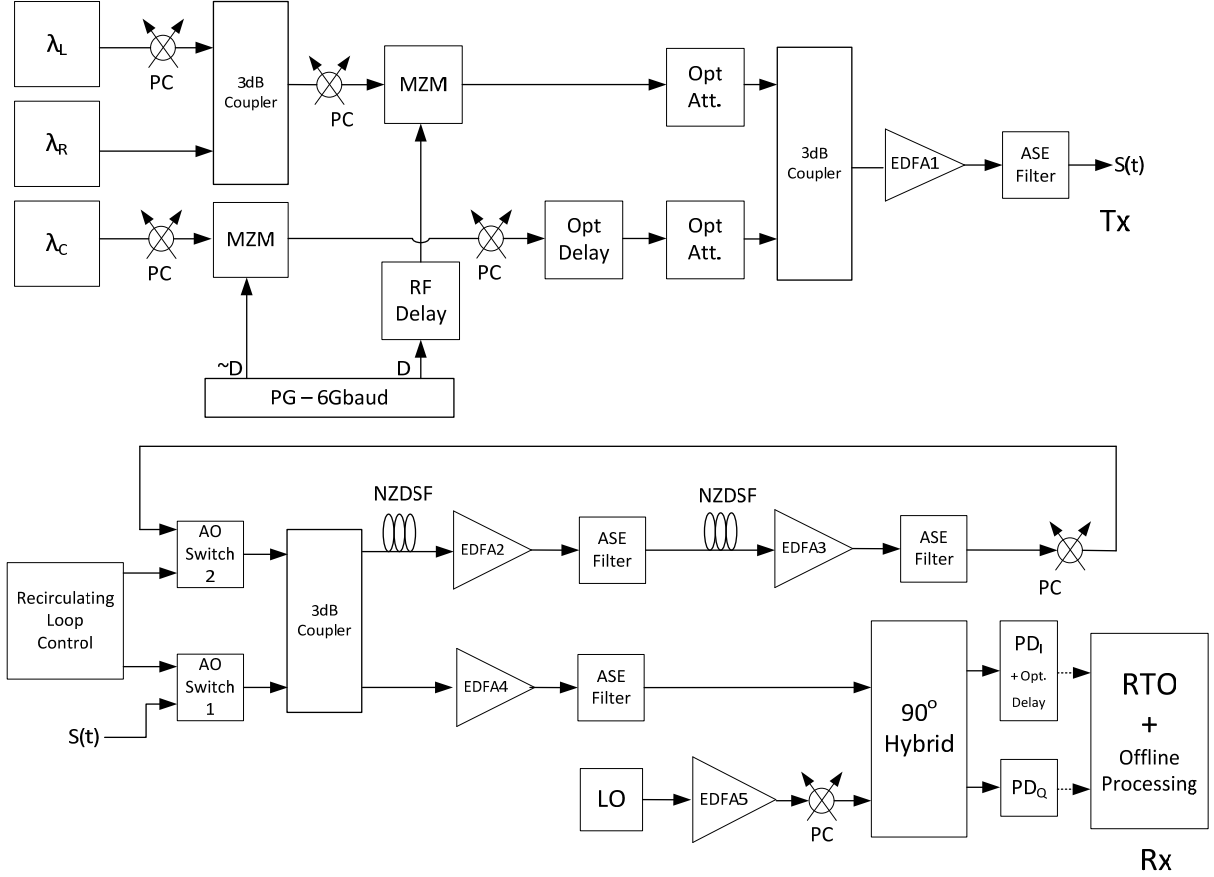


Figure 6-2: Experimental setup for backward-propagation

The total launching power ( $P_L$ ) was varied set using an Erbium-doped fiber amplifier (EDFA), calibrated to the insertion losses associated with the recirculating loop components. The recirculating loop consisted of two non-zero dispersion-shifted fiber (NZ-DSF) spools, with a combined length of  $152.82\text{km}$ . The fiber parameters were:  $\alpha = 0.2 \frac{\text{db}}{\text{km}}$ ,  $\beta_2 = -4.9 \frac{\text{ps}^2}{\text{km}}$  and  $\gamma_{NL} = 1.46 \frac{1}{\text{W} \cdot \text{km}}$ . NZ-DSF was chosen for this experiment as it is widely deployed. A phase diversity receiver was used to beat the transmitted optical signal with the local oscillator (LO). For the LO an external cavity laser tuned to the center channel was used. The RTO was used for digitization of the two signal quadratures at  $40 \frac{\text{GSamples}}{\text{sec}}$ . Digital signal processing was performed offline.

## 6.4. Experimental Results

The experimental datasets were processed using the SSM as described in section 6.2. The characteristic lengths according to Eq. (6-3) to Eq. (6-5) were found to be  $L_D \cong 350km$  (where the full bandwidth  $\Delta f = 24GHz$  is taken),  $L_{XPM} \cong 368km$  ( $P_L = 6dBm$ , which is the highest used in this experiment) and  $L_{FWM} \cong 105km$  (using a channel spacing of  $\Delta\nu = 7GHz$ ). All the characteristic lengths are found to be longer than a single spool length,  $\sim 80km$ . The presence of periodically spaced EDFAs within the link dictates that the maximum step size should be limited to a single spool length. From these considerations, the step size of  $80km$  was chosen. The total walk-off between adjacent channels is  $\Delta\tau = 2\pi\Delta\nu|\beta_2|z$ , where  $\Delta\nu = 7GHz$  is the channel spacing. For  $1000km$  transmission this amounts to 1.3 symbols; hence, XPM will indeed be a degrading factor. Moreover, the low dispersion value allows FWM products to be generated. The FWM efficiency is roughly 96% and the periodic amplification guarantees accumulation of FWM effect throughout the link. After backward propagation, proper OWDM filtering (as described in chapter 4), phase estimation and decision threshold Q-factor calculation for the center channel were performed.

The correct choice of the SSM step size can be verified by applying backward-propagation with decreasing step sizes. This serves as a verification of the step size chosen (e.g.,  $80km$  for  $P_L = 6dBm$ ). In Figure 6-3, the dependence of Q-factor penalty on the SSM step-size is plotted for varying launch powers. It is evident from this plot that larger launch powers require the SSM to be implemented with smaller step sizes since nonlinear effects are dominant in this system. Moreover, it is verified that a step size of  $\sim 80km$  is sufficient for all launching powers considered in this experiment.

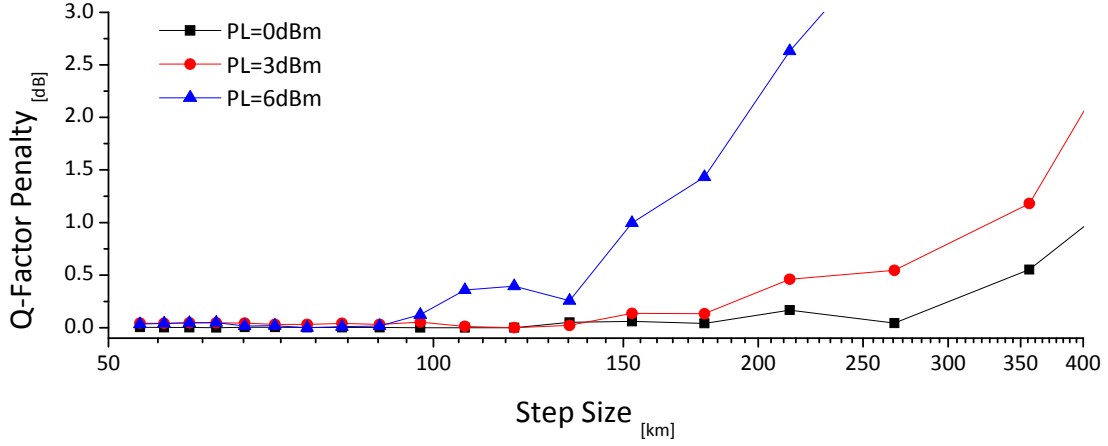


Figure 6-3: Q-factor penalty vs. step size for varying  $P_L$

To evaluate the benefit of using distributed compensation, other possible compensation techniques were considered. The first consisted of chromatic dispersion compensation (CDC) only. The second was lumped compensation which included CDC followed by a single nonlinear compensating operation consisting of a phase shift proportional to the signal power. In Figure 6-4, the back-to-back, CDC, lumped compensation and distributed eye diagrams for 760km NZ-DSF transmission with  $P_L = 6dBm$  are shown. The distributed method yields a clear open eye.

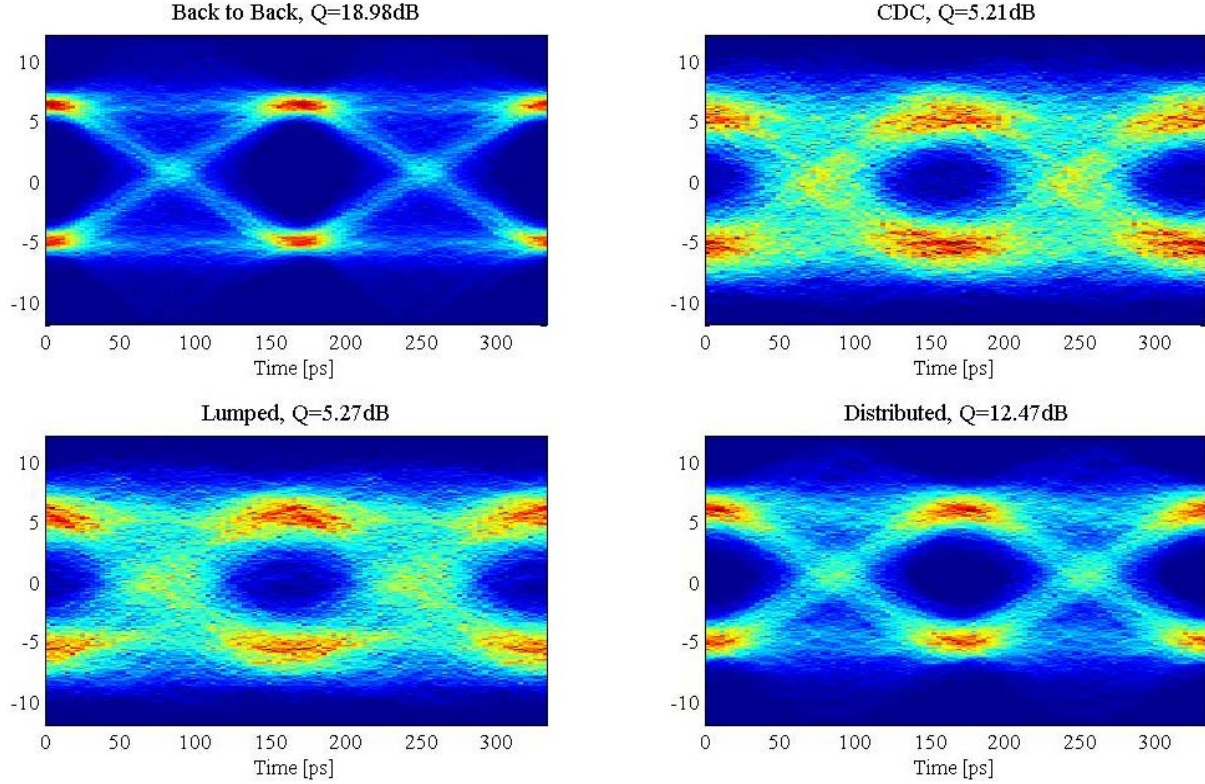


Figure 6-4: Eye diagrams for (a) back-to-back and after 760km with compensation using: (b) CDC (c) Lumped (d) Distributed

The decision-threshold Q-factors for CDC, lumped compensation and distributed compensation as a function of transmission distance are presented in Figure 6-5, for  $P_L = 0, 3$  and  $6dBm$ . Lumped compensation achieves a better result compared to CDC only at short propagation distances and higher power levels. This can be explained by the fact that lumped compensation can be viewed as a single-step SSM (for the entire propagation distance). For distances which far exceed the dispersion length of  $L_D = 350km$ , lumped compensation cannot provide better performance than CDC. The distributed compensation scheme (namely SSM) has a much smaller step size; hence, it achieves superior performance. This method clearly outperforms CDC or lumped compensation (e.g. for  $Q = 10dB$ , CDC or lumped compensation allow propagation of approximately  $520km$  while the distributed compensation allows more than double the distance, approximately  $1150km$ ).

It is observed that the Q-factor slopes as a function of distance become steeper with larger launch powers. This is explained by the fact that higher launch powers are harder to compensate, for two main reasons. The first being nonlinear products that fall out of the RTO detection bandwidth. As these are not available for backward-propagation, a larger penalty is introduced with growing  $P_L$ . The second reason is the non-deterministic noise sources in the link (i.e. signal-ASE beat), which cannot be compensated for due to their stochastic nature. The implication of this behavior is that for a certain transmission distance, an optimal launching power exists. Higher power levels would actually result in deterioration of performance. This is in strict opposition to a lineal channel where any penalty can be overcome by launching higher signal powers.

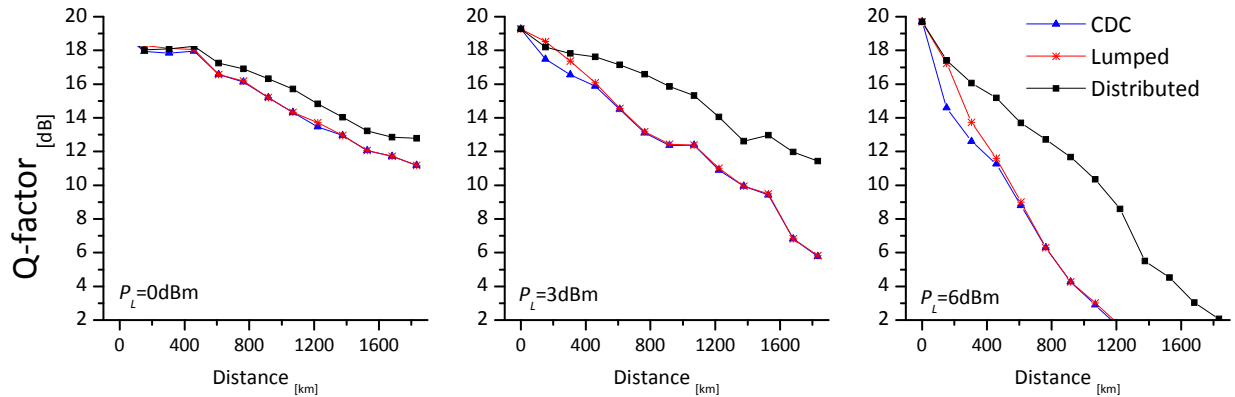


Figure 6-5: Q-factor vs. propagation distance

## 6.5. SSM with Infinite-Impulse Response Filtering

Implementation of the SSM is highly resource-consuming since multiple stages of linear and nonlinear operations must be employed. Any simplification or efficient algorithm to reduce the amount of required operations would render this approach much more feasible. Since dispersion compensation is the more resource-hungry of the two operators in the SSM, reduction in computational load for this operator is considered.

The complex-coefficients infinite impulse response (IIR) filter was presented in section 5.2.2. It is considered for the linear operator for the SSM since the dispersion value to compensate for at each step is small. This is exactly the scenario where complex-IIR filtering would serve better for dispersion compensation, compared for FIR filtering.

A small modification to the symmetric-SSM is considered first, since the complex-coefficients IIR filter group-delay (GD) does not necessarily match the required GD to achieve CDC. Any mismatch between the IIR filter GD and that of the desired GD accumulates with each step of the SSM. As a remedy, the first IIR filter at each step is designed to match (as best as possible) the required GD for the associated propagation length  $\left(\frac{z_{step}}{2}\right)$ , while the second is optimized to compensate not only for the GD from the second half of the fiber propagation at that step, but for the error in GD compensation introduced by the first filter. The GD required for the linear operator (for the first spool in the recirculating loop) and provided by those of the first IIR and complimentary (second) optimized IIR filters are shown in Figure 6-6, as a function of normalized frequency with respect to the sampling frequency.

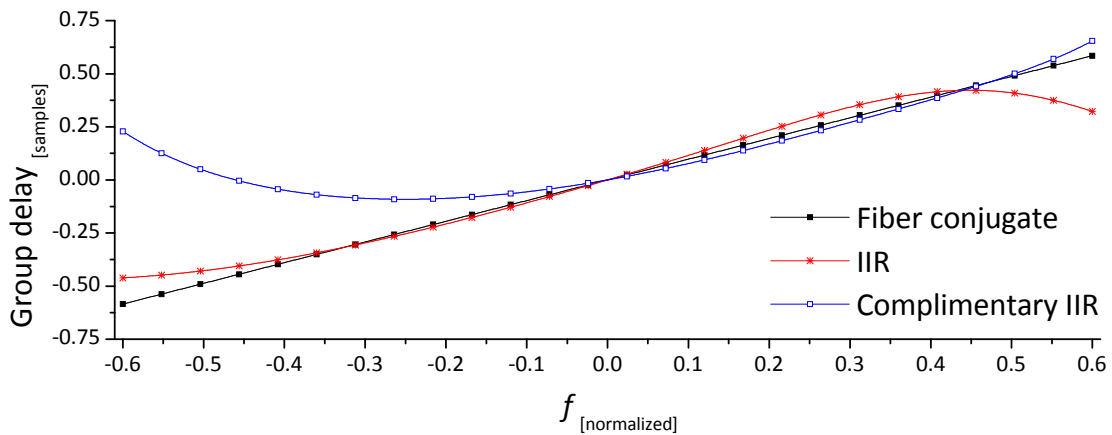


Figure 6-6: Desired and complex IIR filter group delays vs. normalized frequency

The eye diagrams for SSM/FFT, IIR and complimentary IIR are seen in Figure 6-7. The experimental dataset with  $P_L = 6dBm$ , and a total propagation of  $760km$  was used. From this figure, it is clear that the complimentary design is superior to the non-complimentary design; this performance is achieved at no computational load cost.

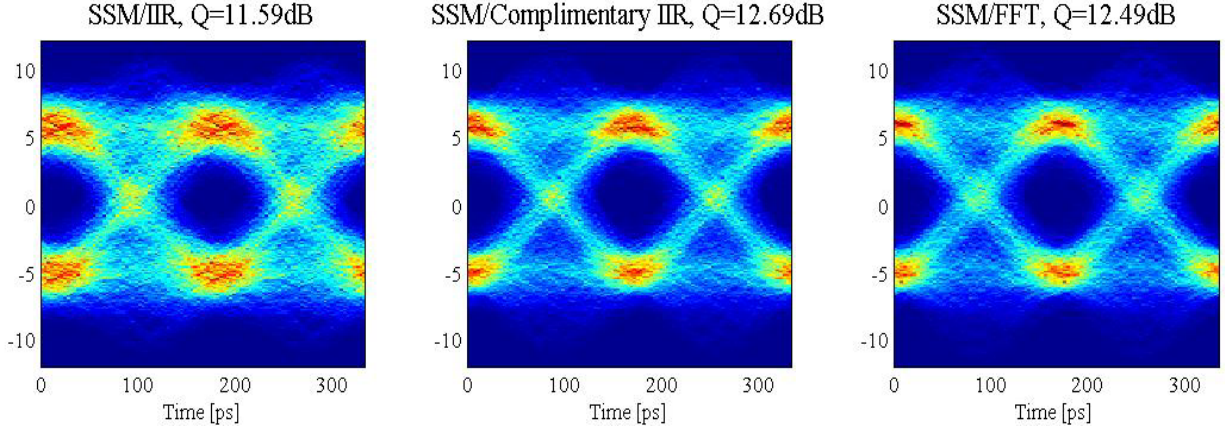


Figure 6-7: Eye diagrams for SSM using IIR, complimentary IIR and FFT

The decision-threshold Q-factors for SSM/FIR and SSM/IIR for both IIR and complimentary-IIR designs, as a function of transmission distance, are presented in Figure 6-8 for  $P_L = 6dBm$ . For comparison purposes, SSM/FFT in which dispersion compensation is done in the frequency domain), linear (dispersion compensation only, CDC) and lumped compensation are also presented. It is clearly seen that the complimentary-IIR design outperforms that of the non-complimentary one. As mentioned earlier, this comes at no computational cost and is hence the preferred solution.

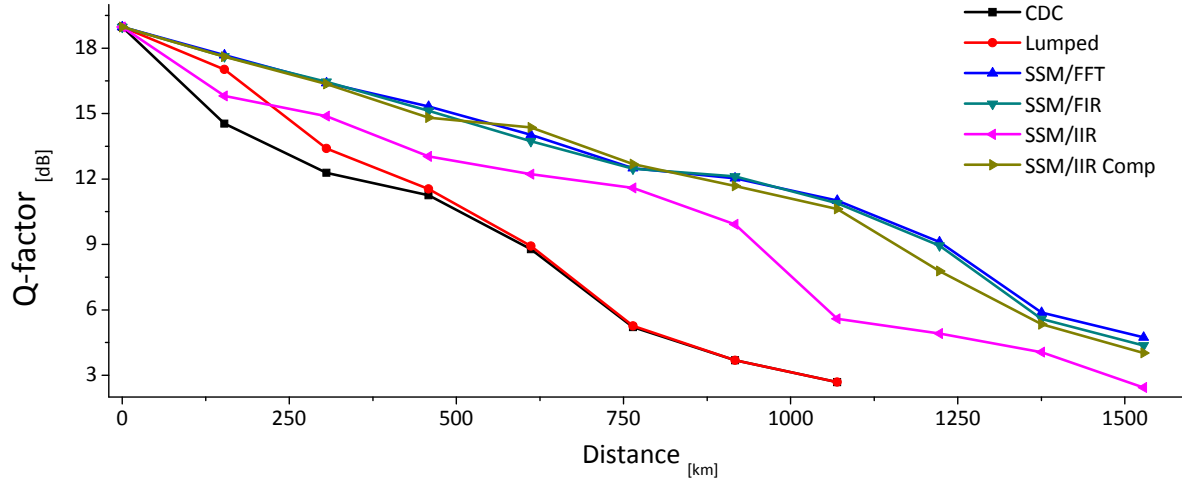


Figure 6-8: Q-factor vs. propagation distance after SSM using various compensation methods

### 6.5.1. Complex-IIR filtering Computational Load Reduction

The IIR filter is a second order (bi-quadratic) complex all-pass filter. 6 real multiplication and 12 real summation operations are required to realize this filter. This calculation accounts for both quadrature paths and common multiplication operations are lumped together. FIR filtering requires  $2(N_{FIR} + 1)$  multiplication and  $2(2N_{FIR} + 1)$  summation operations, where  $N_{FIR}$  is the number of (complex) FIR filter coefficients. FIR filter symmetry is taken into account, reducing the number of operations by a factor of approximately 2. In the case discussed here, 21 coefficients are required for FIR filtering, resulting in a factor of 7.3 in multiplication and 6.83 in number of summation operations compared to IIR filtering. This large difference in number of operations makes IIR filtering an extremely attractive approach in the realization of the SSM.

Although the use of IIR filtering is efficient, the feedback associated with the approach is problematic with respect to real-time implementation, whereas FIR filtering is real-time compatible [82]. Efficient FIR filtering with wavelet-based FIR filter design is presented next.



## 6.6. Wavelet-Based Split-Step Method for Backward-Propagation

Accurate backward-propagation of a multichannel optical signal requires the SSM step size to be small enough so that the assumption that dispersion and nonlinearity act independently is valid [80]. A major difficulty in implementing this technique is the high computational load associated with the dispersion operator. This operator can be implemented in the frequency-domain (via fast Fourier transform, FFT) or in the time-domain using filters. For real-time compatible implementation, FIR filtering is a practical choice as it does not require block-processing (as opposed to FFT implementation). Moreover, FIR filtering does not require a feedback path, as opposed to the use of infinite-impulse response filtering, which was shown to be highly efficient [83], but is hard to implement in real-time.

The FIR filter coefficients may be obtained by an inverse-Fourier transform (IFT) of a step's dispersion frequency response, given in Eq. 2a. This makes the filter length identical to the IFT length, which should be made long enough to achieve high accuracy of the SSM. To reduce the SSM computational load, time-domain windowing of the dispersion compensating FIR filter may be considered; e.g., using Tukey windowing [84]. The window width should be approximately on the order of the time-frame related to the dispersion-induced pulse spreading over a single step, given by:

$$N_{lin} = \frac{\Delta\lambda D z_{step}}{T_s} \quad (6-6)$$

where  $\Delta\lambda$ ,  $D$  and  $T_s$  are the optical bandwidth, dispersion parameter (in ps/km/nm) and the sampling interval, respectively. There is however, a fundamental issue associated with windowing of the FIR filter: the loss of the all-pass property of the dispersion operator. The all-

pass property means that the filter  $H_f(\omega)$  used for dispersion compensation (see Eq. (5-3)) should be lossless, i.e.  $|H_f(\omega)| = 1, \forall \omega$ . As multiple steps of dispersion compensation are required by the SSM, the accumulated error from the truncation of the FIR filter becomes significant and the ultimate quality of the backward-propagated signal is deteriorated. IFT-based design of the FIR dispersion compensation filter is sub-optimal since the Fourier transform relies on a harmonic decomposition basis which is not time-limited and windowing is hence required. Wavelet-based filter design of the dispersion operator is based on time-limited decomposition. This approach is shown achieve accurate back-propagation while reducing the number of operations required for the linear operator, as shown in the following.

### 6.6.1. Theory of Wavelet-Based Dispersion Compensation

Wavelets-based FIR filter design makes use of compact-support decomposition functions. Compact support functions are only non-zero on a finite interval, as opposed to the harmonic basis. As suggested in [85], a possible choice for the decomposition basis is the Deslaurier-Duruc interpolating function,  $\phi(t)$ . The function's support is determined by a single (odd) parameter,  $s$ . The compact-support property is stated as:  $\phi(t) \equiv 0, \forall |t| > sT_s$ . The interpolating function is defined by a filter whose coefficients are given by:

$$h_{2k} = \delta_k \tag{6-7}$$

$$h_{2k+1} = h_{-2k-1} = \frac{(-1)^{\frac{s+1}{2}-k} \prod_{q=0}^s \left(q - \frac{s}{2}\right)}{\left(\frac{s-1}{2} - k\right)! \left(\frac{s+1}{2} + k\right)! \left(k + \frac{1}{2}\right)} \tag{6-8}$$

where  $\delta_k$  is the Kroneker delta function. The compact support of  $\phi(t)$  dictates that  $h_k \equiv 0, \forall |k| > s$ .  $\phi(t)$  can be obtained from the coefficients  $h_k$  by using the cascade algorithm [86].

The parameter  $s$  is used to match the dispersion compensating filter length to the required dispersion-induced pulse spreading time-frame, from Eq. (6-6). Two interpolating functions for  $s = 5, 39$  are shown in Figure 6-9. The compact-support of  $\phi(t)$  is clearly seen in the inset with  $\phi(t)$  being identical to zero at times beyond  $|t| > sT_s$ .

The interpolating nature is evident from this plot, where the function is identically zero at all the sampling points except at  $t = 0$ . This function is reminiscent of the  $Sinc(t) = \frac{\sin(\pi t)}{\pi x}$  interpolating function classically used in digital-to-analog reconstruction of sampled signals through the Nyquist-Shannon sampling theorem. The major difference lies in the compact support of  $\phi(t)$ , as opposed to the  $Sinc(t)$  function having an infinite support on  $t \in (-\infty, \infty)$ . Also observed in Figure 6-9 is the wider support with increasing  $s$ , as expected from the design of the filter  $h$ ; the inset in Figure 6-9 shows  $\log\{|\phi(t)|\}$  to clarify this difference.

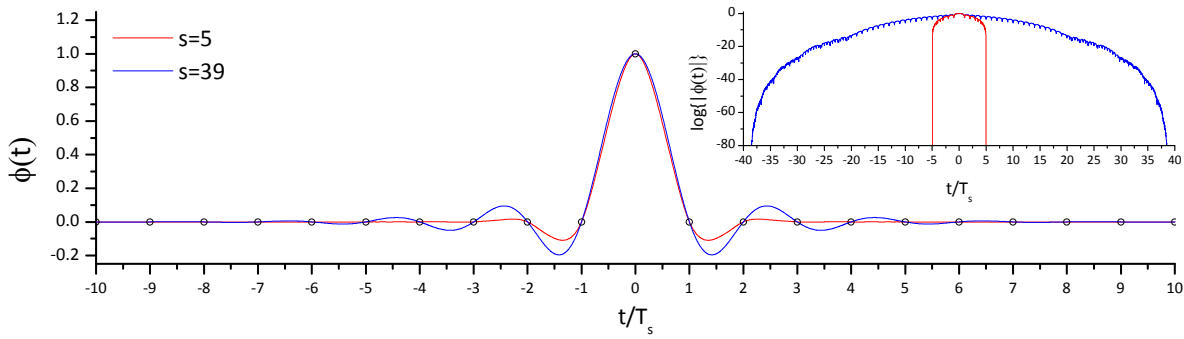


Figure 6-9: Wavelet interpolation function  $\phi(t)$  for  $s = 5, 39$

The linear operator requires finding the second and third order derivative of the time-shifted interpolation function  $\phi_m(t) = \phi(t - t_m)$ , where  $t_m$  are the sampling instances). To achieve this, vectors  $\mathbf{D}^{(\mu)}$  of  $2s - 1$  elements each are found by solving the linear set of equations defined in [87]. Keeping the same notation as in [85] ( $\mu = 2, 3$  for the second and third order derivative, respectively), the following set of equations is to be solved:

$$\sum_{k=-(s+1)/2}^{(s+1)/2} h_{2k+1} D_{2(k+n)+1}^{(\mu)} - 2^{-\mu} D_n^{(\mu)} + D_{2n}^{(\mu)} = 0 \quad (6-9)$$

$$\sum_{n=1-s}^{s-1} n^{\mu} D_n^{(\mu)} = \mu! \quad (6-10)$$

where  $n$  is an integer and Eq. (6-10) is used for normalization. The compact support limits the number of nonzero elements of  $\mathbf{D}^{(\mu)}$  so that  $D_n \equiv 0, \forall |n| \geq s$ . The elements of  $\mathbf{D}^{(\mu)}$  are symmetric for  $\mu = 2$  and anti-symmetric for  $\mu = 3$ , such that:  $D_{-k}^{(\mu)} = (-1)^{\mu} D_k^{(\mu)}$ , so that there are  $s$  equations required to obtain  $\mathbf{D}^{(\mu)}$ . The Wavelets-based FIR filter used for dispersion compensation is given by [87]:

$$\mathbf{h}_f = IFFT \left\{ \exp \left\{ \left\{ FFT \left[ \frac{1}{2T_s^2} \left( -j\beta_2 \mathbf{D}^{(2)} + \frac{\beta_3 \mathbf{D}^{(3)}}{3T_s} \right) \right] + \frac{\alpha}{2} \right\} \right\} \right\} \quad (6-11)$$

In order for  $\mathbf{h}_f$  to obtain high accuracy,  $\mathbf{D}^{(2,3)}$  are zero-padded (before the Fourier-Transform) so that the impulse response is longer than the limit given by Eq. (6-6).  $\mathbf{h}_f$  is then truncated to allow savings in number of operations by setting all the coefficients that result in  $\log\{|h_f|\} < \epsilon$  to zero.  $\epsilon$  may be scanned to obtain a value which allows good performance while minimizing the number of non-zero  $\mathbf{h}_f$  coefficients.

### 6.6.2. Numerical Simulation and Results

To investigate the benefit of wavelets-based FIR filter design, simulation of a 9 channel WDM system was performed. Quadrature phase-shift keying (QPSK) modulation at 10GBaud, with 20GHz channel spacing was employed. The simulation sampling rate used was set to 320GHz ( $T_s = 3.125ps$ ) and Pseudo-random bit sequence of order 23 was used. The optical

signal was launched into 48 spans of 100km NZ-DSF. The fiber parameters are  $\alpha = 0.2 \frac{dB}{km}$ ,  $D = 4 \frac{ps}{km \cdot nm}$ ,  $D_s = 0.045 \frac{ps}{km \cdot nm^2}$  and  $\gamma = 1.46 \frac{1}{W \cdot km}$ , where  $D_s$  is the dispersion slope. The loss in each span was compensated using an optical amplifier with noise figure  $N_F = 5$ .

Verification of the benefit of using backward-propagation as compared to linear (dispersion) compensation only is seen in Figure 6-10. The total launching power is scanned to demonstrate the ability to achieve better performance using backward-propagation, compared to linear compensation only. Backward-propagation is implemented as discussed in Section 6.2, with frequency domain dispersion compensation (SSM/FFT). Using frequency domain compensation no time-domain effects (such as FIR windowing) deteriorate the performance. SSM/FFT is hence used as the benchmark for backward-propagation performance. Also included is the performance limit when all the fiber parameters except loss are set to zero; in this case, only amplifier noise and linear interference affect performance. The phase standard-deviation (Phase-STD) serves as a metric for the performance since phase shift keying is considered in this numerical study. From Figure 6-10, the benefit of using backward-propagation is clear as the optimal launching power is increased and the performance improved. The optimum total launching power is found to be 5dBm and an SSM step size of 2km was determined to achieve close to zero penalty performance, compared to smaller step sizes. These values will be used in the following analysis.

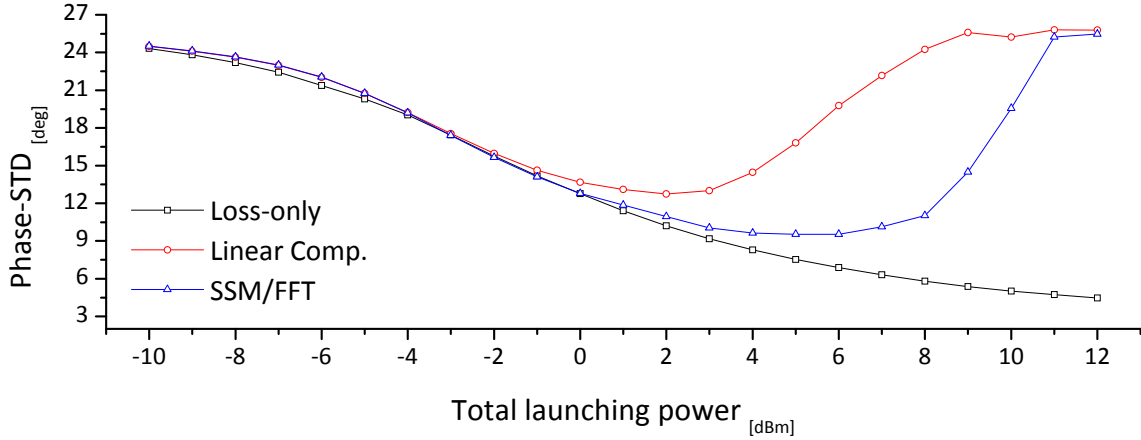


Figure 6-10: Phase standard deviation vs. total launching power

A comparison of three FIR filters using IFT, IFT with Tukey windowing (both in frequency and time, as in [84]) and wavelets-based design is seen in Figure 6-11. On the right, the time-domain magnitude, namely the impulse response is plotted on a logarithmic scale for clarity. The plot reveals the slow decay of the IFT filter; Tukey windowing limits the extent (and hence the number of operations required for filtering) of the IFT-based filter. Wavelets-based design achieves the tightest windowing limits due to the compact-support of the decomposition function it is based upon. Moreover, observing the magnitude response comparison between IFT/Tukey and wavelets-based designs (Figure 6-11, top right) shows that the all-pass characteristic of the wavelets-based filter is preserved much better than with the IFT/Tukey design. Although the IFT/Tukey filter group-delay (Figure 6-11, bottom right) is more accurate (namely, closer to the required linear group-delay response) at the band edges than the wavelets-based filter, loss of the all-pass feature combined with multiple linear-compensation operations required when employing the SSM is a significantly more severe issue.

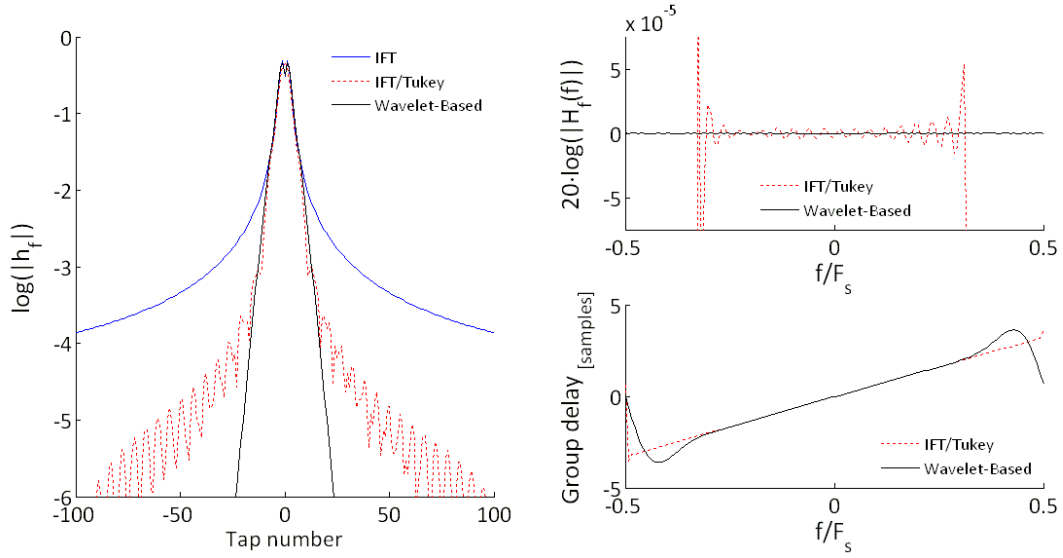


Figure 6-11: Impulse response of dispersion compensation FIR filter with IFT, IFT/Tukey and Wavelets-based designs (left), magnitude response (top right) and group-delay response (bottom right).

The number of FIR filter coefficients for IFT/Tukey was scanned by varying the Tukey window ratios of both frequency and time windows used. For the wavelets-based filter, the parameter  $s$  was scanned increasingly by taking values starting from  $N_{lin}$  given in Eq. (6-6) (with the parameter  $= -12$ ) to find the smallest limit on  $s$  which allows a wide enough window to include the effect of dispersion-induced pulse spreading. A value of  $s = 27$  was found to be sufficient. Truncation of the wavelets-based FIR filter by increasing the value of  $\epsilon$  minimizes the number of operations required for the linear operator in the SSM. A performance comparison of the two filter designs is shown in Figure 6-12. The performance limit of the SSM achieved with the linear operator implemented in the frequency domain (FFT) is also shown.

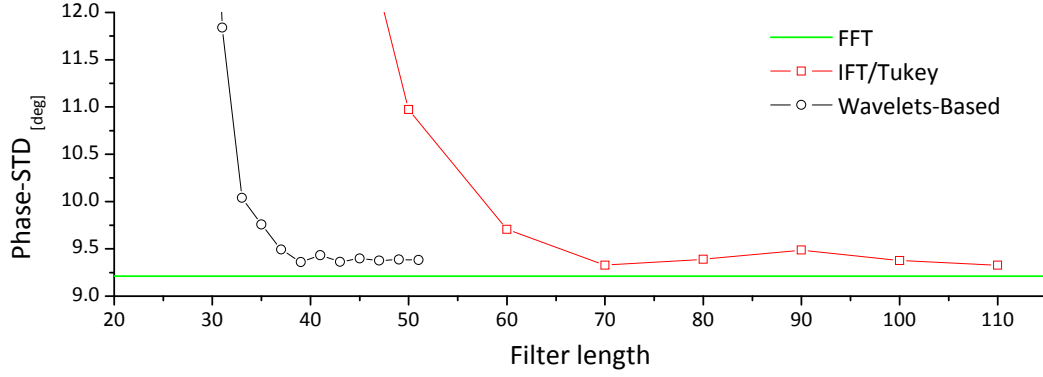


Figure 6-12: Performance comparison of IFT/Tukey and wavelets-based FIR filter design vs. filter length.

From Figure 6-12 it is observed that the wavelets-based FIR filtering approach does indeed achieve equivalent performance as the IFT/Tukey design (both being close to the frequency-domain linear compensation implementation). The wavelets-based filter achieves this performance using 39 taps, as opposed to 70 taps for the IFT/Tukey design. The number of operations required for the SSM linear operator is hence reduced by a factor of approximately 1.8, validating the wavelets-based approach to dispersion-compensation FIR filter design.

## 6.7. Conclusions

In this chapter the viability of using the SSM was presented. A 3-channel *6GBaud* BPSK OWDM recirculating loop experiment was carried out and backward-propagation was achieved using the SSM with FFT (frequency-domain compensation), FIR, IIR, complimentary-IIR and wavelet-based FIR filtering schemes (time-domain compensation). Experimental results demonstrate that the propagation distance (limited by forward error correction) can be significantly extended compared to CDC only or lumped CDC and nonlinearity compensation.

The SSM step-size requirements were introduced and an analysis of the experimental results demonstrated the fact that higher launching powers are harder to compensate for. This is due to nonlinear products which might not be available for digital backward-propagation due



to the limited analog bandwidth at the receiver and the signal-ASE nonlinear beat which is stronger with higher optical powers. It is determined that an optimal launch power is required for a given transmission distance. This is in opposition with a linear channel where a larger launching power naturally translates to an extended reach.

The high implementation complexity of the SSM was addressed by introducing two alternative approaches to the implementation of the linear operator. The first was a complex-coefficients complementary-IIR filtering design which achieves a factor of 7.3 in number of multiplication and 6.8 in number of summation operations, compared to FIR filtering approach based on inverse Fourier transform design. The large computational savings make this approach highly attractive when considering implementation of SSM for backward propagation.

Since IIR filtering requires a feedback path which is not highly compatible with real-time implementation at exceedingly fast clock speeds, a wavelet-based FIR filter design was introduced. The compact support allowed by wavelets (through the use of a proper interpolating function) translates to rapid decay of the FIR filter coefficients used for dispersion compensation. Simulations results reveal that savings of a factor approximately 1.8 is achievable.

## CHAPTER 7. SUMMARY AND FUTURE RESEARCH DIRECTIONS

This dissertation focused on various aspects of coherent detection with subsequent DSP techniques used for channel impairment compensation and signal demodulation. Theoretical, numerical and experimental results were all obtained to gain further the knowledge and provide design and implementation guidelines when this detection architecture is considered.

As a first effort in coherent detection, the benefit of using coherent detection with a phase-coded Duobinary signal in the presence of fiber dispersion was presented. It was found that coherent detection extends the transmission distance (using and eye closure penalty of  $1dB$ ) from approximately  $213km$  to  $283km$ . A decision-directed phase-locked loop compatible with this type of modulation was also presented.

Delving into the coherent/DSP arena, an analytical approximation of the performance of a generic feed-forward carrier phase estimation scheme provided insight to the tradeoff between additive noise and phase noise. The additive noise requires filtering which introduces an error on the phase tracking. This is due to the fact that phase estimation on a current symbol is affected by other symbols through filtering. An optimal block size ( $N_b$ ) in the presence of both noise sources was derived. An optimal block size exists because phase noise can be ideally removed when a single symbol is considered ( $N_b = 1$ ) while additive noise is ideally filtered with  $N_b \rightarrow \infty$ . The phenomenon of cycle-slipping in feed-forward phase estimation schemes was also investigated. The conditions for an occurrence of a cycle-slip were established. It was found that for  $N_b = 1$ , a cycle slip occurs when the phase estimate in the presence of both additive and phase noises deviates by more than  $\pi$  from the would-be estimate in the absence of additive noise. The probability-density functions required for cycle-slip probability calculation

were derived, with the associated regions of integration. Excellent agreement was found between Monte-Carlo simulation and the derived cycle-slip analytical expression.

One of the benefits most quoted with respect to coherent detection is the high spectral-efficiency. This may be achieved by filtering in the electrical/digital domain, rather than the optical domain. Optical filters are hard to design and implement and do not have as high Q-factors as RF/digital filters, leading to linear spectral crosstalk between WDM channels. The concept of orthogonal-WDM was presented and experimentally demonstrated. By allowing the transmitter and receiver pulse shapes to fulfill certain conditions (namely that their combined shape is a Nyquist filter) and by spacing the WDM channels at the symbol rate, it was shown that the received signal can be demodulated with a penalty of approximately  $2.8dB$ . This result demonstrates the benefit of coherent/DSP approach with respect to spectral efficiency as the ultimate spectral-efficiency limit for the binary phase-shift keying single-polarization modulation format  $\left(1 \frac{bits}{s \cdot Hz}\right)$  has been achieved.

Transmission in the linear regime (with low total optical powers) avoids degrading nonlinear effects, yet dispersion compensation must still be considered. In the digital domain finite-impulse-response (FIR) filtering can be used for this purpose. However, infinite-impulse response filters are more efficient since these incorporate a feed-back path. Real-coefficients IIR filters for chromatic dispersion compensation were suggested in this dissertation. It was shown that these may achieve savings of close to 1.7 in number of operations required for dispersion compensation compared to FIR filters. The reason for the limited savings in computational load is that there is a large overhead at short transmission distances. This

overhead stems from the stability conditions of the real-coefficients all-pass IIR filters, which must have a monotonously decreasing phase response. A time-reversal scheme combined with Hilbert filtering was suggested as a solution to the stability problem. The added complexity associated with real, all-pass IIR filtering for dispersion compensation is to be considered as a tradeoff with the savings in number of operations.

Complex-IIR filters were also introduced. These filters do not have the same stability constraints, yet are limited by the total amount of dispersion (per filter order) which can be compensated for. A useful application for these filters is when the total amount of dispersion is small, namely when the split-step method (SSM) is employed.

Backward-propagation was experimentally demonstrated using the SSM to combat the combined effect of fiber dispersion and nonlinearity. The SSM was used in several different configurations to experimentally demonstrate the advantage of this approach, compared to linear and lumped compensation. An orthogonal-WDM transmission system using a recirculating loop was set-up and non-zero dispersion shifted fiber used. This system configuration manifests a large amount of nonlinear effects, since both small channel spacing and low dispersion contribute heavily to the accumulation of nonlinear effects. It was shown that even under these operating conditions the SSM may substantially extend the transmission reach; e.g., for a decision-threshold Q-factor of  $10\text{dB}$ , a 3 channel with  $6\text{GBaud}$  signaling rate,  $7\text{GHz}$  channel spacing and a total launch power of  $6\text{dBm}$ , the transmission reach more than doubled using the SSM versus linear or lumped compensation.

To achieve higher computational efficiency, complex-coefficients IIR filtering was suggested in conjunction with the symmetric-SSM. The symmetric-SSM allows complimentary

design of the IIR filters used for the two propagation steps required for dispersion compensation. The complimentary-IIR performance is practically equivalent to the SSM with dispersion compensated in the frequency domain (through a Fourier-transform) or in the time domain using FIR filters. The savings in number of operations was found to be approximately 7, compared for FIR filtering implementation.

IIR filtering requires a feedback-path which introduces a considerable real-time implementation difficulty. As an alternative, wavelet-based FIR filter design was suggested. The wavelet compact time support dictates that the FIR filter can be truncated without a significant effect on the all-pass property, as opposed to inverse-Fourier based designs. It was shown through numerical simulations that a factor of approximately 1.8 in computational load savings can be achieved while maintaining similar performance using wavelet-based design.

The novel coherent/DSP approach presents new challenges and opens the door to many possible research directions. Some of the challenges facing academia and industry in this context are discussed henceforth.

From an implementation perspective, real-time operation is a critical issue. The algorithms used for channel impairment compensation and demodulation must consider real-time compatibility, under clock speed constraints. In that sense, feedback paths should be avoided unless DSP speeds advance at a pace which allows operation without resorting to look-ahead techniques [82]. Look-ahead design may render the use of feedback structures inefficient compared to their feed-forward only counterparts. Most of the coherent/DSP demonstrations are based on offline processing; however, first attempts have already been made to implement this type of receivers in real-time. Field-programmable gated array implementations are

presented in [88, 89] and an application-specific integrated-circuit was also demonstrated [33]. Improved and efficient algorithms to handle channel impairment compensation, polarization and phase tracking and any other task required for demodulation are and will be sought after, far into the future.

One of the more fascinating possibilities of the use of DSP is the ability to pre- or post-compensate for both linear and nonlinear channel impairments [12, 13]. This technique allows an increase of several dBm in launching power, which translates to significantly improved performance, compared to linear compensation only [90]. However, numerous repetitions of linear and nonlinear operations are required. This poses a great implementation challenge since power consumption, hardware complexity and latency are all at a premium. Moreover, the entire bandwidth which plays a role in the dispersion-nonlinearity interaction must be handled in parallel. The amount of operations required for a realistic system might be prohibitive. In [90] the impact of XPM and FWM compensation is studied. It was found that when the performance degradation is dominated by XPM, simplified equations for backward-propagation may be considered and hence the amount of operations required for (quasi-)compensation of fiber impairments reduces dramatically. In the future, various scenarios must be explored, where it is envisioned that with a proper WDM system design, a significant benefit from backward-propagation can be obtained with tolerable amount of required digital operations.

Another major issue when considering backward-propagation of a WDM optical signal is polarization-mode dispersion (PMD). The treatment presented in this dissertation focused on single polarization which simplified the relevant equations to their scalar form. When polarization is considered (as would be the case when polarization multiplexing is to be

implemented), PMD presents a concern. The interaction between nonlinearity and PMD requires knowledge of the state of polarization along the propagation for backward-propagation to be employed. This translates to monitoring the polarization state as a function of wavelength in multiple locations along the link, since PMD is wavelength dependent [91]. A rigorous study of this problem must be conducted in order to realistically consider polarization-multiplexed signals in a WDM configuration with vectorial backward-propagation implemented.

Assuming infinite resources to compensate for any deterministic effect in nonlinear fiber, there still remain the fundamental question of information capacity limit of such systems. In his pioneering work, Shannon paved the way to answering this question for a linear medium by introducing the fundamentals of information theory [7]. Shannon's formula is given for a linear channel, where the noise is un-correlated with the signal. In a nonlinear fiber link, this is not the case as there is interaction between the signal and amplified spontaneous emission noise as the transmitted field propagates. Several research papers suggest calculation of the limit through various methods (e.g., [92-94]), for various modulation formats, receiver architectures and fiber types. The different models and assumptions lead to quantitatively different conclusions. A fundamental study of the information limit is still to be conducted for the case where backward-propagation is considered and for which only non-deterministic effects stemming (mostly) from nonlinear ASE-signal beat exist.

The topics presented above are but several of multiple challenges associated with coherent detection/DSP facing the optical fiber communication community today.

## REFERENCES

- [1] G. P. Agrawal, *Fiber-Optic Communication Systems*, 3rd ed. New York: Wiley, 2002.
- [2] T. H. Maiman, "Stimulated Optical Radiation in Ruby," *Nature*, vol. 187, pp. 493-494, 1960.
- [3] K. C. Kao and G. A. Hockham, "Dielectric Fibre Surface Waveguides for Optical Frequencies," in *Proc. Inst. Elec. Eng.*, 113, 1966.
- [4] H. Kogelnik, "High-capacity optical communications: personal recollections," *Selected Topics in Quantum Electronics, IEEE Journal of*, vol. 6, pp. 1279-1286, 2000.
- [5] R. A. Linke and A. H. Gnauck, "High-capacity coherent lightwave systems," *Lightwave Technology, Journal of*, vol. 6, pp. 1750-1769, 1988.
- [6] D. N. Payne and R. I. Laming, "Optical amplifiers-a telecommunications revolution," 1991, pp. 3-4.
- [7] C. E. Shannon, "A Mathematical Theory of Communication," *The Bell System Technical Journal*, vol. 27, pp. 379-423, 623-656, Jul. and Oct. 1948.
- [8] E. Ip, A. P. T. Lau, D. J. F. Barros, and J. M. Kahn, "Coherent detection in optical fiber systems," *Opt. Express*, vol. 16, pp. 753-791, 2008.
- [9] L. G. Kazovsky, "Phase- and polarization-diversity coherent optical techniques," *Lightwave Technology, Journal of*, vol. 7, pp. 279-292, 1989.
- [10] J. Salz, "Modulation and detection for coherent lightwave communications," *Communications Magazine, IEEE*, vol. 24, pp. 38-49, 1986.



- [11] K. Kikuchi, T. Okoshi, M. Nagamatsu, and N. Henmi, "Degradation of bit-error rate in coherent optical communications due to spectral spread of the transmitter and the local oscillator," *Lightwave Technology, Journal of*, vol. 2, pp. 1024-1033, 1984.
- [12] K. Roberts, L. Chuandong, L. Strawczynski, M. O'Sullivan, and I. Hardcastle, "Electronic precompensation of optical nonlinearity," *Photonics Technology Letters, IEEE*, vol. 18, pp. 403-405, 2006.
- [13] X. Li, X. Chen, G. Goldfarb, E. Mateo, I. Kim, F. Yaman, and G. Li, "Electronic post-compensation of WDM transmission impairments using coherent detection and digital signal processing," *Opt. Express*, vol. 16, pp. 880-888, 2008.
- [14] R. Noé, "PLL-free synchronous QPSK polarization multiplex/diversity receiver concept with digital I&Q baseband processing," *Photonics Technology Letters, IEEE*, vol. 17, pp. 887-889, 2005.
- [15] S. J. Savory, G. Gavioli, R. I. Killey, and P. Bayvel, "Electronic compensation of chromatic dispersion using a digital coherent receiver," *Opt. Express*, vol. 15, pp. 2120-2126, 2007.
- [16] D.-S. Ly-Gagnon, S. Tsukamoto, K. Katoh, and K. Kikuchi, "Coherent Detection of Optical Quadrature Phase-Shift Keying Signals With Carrier Phase Estimation," *J. Lightwave Technol.*, vol. 24, p. 12, 2006.
- [17] K. Kikuchi, "Phase-diversity homodyne detection of multilevel optical modulation with digital carrier phase estimation," *Selected Topics in Quantum Electronics, IEEE Journal of*, vol. 12, pp. 563-570, 2006.

- [18] G. Goldfarb, M. G. Taylor, and G. Li, "Experimental Demonstration of Fiber Impairment Compensation Using the Split-Step Finite-Impulse-Response Filtering Method," *Photonics Technology Letters, IEEE*, vol. 20, pp. 1887-1889, 2008.
- [19] A. Viterbi, "Nonlinear estimation of PSK-modulated carrier phase with application to burst digital transmission," *Information Theory, IEEE Transactions on*, vol. 29, pp. 543-551, 1983.
- [20] Y. Yamamoto and T. Kimura, "Coherent optical fiber transmission systems," *Quantum Electronics, IEEE Journal of*, vol. 17, pp. 919-935, 1981.
- [21] T. Okoshi, "Recent progress in heterodyne/coherent optical-fiber communications," *Lightwave Technology, Journal of*, vol. 2, pp. 341-346, 1984.
- [22] S. Betti, G. D. Marchis, and E. Iannone, *Coherent optical communications systems*. New York: Wiley, 1995.
- [23] E. J. Bachus, T. Almeida, P. Demeester, G. Depovere, A. Ebberg, M. Rui Ferreira, K. Giok-Djan, O. Koning, R. Marsden, J. Rawsthorne, and N. Wauters, "Coherent optical systems implemented for business traffic routing and access: the RACE COBRA project," *Lightwave Technology, Journal of*, vol. 14, pp. 1309-1319, 1996.
- [24] R. J. v. d. Plassche, *CMOS Integrated Analog-to-digital and Digital-to-analog Converters*, 2nd ed. ed. Boston: Kluwer Academic Publishers, 2003.
- [25] M. G. Taylor, "Coherent detection method using DSP for demodulation of signal and subsequent equalization of propagation impairments," *Photonics Technology Letters, IEEE*, vol. 16, pp. 674-676, 2004.

- [26] R. Noé, "Phase noise tolerant synchronous QPSK receiver concept with digital I&Q baseband processing," in *Opto-Electronics and Communications Conference (OECC)*, Yokohama, Japan, 2004.
- [27] F. Derr, "Coherent optical QPSK intradyne system: concept and digital receiver realization," *Lightwave Technology, Journal of*, vol. 10, pp. 1290-1296, 1992.
- [28] D. S. Ly-Gagnon, K. Katoh, and K. Kikuchi, "Coherent demodulation of differential 8-phase-shift keying with optical phase diversity and digital signal processing," in *Lasers and Electro-Optics Society, 2004. LEOS 2004. The 17th Annual Meeting of the IEEE*, 2004, pp. 607-608 Vol.2.
- [29] D. S. Ly-Gagnon, K. Katoh, and K. Kikuchi, "Unrepeated optical transmission of 20 Gbit/s quadrature phase-shift keying signals over 210 km using homodyne phase-diversity receiver and digital signal processing," *Electronics Letters*, vol. 41, pp. 206-207, 2005.
- [30] G. Charlet, N. Maaref, J. Renaudier, H. Mardoyan, P. Tran, and S. Bigo, "Transmission of 40Gb/s QPSK with Coherent Detection over Ultra-Long Distance Improved by Nonlinearity Mitigation," in *European Conference on Optical Communication*, Cannes, Frances, 2006.
- [31] T. Pfau, S. Hoffmann, R. Peveling, S. Bhandare, S. K. Ibrahim, O. Adamczyk, M. Porrmann, R. Noe, and Y. Achiam, "First Real-Time Data Recovery for Synchronous QPSK Transmission With Standard DFB Lasers," *Photonics Technology Letters, IEEE*, vol. 18, pp. 1907-1909, 2006.

- [32] G. Goldfarb, G. Li, and M. G. Taylor, "Orthogonal Wavelength-Division Multiplexing Using Coherent Detection," *Photonics Technology Letters, IEEE*, vol. 19, pp. 2015-2017, 2007.
- [33] H. Sun, K.-T. Wu, and K. Roberts, "Real-time measurements of a 40 Gb/s coherent system," *Opt. Express*, vol. 16, pp. 873-879, 2008.
- [34] G. Goldfarb and G. Li, "Chromatic Dispersion Compensation Using Digital IIR Filtering With Coherent Detection," *Photonics Technology Letters, IEEE*, vol. 19, pp. 969-971, 2007.
- [35] M. G. Taylor, "Compact Digital Dispersion Compensation Algorithms," in *OFC/NFOEC*, San Diego, CA, 2008, p. OTuO1.
- [36] R. I. Killey, P. M. Watts, V. Mikhailov, M. Glick, and P. Bayvel, "Electronic dispersion compensation by signal predistortion using digital Processing and a dual-drive Mach-Zehnder Modulator," *Photonics Technology Letters, IEEE*, vol. 17, pp. 714-716, 2005.
- [37] A. Leven, N. Kaneda, K. Ut-Va, and C. Young-Kai, "Coherent Receivers for Practical Optical Communication Systems," in *Optical Fiber Communication and the National Fiber Optic Engineers Conference, 2007. OFC/NFOEC 2007. Conference on*, 2007, pp. 1-3.
- [38] S. Ryu, S. Yamamoto, H. Taga, N. Edagawa, Y. Yoshida, and H. Wakabayashi, "Long-haul coherent optical fiber communication systems using optical amplifiers," *Lightwave Technology, Journal of*, vol. 9, pp. 251-260, 1991.
- [39] J. R. Barry and E. A. Lee, "Performance of coherent optical receivers," *Proceedings of the IEEE*, vol. 78, pp. 1369-1394, 1990.

- [40] E. Ip and J. M. Kahn, "Carrier Synchronization for 3-and 4-bit-per-Symbol Optical Transmission," *J. Lightwave Technol.*, vol. 23, p. 4110, 2005.
- [41] C. Henry, "Theory of the phase noise and power spectrum of a single mode injection laser," *Quantum Electronics, IEEE Journal of*, vol. 19, pp. 1391-1397, 1983.
- [42] S. J. Savory, "Digital filters for coherent optical receivers," *Opt. Express*, vol. 16, pp. 804-817, 2008.
- [43] E. Ip and J. M. Kahn, "Digital Equalization of Chromatic Dispersion and Polarization Mode Dispersion," *Lightwave Technology, Journal of*, vol. 25, pp. 2033-2043, 2007.
- [44] G. Goldfarb, K. Cheolhwan, and L. Guifang, "Improved chromatic dispersion tolerance for optical duobinary transmission using coherent detection," *Photonics Technology Letters, IEEE*, vol. 18, pp. 517-519, 2006.
- [45] G. Goldfarb and G. Li, "BER estimation of QPSK homodyne detection with carrier phase estimation using digital signal processing," *Opt. Express*, vol. 14, pp. 8043-8053, 2006.
- [46] J. H. Winters and R. D. Gitlin, "Electrical signal processing techniques in long-haul fiber-optic systems," *Communications, IEEE Transactions on*, vol. 38, pp. 1439-1453, 1990.
- [47] S. Watanabe and M. Shirasaki, "Exact compensation for both chromatic dispersion and Kerr effect in a transmission fiber using optical phase conjugation," *Lightwave Technology, Journal of*, vol. 14, pp. 243-248, 1996.
- [48] K. Yonenaga, S. Kuwano, S. Norimatsu, and N. Shibata, "Optical duobinary transmission system with no receiver sensitivity degradation," *Electronics Letters*, vol. 31, pp. 302-304, 1995.

- [49] D. Penninckx, M. Chbat, L. Pierre, and J. P. Thiery, "The phase-shaped binary transmission (PSBT): a new technique to transmit far beyond the chromatic dispersion limit," *Photonics Technology Letters, IEEE*, vol. 9, pp. 259-261, 1997.
- [50] K. Yonenaga and S. Kuwano, "Dispersion-tolerant optical transmission system using duobinary transmitter and binary receiver," *Lightwave Technology, Journal of*, vol. 15, pp. 1530-1537, 1997.
- [51] T. Ono, Y. Yano, and K. Fukuchi, "Demonstration of high-dispersion tolerance of 20-Gbit/s optical duobinary signal generated by a low-pass filtering method," in *Optical Fiber Communication. OFC 97., Conference on*, 1997, pp. 268-269.
- [52] T. Ono, Y. Yano, K. Fukuchi, T. Ito, H. Yamazaki, M. Yamaguchi, and K. Emura, "Characteristics of optical duobinary signals in terabit/s capacity, high-spectral efficiency WDM systems," *Lightwave Technology, Journal of*, vol. 16, pp. 788-797, 1998.
- [53] M. Shtaif and A. H. Gnauck, "The relation between optical duobinary modulation and spectral efficiency in WDM systems," *Photonics Technology Letters, IEEE*, vol. 11, pp. 712-714, 1999.
- [54] J. G. Proakis, *Digital Communications*, 4th ed. New York, NY: McGraw-Hill, 2001.
- [55] L. G. Kazovsky, S. Benedetto, and A. E. Willner, *Optical Fiber Communication Systems*. Boston, MA: Artech House, 1996.
- [56] M. G. Taylor, "Accurate digital phase estimation process for coherent detection using a parallel digital processor," in *Optical Communication, 2005. ECOC 2005. 31st European Conference on*, 2005, pp. 263-264 vol.2.

- [57] M. K. Simon, "On the bit-error probability of differentially encoded QPSK and offset QPSK in the presence of carrier synchronization," *Communications, IEEE Transactions on*, vol. 54, pp. 806-812, 2006.
- [58] Y. K. Some and P. Y. Kam, "Bit-error probability of QPSK with noisy phase reference," *Communications, IEE Proceedings-*, vol. 142, pp. 292-296, 1995.
- [59] A. H. Gnauck and P. J. Winzer, "Optical phase-shift-keyed transmission," *Lightwave Technology, Journal of*, vol. 23, pp. 115-130, 2005.
- [60] M. P. Fitz, "Equivocation in nonlinear digital carrier synchronizers," *Communications, IEEE Transactions on*, vol. 39, pp. 1672-1682, 1991.
- [61] H. Meyr, M. Moeneclaey, and S. Fechtel, *Digital Communication Receivers: Synchronization, Channel Estimation, and Signal Processing*: John Wiley & Sons, Inc., 1997.
- [62] G. De Jonghe and M. Moeneclaey, "The effect of the averaging filter on the cycle slipping of NDA feedforward carrier synchronizers for MPSK," in *Communications, 1992. ICC 92, Conference record, SUPERCOMM/ICC '92, Discovering a New World of Communications. IEEE International Conference on*, 1992, pp. 365-369 vol.1.
- [63] G. De Jonghe and M. Moeneclaey, "Cycle-slip analysis of the Mth-power NDA feedforward carrier synchronizer for MPSK," *Communications, IEEE Transactions on*, vol. 46, pp. 1000-1002, 1998.
- [64] M. K. Simon, *Probability Distributions Involving Gaussian Random Variables: A Handbook for Engineers, Scientists and Mathematicians*. New York, NY: Springer-Verlag, 2006.

- [65] S.-Y. Kim and K. Kikuchi, "1,000-km transmission of 20-Gbit/s QPSK-NRZ co-polarized DWDM signals with spectral efficiency of 1 bit/s/Hz using coherent detection," in *Optical Fiber Communication and the National Fiber Optic Engineers Conference, 2007. OFC/NFOEC 2007. Conference on*, 2007, pp. 1-3.
- [66] N. E. Jolley, H. Kee, P. Pickard, J. Tang, and K. Cordina, "Generation and propagation of a 1550 nm 10 Gbit/s optical orthogonal frequency division multiplexed signal over 1000m of multimode fibre using a directly modulated DFB," in *Optical Fiber Communication Conference, 2005. Technical Digest. OFC/NFOEC, 2005*, p. 3 pp. Vol. 6.
- [67] A. J. Lowery, D. Liang, and J. Armstrong, "Orthogonal Frequency Division Multiplexing for Adaptive Dispersion Compensation in Long Haul WDM Systems," in *Optical Fiber Communication Conference, 2006 and the 2006 National Fiber Optic Engineers Conference. OFC 2006*, 2006, pp. 1-3.
- [68] W. Shieh, X. Yi, and Y. Tang, "Transmission experiment of multi-gigabit coherent optical OFDM systems over 1000[emsp4 1/4-em space]km SSMF fibre," *Electronics Letters*, vol. 43, pp. 183-185, 2007.
- [69] J. H. Winters, "Equalization in coherent lightwave systems using a fractionally spaced equalizer," *Lightwave Technology, Journal of*, vol. 8, pp. 1487-1491, 1990.
- [70] P. P. Vaidyanathan, *Multirate Systems And Filter Banks*, 1st ed. Englewood Cliffs, NJ: Prentice-Hall, 1993.
- [71] C. C. Tseng, "Design of IIR digital all-pass filters using least pth phase error criterion," *Circuits and Systems II: Analog and Digital Signal Processing, IEEE Transactions on* [see



- also *Circuits and Systems II: Express Briefs, IEEE Transactions on*], vol. 50, pp. 653-656, 2003.
- [72] S. R. Powell and P. M. Chau, "A technique for realizing linear phase IIR filters," *Signal Processing, IEEE Transactions on [see also Acoustics, Speech, and Signal Processing, IEEE Transactions on]*, vol. 39, pp. 2425-2435, 1991.
  - [73] A. Carena, V. Curri, R. Gaudino, P. A. P. P. Poggiolini, and S. A. B. S. Benedetto, "A time-domain optical transmission system simulation package accounting for nonlinear and polarization-related effects in fiber," *Selected Areas in Communications, IEEE Journal on*, vol. 15, pp. 751-765, 1997.
  - [74] A. Yariv, D. Fekete, and D. M. Pepper, "Compensation for channel dispersion by nonlinear optical phase conjugation," *Opt. Lett.*, vol. 4, pp. 52-54, 1979.
  - [75] R. A. Fisher, B. R. Suydam, and D. Yevick, "Optical phase conjugation for time-domain undoing of dispersive self-phase-modulation effects," *TIME (psec)*, vol. 8, pp. 0-4.
  - [76] C. Pare, A. Villeneuve, P. A. Belanger, and N. J. Doran, "Compensating for dispersion and the nonlinear Kerr effect without phase conjugation," *Opt. Lett.*, vol. 21, p. 459, 1996.
  - [77] R.-J. Essiambre, P. J. Winzer, X. Q. Wang, W. Lee, C. A. White, and E. C. Burrows, "Electronic predistortion and fiber nonlinearity," *Photonics Technology Letters, IEEE*, vol. 18, pp. 1804-1806, 2006.
  - [78] E. Yamazaki, F. Inuzuka, K. Yonenaga, A. Takada, and M. Koga, "Compensation of Interchannel Crosstalk Induced by Optical Fiber Nonlinearity in Carrier Phase-Locked WDM System," *Photonics Technology Letters, IEEE*, vol. 19, pp. 9-11, 2007.

- [79] K. Kikuchi, "Electronic Post-compensation for Nonlinear Phase Fluctuations in a 1000-km 20-Gbit/s Optical Quadrature Phase-shift Keying Transmission System Using the Digital Coherent Receiver," *Opt. Express*, vol. 16, pp. 889-896, 2008.
- [80] G. P. Agrawal, *Nonlinear Fiber Optics*, 4th. ed.: Academic Press, 2007.
- [81] C. Francia, "Constant step-size analysis in numerical simulation for correct four-wave-mixing power evaluation in optical fiber transmission systems," *Photonics Technology Letters, IEEE*, vol. 11, pp. 69-71, 1999.
- [82] K. K. Parhi and D. G. Messerschmitt, "Pipeline interleaving and parallelism in recursive digital filters. I. Pipelining using scattered look-ahead and decomposition," *Acoustics, Speech and Signal Processing, IEEE Transactions on*, vol. 37, pp. 1099-1117, 1989.
- [83] G. Goldfarb and G. Li, "Demonstration of fibre impairment compensation using split-step infinite-impulse-response filtering method," *Electronics Letters*, vol. 44, pp. 814-816, 2008.
- [84] X. Li, C. Xingzhong, and M. Qasmi, "A broad-band digital filtering approach for time-domain Simulation of pulse propagation in optical fiber," *Lightwave Technology, Journal of*, vol. 23, pp. 864-875, 2005.
- [85] T. Kremp and W. Freude, "Fast split-step wavelet collocation method for WDM system parameter optimization," *Lightwave Technology, Journal of*, vol. 23, pp. 1491-1502, 2005.
- [86] C. S. Burrus, R. A. Gopinath, and H. Guo, *Introduction to Wavelets and Wavelet Transforms: A Primer*: Prentice-Hall, 1998.

- [87] G. Beylkin, "On the Representation of Operators in Bases of Compactly Supported Wavelets," *SIAM Journal on Numerical Analysis*, vol. 29, pp. 1716-1740, 1992.
- [88] T. Pfau, S. Hoffmann, O. Adamczyk, R. Peveling, V. Herath, M. Porrmann, and R. Noé, "Coherent optical communication: Towards realtime systems at 40 Gbit/s and beyond," *Opt. Express*, vol. 16, pp. 866-872, 2008.
- [89] A. Leven, N. Kaneda, and C. Young-Kai, "A real-time CMA-based 10 Gb/s polarization demultiplexing coherent receiver implemented in an FPGA," in *Optical Fiber communication/National Fiber Optic Engineers Conference*, 2008, pp. 1-3.
- [90] E. Mateo, L. Zhu, and G. Li, "Impact of XPM and FWM on the digital implementation of impairment compensation for WDM transmission using backward propagation," *Opt. Express*, vol. 16, pp. 16124-16137, 2008.
- [91] M. Karlsson and H. Sunnerud, "Effects of Nonlinearities on PMD-Induced System Impairments," *Lightwave Technology, Journal of*, vol. 24, pp. 4127-4137, 2006.
- [92] P. P. Mitra and J. B. Stark, "Nonlinear limits to the information capacity of optical fiber communications," *Nature*, vol. 411, pp. 1027-1030, 2001.
- [93] J. Tang, "A comparison study of the Shannon channel capacity of various nonlinear optical fibers," *Lightwave Technology, Journal of*, vol. 24, pp. 2070-2075, 2006.
- [94] J. M. Kahn and H. Keang-Po, "Spectral efficiency limits and modulation/detection techniques for DWDM systems," *Selected Topics in Quantum Electronics, IEEE Journal of*, vol. 10, pp. 259-272, 2004.